A Computer-Aided Tracking and Motion Analysis with Ultrasound System for Describing Hip Joint Kinematics

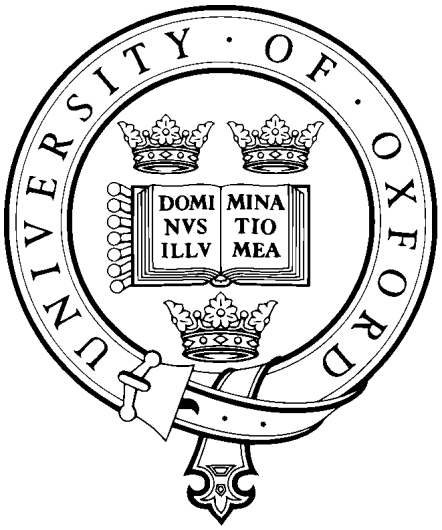

Rui Jia

Kellogg College

University of Oxford

Supervised by
Professor J. Alison Noble & Dr. Stephen Mellon

Submitted: Trinity Term,
October, 2016

This thesis is submitted to the Department of Engineering Science, University of Oxford, in partial fulfilment of the requirements for the degree of Doctor of Philosophy.

Declaration

I declare that this thesis is entirely my own work, and except where otherwise stated, describes my own research.

R. Jia,

Kellogg College

University of Oxford

Dedication

This thesis is dedicated to my dearest family for endless love and support and myself for more than a thousand days and nights' hard work at the University of Oxford.

Abstract

Joint kinematics has been suggested to play an important role in the initiation and progression of a number of musculoskeletal pathologies. Thus, investigation of joint kinematics can help clinicians and researchers to better understand musculoskeletal conditions such as osteoarthritis and trochanteric bursitis. Existing motion capture technologies used in clinical settings suffer from various limitations, including soft tissue artefact. These limitations result in a lengthy examination process, an incomplete movement description, or an inaccurate representation of the real bony landmarks. The recent introduction of a motion analysis with ultrasound (MAUS) system aimed to provide a less constrained approach to detect actual bony structures and describe joint kinematics in three dimensional (3D) space. However, the accuracy of the original MAUS system was highly dependent on the operator's experience.

In this doctoral thesis, a computer-aided tracking and motion analysis with ultrasound (CAT & MAUS) system is developed to track underlying bony landmarks and describe hip joint kinematics during gait. The key contribution of this thesis is to combine state-of-the-art computer vision approaches with the original MAUS system to improve the speed, accuracy and repeatability of joint kinematics examination for clinical measurement and diagnosis.

Firstly, a comprehensive review of gait analysis and relevant clinical diagnostic modalities is presented. Then, an augmented MAUS system architecture is presented, which is more flexible than the previous MAUS system of the data acquisition. It combines an optoelectronic motion analysis (MA) system with a 2D ultrasound (US) device to build up a 3D representation of the bony structure of interest. A novel calibration box with multiple functions for the augmented MAUS system is designed to spatially and temporally match US images to the motion analysis data. The average Euclidean distance error of the spatial calibration is found to be 0.34 mm and the accuracy of the temporal calibration is found to be within half of the frame acquisition interval. The augmented MAUS system with its more accurate calibration procedures can accurately present the bone of interest in 3D space.

Secondly, a computer-aided post-processing pipeline is presented to automatically track the bone of interest in 3D space. A globally optimal registration method is employed to align the 3D surfaces of the target bony structure reconstructed from the manual segmentation in US images at different positions to locate the target bony landmark from one position to another. The globally optimal registration overcomes the issue of getting trapped into local minima for the conventional iterative closest point registration. The accuracy of the globally optimal registration is validated with a proximal femur phantom. The average rotation error is found to be 0.38° and the average translation error is found to be 0.33 mm, both of which are within the clinical tolerance of computer-aided orthopaedics surgery ($\pm 3°$ and $\pm 1mm$). The 3D globally optimal registration guarantees an accurate track of the same target bony structure at different positions instead of estimating the similar bony structure at each position by eyeball with previous MAUS system.

However, in practice, it takes around 20 minutes to manually segment the bone structure for a single surface reconstruction, which is extremely laborious and time consuming. In order to automate the CAT & MAUS system, a novel automatic segmentation of the bone structure in a 2D US image is then developed as a precursor for an accurate globally optimal registration. The automatic bone segmentation introduces the local phase features and acoustic characteristics to enhance the bone probability for detection. The result of the automatic segmentation is validated with a pilot phantom study before applying to the *in-vivo* experiment and achieves an accuracy of 0.13 mm.

After fully developing the CAT & MAUS system, hip joint kinematics of healthy subjects are quantified in six degrees of freedom using the CAT & MAUS system and compared to the results from the optoelectronic motion analysis system. It is shown that CAT & MAUS results describe a greater rotation range than MA results by up to 4.03° in the sagittal plane because the optoelectronic motion analysis system alone suffers from severe soft tissue artefact as the skin markers shift away from the underlying bony structures during movement. The deformation of body segments captured by MA during movements caused by soft tissue artefact is explained using Procrustes analysis to indicate the accuracy and repeatability of the CAT & MAUS system.

Finally, possible future directions are proposed based on preliminary investigations using the developed CAT & MAUS system with particular reference to both the technical and clinical perspectives.

Acknowledgements

An acknowledgement may always be left in the basket, however, it is very important for the author to truly thank a vast number of people who have helped me in my both daily and academic life.

First of all, I wish to sincerely thank my parents (Mr. Geping Jia and Mrs. Qinghua Han) not only for bringing me up, but also for the endless moral support, particularly during my D.Phil period.

This thesis would not be finished without the endless suggestions and supports from my knowledgeable and patient supervisors. Thus, I would like to most sincerely thank both of my supervisors, Professor J. Alison Noble from Institute of Biomedical Engineering and Dr. Stephen Mellon from Nuffield Department of Orthopaedics, Rheumatology and Musculoskeletal Sciences. I feel lucky that I am able to work under their supervision. Alison's valuable technical advices kept me in the correct track throughout my D.Phil. Moreover, her meticulous nature always inspired me to do everything more carefully. Stephen sacrificed a lot of his own time to help most of the experiments as it was not possible to finish the experiments by a person. His enthusiasm for this project encouraged me to move forward.

I am also deeply grateful to my clinical adviser, Mr. Paul Monk. He came up with the initial idea of this amazing project. He also volunteered to be our first subject. Here, I truly thank all the volunteers participated in this research.

There are a great number of people who helped me during my D.Phil in one way or another. I would like to pass my genuine thanks to them. Thank all my colleagues, especially Christopher Bridge, Ali Maraci and Ana Namburete, for their help with my research. Thank all the staffs from Institute of Biomedical Engineering and the gait lab of Nuffield Department of Orthopaedics, Rheumatology and Musculoskeletal Sciences for all the technical support. Thank all my friends, especially Tzuching Hsu, Weidi Xie, Yichen Li, Siqi ying, Li Jin and so on for cheering me up whenever I've been down.

Moreover, I would like to thank Kellogg College for making me a feel like a home in Oxford and its generous funding to support my research and academic travel.

Today's progress is inseparable from previous accumulation. I would like to sincerely thank all my teachers and mentors from early schooling. I would particularly like to thank Mrs. Zhihong Chang for helping me building up a solid science foundation. I would also deeply appreciate Prof. Dong Ming, Professor Xianfeng Zhu and Professor Qiang Li from Tianjin University, and Professor Zhihong Huang and Professor Sandy Cochran from University of Dundee for early leading me into the fantastic biomedical research area.

I also truly thank Orthopaedic Research UK for funding this project and Chinese Scholarship Council for funding myself. Without their financial support, this doctoral thesis would not complete so smoothly.

Lastly, I have to thank myself for not giving up and finally making it after three years' hard work. I wish myself an even brighter future.

Contents

1 Introduction **1**

1.1 Background 1

1.2 Contributions 4

1.3 Thesis overview 5

2 Literature Review **6**

2.1 Gait analysis 7

2.1.1 The anatomy of related bone structures in gait 7

2.1.2 Gait cycle 11

2.1.3 Normal gait 12

2.2 Current measuring technologies 16

2.2.1 Motion capture systems 16

2.2.2 Radiography and fluoroscopy 21

2.2.3 Magnetic resonance imaging 23

2.2.4 Ultrasound 25

2.2.5 Motion analysis with ultrasound 26

2.3 Summary 28

3 Augmented Motion Analysis with Ultrasound System **29**

3.1 Computer-aided tracking and motion analysis with ultrasound system constitution 30

3.2 Calibration 30

3.2.1 Previous calibration methods 32

3.2.2 Design of multi-use calibration box 33

3.2.3 Image distortion assessment 36

3.2.4 Spatial calibration 36

3.2.5 Temporal calibration 43

3.3 Validation 44

3.3.1 Validation setup 44

3.3.2 Patch-based tracking . . . 47
3.3.3 Validation results . . . 58
3.4 Conclusions . . . 60

4 Globally Optimal Iterative Closest Point Registration 61
4.1 Related registration methods . . . 62
4.2 Globally optimal iterative closest point algorithm . . . 65
4.2.1 Iterative closest point registration . . . 65
4.2.2 Branch-and-bound global optimization . . . 66
4.3 *In-vitro* validation . . . 74
4.4 Results . . . 79
4.5 Conclusions . . . 82

5 Automatic Bone Segmentation 84
5.1 Related segmentation methods . . . 85
5.2 Automatic bone segmentation algorithm . . . 86
5.2.1 Bone probability mapping . . . 86
5.2.2 Bone localization optimization . . . 95
5.3 Results . . . 99
5.4 Conclusions . . . 105

6 Quantitative Study of *In-vivo* Hip Joint Kinematics During Gait 106
6.1 *In-vivo* experiment . . . 108
6.1.1 Data acquisition . . . 108
6.1.2 Procrustes analysis . . . 118
6.1.2.1 Measurement of the repeatability of the examination . . 121
6.1.2.2 Quantification of the femur segment deformation during movements . . . 123
6.2 Adapted International Society of Biomechanics recommended hip joint kinematics description . . . 126
6.2.1 Local lower limb bone structure coordinate systems definition . . 127
6.2.2 Hip joint kinematics (rotations) description . . . 129
6.3 Results . . . 130
6.3.1 CAT & MAUS GT and MA GT comparison . . . 130
6.3.2 Hip joint kinematics description . . . 132
6.4 Conclusions . . . 136

7 Conclusions and Future Work **137**
7.1 Contributions . . . 138
7.2 Future work . . . 141
7.2.1 Automatic segmentation on other bone structures . . . 141
7.2.2 Dynamic measurement with more constrained movement protocol using the CAT & MAUS system . . . 141
7.2.3 Clinical analysis and decision making of musculoskeletal problems using CAT & MAUS . . . 143

A List of Publications and Presentations **144**
A.1 Publications . . . 145
A.1.1 Journal papers . . . 145
A.1.2 Conference papers . . . 145
A.2 Conference presentations . . . 146
A.2.1 Oral presentations . . . 146
A.2.2 Poster presentations . . . 146

B Multi-use Calibration Box Design using SolidWorks **147**

C Three Dimensional Freehand Ultrasound Reconstruction using Hybrid Interpolation **150**
C.1 Introduction . . . 151
C.2 Methods . . . 152
C.2.1 Data acquisition . . . 152
C.2.2 Three dimensional volume reconstruction . . . 152
C.3 Results . . . 155
C.4 Conclusions . . . 158

Bibliography . . . 159

List of Figures

1.1 Hip joint pain (Orange colour highlighted). Taken from: http://www.physiologicnyc.com/blog/d/you-don-t-have-to-live-with-hip-pain.php 2

1.2 Planes of the body. Taken from: http://www.1001freedownloads.com/free-clipart/planes-of-the-body . . . 3

2.1 Bones and joints of the lower limbs. Taken from: Figure 1.3 in [140] . . . 8

2.2 The ligaments and the synovial capsule surrounding the hip joint. Taken from: http://medical-dictionary.thefreedictionary.com/hip+laxity 10

2.3 Four gait poses of one gait cycle, heel strike, mid stance, toe off and mid swing. 13

2.4 Gait phases of a little more than one gait cycle beginning with right heel strike. Gait events of the left leg are in italic while the gait events of the right leg are in normal font. The double supports during gait are in bold. 14

2.5 Hip flexion/extension at preferred and maximal gait speed. Mean angle of the hip flexion/extension for 20 healthy subjects. Dark line, gait at preferred velocity; light gray line, maximal velocity. Taken from: Figure 1 in [59] 15

2.6 One gait analysis experiment on a marker attached subject in the Oxford Gait Laboratory with VICON motion analysis system (16 Cara infra-red cameras). 17

2.7 A Kinect device (*Microsoft*). 18

2.8 Microsoft Kinect data captured during gait. Taken from: [9]. 19

2.9 An accelerometer sensor based motion capture system (GaitSmart). Taken from: http://www.gaitsmart.com/ 20

2.10 Anterior-posterior X-ray radiography of the native patellofemoral joint. Note: this image is cropped from the C-arm fluoroscopic data collected in Nuffield Orthopaedics Hospital, Oxford with the ethical approval (08/H00606/114) in [88] 21

2.11 Anterior-posterior X-ray radiography of the patellofemoral joint with joint replacement. Note: this image is cropped from the C-arm fluoroscopic data collected in Nuffield Orthopaedics Hospital, Oxford with the ethical approval (08/H00606/114) in [88]. 22
2.12 Anterior-posterior T2 MRI of the hip joint. Note: this image is cropped from the T2 MRI data collected in Nuffield Orthopaedics Hospital, Oxford with the ethical approval (08/H00606/114) in [88]. 23
2.13 A subject standing within one open MRI system for dynamic measurement.Cropped from Figure.1 in [125]. 24
2.14 A 2D ultrasound image of the patellofemoral joint. 25
2.15 Difference of the results from the MA system (black) compared to the MAUS results (red). Taken from [88]. 27

3.1 A schematic of the computer-aided tracking and motion analysis with ultrasound system. 31
3.2 Multi-use calibration box. 34
3.3 Five pairs of metal cross wires on two frames with rectangular cut-out windows in the middle. 35
3.4 Schematic of spatial calibration. 37
3.5 Two representations of the cross-wires under US when the US image misaligned with the cross-wires plane. 38
3.6 Representation of the cross-wires under US when the US image well-aligned with the cross-wires plane. 39
3.7 Local coordinate systems, a) ultrasound local coordinate system (ULCS), b) probe local coordinate system (PLCS) and c) crosses local coordinate system (CLCS). 41
3.8 Transformation relationship map of spatial coordinate systems. 42
3.9 Experimental setup for validation of spatial and temporal calibration with a proximal femur model. 45
3.10 Data of the validation experiment of spatial and temporal calibration, a) cropped US image of the GT marker and b) markers captured by MA system. 46
3.11 Schematic diagram of patch-based tracking. 47
3.12 US image of a proximal femur with a selected patch (white box). 48
3.13 Number of incorrect tracked frames with different patch sizes in a single ultrasound video and the deviation of number of incorrect tracked frames over ten videos. 49

3.14 Number of missed tracking frames in a single ultrasound video with its deviation over ten videos (blue line) and the elapsed time when building the K-D trees (red line) with different numbers, M, of PCA components in a single ultrasound video. 50
3.15 The first 25 principal components for patches projection. 51
3.16 Comparison between an US image and the its compressed image. 52
3.17 The accuracy percentage map for λ_d and λ_a parameters selection. 55
3.18 Example results from the dynamic programming stage. The diagram illustrates the graph constructed from frames 1 to 5 of example video. The table shows the Euclidean distance error with respect to the ground truth. 57
3.19 Euclidean distance error between the MA GT marker and the MAUS GT marker over five trials. 58
3.20 Results of the temporal calibration, a) before and b) after. 59

4.1 Limitation of the conventional ICP algorithm. 63
4.2 Derivation of the rotation uncertainty radius. 68
4.3 Rotation uncertainty radius. 69
4.4 Translation uncertainty radius. 70
4.5 Uncertainty radius. 71
4.6 Lower Bound illustration. 72
4.7 BnB global searched ICP. 74
4.8 The proximal femur phantom with a ball joint at the femur head 75
4.9 Proximal femur model clapped in a water tank. 75
4.10 *In-vitro* experiment setup. 76
4.11 Ultrasound parallel scanning. 77
4.12 All markers used in the registration validation captured by motion analysis system. 77
4.13 Reconstructed greater trochanter surface of the proximal femur phantom. 78
4.14 Results comparison between globally optimal ICP registration and conventional ICP registration. 79
4.15 Rotation errors around three axes compared to the ground truth of a) the globally optimal ICP registration and b) the conventional ICP registration. 80
4.16 Translation errors along three axes compared to the ground truth of a) the globally optimal ICP registration and b) the conventional ICP registration. 81

5.1 The ultrasound image smoothed by a Gaussian filter ($\sigma = 6$). 86
5.2 The binary mask for the ultrasound image to get rid of useless pixels. . . 87
5.3 The ultrasound image filtered by a Laplacian of Gaussian filter ($\sigma = 6$). . 88

5.4 Frequency-domain representations of 2D log-Gabor filter and the two parts after Riesz transformation a) the even filter, b) and c) the odd filters. . . 89
5.5 The local Energy of the ultrasound image. 90
5.6 The local phase of the ultrasound image. 91
5.7 The feature symmetry of the ultrasound image. 92
5.8 The shadow map of the ultrasound image. 93
5.9 The integrated backscattering map of the ultrasound image. 94
5.10 Final bone probability mapping. 94
5.11 Three parts of the bone segmentation *Seg(s)*. Note: the white line is thickened for better visualization. 95
5.12 Segmentation results after adjusting the parameters α and β, a) segmentation at $\alpha = 10$ and $\beta = 1$, b) segmentation at $\alpha = 1$ and $\beta = 10$, c) segmentation at $\alpha = 3$ and $\beta = 1$. Segmentation results have been thickened for better visualization. 97
5.13 Probability map comparison, a) probability mapping of the method in [37], b) probability mapping of the developed method. 100
5.14 The automatic segmentation results with this developed method (white line) and the method in [37] (blue line), and the manually segmented ground truth (red line), two different US representations of the phantom and four of the human greater trochanter. All the segmentation results are dilated for better visualization. 101

6.1 A pipeline schematic of the CAT & MAUS system. 107
6.2 Retro-reflective markers attached on one test subject in the front, sagittal and back views. 111
6.3 Four gait poses (heel strike, mid stance, toe off and mid swing) of the left leg in the sagittal, front and back views. 113
6.4 Motion analysis data of the lower limb model at five different poses. . . . 114
6.5 The LGT capture using CAT & MAUS, a) *in-vivo* data acquisition and b) US scanning in a parallel sweep. 115
6.6 CAT & MAUS data of the lower limb model at five different poses captured by the motion analysis system. 116
6.7 The lower limbs MA model with the CAT & MAUS reference surface of greater trochanter reconstructed at the upright standing pose and the selected greater trochanter bony landmark superimposed. 117
6.8 An example of greater trochanter localization using globally optimal registration. 118
6.9 Lower limb body segments split from motion analysis data points. 119

6.10 Two shapes a) before and b) after superimposing. 120
6.11 An illustration of the difference between the femur segments modelled by MA alone and CAT & MAUS at the standing pose. 123
6.12 An illustration of the comparison between the femur segments modelled by each of MA alone and CAT & MAUS at one example gait pose. . . . 124
6.13 An illustration of the comparison between the femur segments modelled by each of MA alone and CAT & MAUS at the standing pose and one example gait pose. 125
6.14 Left hip joint coordinate systems, pelvic coordinate system (X,Y,Z) and adapted femoral coordinate system (x,y,z), and the kinematics description. 127
6.15 Difference between the GT captured by MA alone and the GT captured by CAT & MAUS at heel strike pose. 131
6.16 Three dimensional visualization of hip joint at heel strike pose compared to standing pose to indicate the error caused by soft tissue artefact. . . . 132
6.17 Quantification of hip joint rotation angles using the CAT & MAUS system, a) flexion/extension, b) adduction/abduction and c) internal/external rotation. 133
6.18 Quantification of hip joint rotation angles using the motion analysis system alone (i.e. without US), a) flexion/extension, b) adduction/abduction and c) internal/external rotation. 134

7.1 Hip joint rotation experiment, a) experiment pose, b) pose in motion analysis. 142

B.1 Solidworks design of calibration box with an open window in the front (Unit: mm). 148
B.2 Solidworks design Dual frames of the calibration box (Unit: mm). 149

C.1 US scanning, a) in parallel, and b) from heel to toe. 152
C.2 One cross section of the reconstructed US volume, a) without interpolation, b) VNN interpolation (discontinuity artefacts circled), c) and d) DW interpolation (with different distance threshold), and e) our method. . . . 156
C.3 Intensity comparison between DW, VNN and our method, a) local region of interest (ROI), and b) comparison of inter-pixel intensity variations. . 157

List of Tables

3.1 Ultrasound image distortion analysis with different ultrasound powers (USP) after moving the frame to different positions (FM). 37

5.1 An comparison between the manually segmented ground truth and a) the results using this developed method with different thresholds, and b) the results on the same data set using the method in [37] with different thresholds. The thresholds highlighted in grey gave best results for each of these two methods. 104

6.1 Anthropometric parameters of the ten healthy volunteers. 109
6.2 Bony landmarks of lower limbs and the methods used to track these landmarks. 110
6.3 Shape comparison between lower limb segments between three examinations including Procrustes distance and the sum of Euclidean distance at each of standing pose and four gait poses. 122
6.4 Procrustes distance between the femurs modelled by MA alone and CAT & MAUS at four gait poses compared to the femurs modelled by MA alone and CAT & MAUS at the standing pose. 125
6.5 Euclidean distance between the CAT & MAUS GT and the MA GT at the standing pose and four different gait poses. 130

List of Abbreviations

All the technical abbreviations and their explanations are listed in alphabetical order.

- 2D: Two Dimensional - the physical universe
- 3D: Three Dimensional - the physical universe
- 6DOF: Six Degrees Of Freedom - the freedom of movement of a rigid body in three-dimensional space
- CAOS: Computer-Aided Orthopedic Surgery - a discipline where computer technology is applied pre-, intra- and/or post-operatively to improve the outcome of orthopedic surgical procedures
- CAT & MAUS: Computer Aided Tracking and Motion Analysis with Ultrasound System - a measuring system composed of state-of-the-art computer vision knowledge, a 2D ultrasound device and a motion analysis system.
- CLCS: Cross-wires Local Coordinate System - a coordinate system built by the makers attached on the movable beam
- GT: Greater Trochanter - A strong process overhanging the root of the neck of the femur, giving attachment to the gluteus medius and minimus muscles, the piriform muscle, the internal and external obturator muscles, and the gemelli muscles
- IBS: Integrated BackScattering - integrated backscattered signals
- ISB: International Society of Biomechanics - a society dedicated to promoting biomechanics in its various forms
- K-D: K-Dimensional - the physical universe
- MA: Motion Analysis - a motion capture technology

- MAUS: Motion Analysis with Ultrasound System - a system to transform points in a 2D ultrasound image into 3D global coordinate system by referring the positions of the ultrasound probe captured by the motion analysis system
- MRI: Magnetic Resonance Imaging - a medical imaging technique used in radiology to image the anatomy and the physiological processes of the body in both health and disease
- PCA: Principal Component Analysis - a statistical procedure that uses an orthogonal transformation to convert a set of observations of possibly correlated variables into a set of values of linearly uncorrelated variables called principal components
- PLCS: Probe Local Coordinate System - a coordinate system built by the makers attached on the ultrasound probe
- RMS: Root Mean Square - a statistical measure defined as the square root of the mean of the squares of a sample
- SBM: Skin Based Markers - retro-reflective markers attached on human skin
- STA: Soft Tissue Artefact - distortion of the measurement caused by soft tissues (such as muscle, fat and so on) surrounding the target region
- TB: Trochanteric Bursitis - the inflammation of the trochanteric bursa
- ULCS: Ultrasound Local Coordinate System - the coordinate system build up for describing the pixel
- US: Ultrasound - an imaging technology

Chapter 1

Introduction

1.1 Background

Musculoskeletal conditions encompass around two hundred different problems affecting daily activities thereby reducing the quality of life [101]. Musculoskeletal problems are commonly reported the world over; around ten million adults and twelve thousand children have a musculoskeletal condition in England [95]. While the pathology of many musculoskeletal problems, such as trochanteric bursitis, is unknown, the result is abnormal joint kinematics [106]. It has been recently demonstrated that there is a difference in patellofemoral joint (formed by the patella (knee-cap) and femur) kinematics between healthy subjects and subjects who had knee joint replacement [88]. This is an example of where an investigation of joint kinematics has contributed to a better understanding of a musculoskeletal problem. However, current diagnostic modalities suffer from various limitations, for example soft tissue artefact, the limited field of view of devices and so on, to accurately and dynamically measure three dimensional (3D) joint kinematics of hip or knee during routine activities such as walking or squatting.

Hip joint pain (Figure 1.1) is very common in musculoskeletal conditions [92]. It is more prevalent in women and most frequently occurs between 40-60 years of age. Approximately 10-25% of the general population is affected by hip joint pain [92]. Subjects complain of a dull, burning or sharp stabbing pain, which is exaggerated when climbing stairs, or following long walks. The nature of the pain varies from chronic to intermittent aching over the greater trochanter and up to 40% complain of pain radiating from their lateral thigh towards the knee [28].

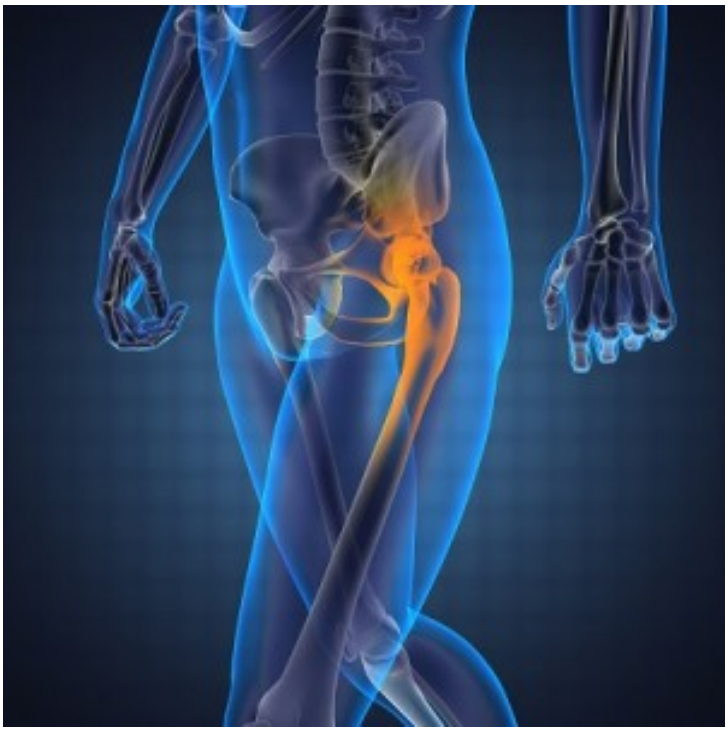

Figure 1.1: *Hip joint pain (Orange colour highlighted). Taken from: http://www.physiologicnyc.com/blog/d/you-don-t-have-to-live-with-hip-pain.php*

There are many pathogeneses cause hip joint pain, for example, inflammation, osteoporosis, osteoarthritis or inappropriately designed joint prosthesis and so on [28] [123]. Abnormal hip biomechanics are a physical characteristic of hip joint pain [122] but, to the author's knowledge, no study on hip loading or kinematics of an affected cohort has been carried out in six degrees of freedom (6DOF) as it is extremely difficult to describe hip joint kinematics in the coronal plane (an imaginary plane that divides the body into ventral and dorsal parts) and the transverse plane (an imaginary plane that divides the

body into superior and inferior parts) with current existing measurement tools. Body planes are shown in figure 1.2.

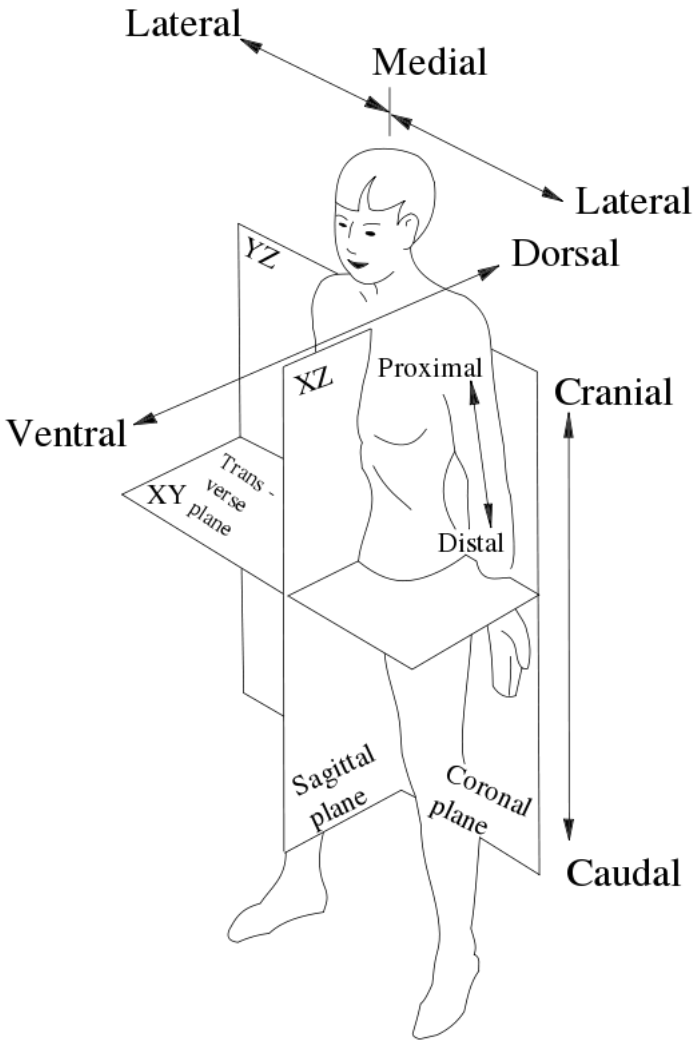

Figure 1.2: *Planes of the body. Taken from: http://www.1001freedownloads.com/free-clipart/planes-of-the-body*

In this research, a novel, non-invasive computer-aided tracking and motion analysis with ultrasound (CAT & MAUS) system is developed for dynamically measuring *in-vivo* joint (hip joint) kinematics in 6DOF. CAT & MAUS transforms bone contours automatically segmented from 2D ultrasound videos into 3D global coordinate system to build up 3D bone surfaces based on the position information of the ultrasound probe captured by the motion analysis system. Moreover, it calculates joint kinematics by registering the bone surfaces from sequential gait poses to a reference standing pose. Accurately

describing the kinematics of joints could not only help clinicians better understand the anatomy and function of the joints, but also potentially help engineers to improve prosthesis design. It is hoped that the final validated system could be applied in outpatient assessment and commercially manufactured in due course.

1.2 Contributions

This thesis introduces a framework for computer-aided tracking and motion analysis with ultrasound (CAT & MAUS) system to describe joint kinematics. The main contributions are:

- An augmented motion analysis with ultrasound system was developed to detect the underlying bony structures. A multi-use calibration box was designed for spatial and temporal calibration for freehand 3D ultrasound acquisition along with femur phantom validation (Chapter 3).

- An accurate patch-based tracker was developed to track the interested bony landmark (Chapter 3).

- A globally optimal registration algorithm was successfully employed for 3D bone surface-to-surface registration (Chapter 4). The globally optimal registration tackles the issue of getting trapped into local minimum for conventional iterative closest point registration. A proximal femur phantom with a socket ball joint was designed to test the accuracy of the computer-aided algorithms in 6DOF.

- A novel ultrasound bone structure segmentation (Chapter 5) and a hybrid interpolated 3D reconstruction 1001[63]algorithm (Appendix C) were developed to estimate the 3D bone surface as a precursor to the surface-to-surface registration.

- A quantitative analysis of hip joint kinematics in 6DOF during gait was conducted using the CAT & MAUS system compared to MA data. A gait model of healthy subjects was built by CAT & MAUS (Chapter 6).

1.3 Thesis overview

In Chapter 2, a comprehensive review of gait analysis and state-of-the-art diagnostic modalities for joint motion monitoring is presented.

In Chapter 3, an augmented motion analysis with ultrasound (MAUS) system is introduced to detect underlying bony landmarks. A multi-use calibration box for image distortion assessment, and spatial and temporal calibrations for the MAUS system is designed and validated using a proximal femur phantom. An automatic patch-based tracking algorithm is developed to accurately track the bony landmarks of the femur phantom in US videos.

In Chapter 4, a globally optimal rigid body registration algorithm is employed to locate the target bony structure. A proximal femur phantom is used to validate the registration algorithm. From the registration result, the target bony landmark can be accurately located at different positions to avoid mis-detection of the same bony landmark using a previous MAUS system.

Chapter 5 introduces a novel local phase-based segmentation algorithm to segment bone structure in ultrasound images. An accurate 3D segmented surface is the precursor for registration. A hybrid interpolation method for the 3D ultrasound volume reconstruction from a stack of 2D ultrasound slices is described in Appendix C to reconstruct those segmented 2D bony structures into a 3D bone surface.

In Chapter 6, the developed CAT & MAUS system is applied in the assessment of healthy subjects' hip joint kinematics during gait. The results from the CAT & MAUS system are compared with the results from the motion analysis system alone (i.e. without US). The deformation of marker-based lower limbs segments caused by soft tissue artefact during movements is explained using Procrustes analysis to indicate the accuracy and repeatability of the CAT & MAUS system.

Chapter 7 presents conclusions and suggestions for future work.

Chapter 2

Literature Review

In this chapter, a comprehensive literature review of human gait analysis and clinical state-of-the-art diagnosis modalities is presented to help readers better understand the background and necessity of this research.

2.1 Gait analysis

Gait analysis is a systematic study of walking which helps in the medical understanding of diseases that affect locomotion. Walking is a cyclical sequence of movements of the lower limbs which propel the body forward while simultaneously maintaining stance stability [102]. Gait is the pattern of walking of lower limbs during locomotion [140]. Walking is one of the most common activities of daily living [91]. However, many musculoskeletal conditions lead to abnormal gait. Moreover, an abnormal walking pattern has been suggested to be highly related to unclear pathology of many joint diseases [106]. Thus, analysing gait function helps clinicians to gain a better understanding of unknown pathology of many musculoskeletal diseases.

2.1.1 The anatomy of related bone structures in gait

Walking is a complex movement [139]. During gait, nerves, muscles, tendons, ligaments and bones, collectively control the gait pattern. Detailed anatomy of the locomotor system was well introduced in [98]. As it goes beyond the needs of this thesis to introduce detailed anatomy of body structure, only the most relevant bone structures are reviewed here.

In walking, it could be considered that nearly all bone structures in the body are activated. There are eleven main lower limb bony segments (pelvis, left and right femurs, patellas, tibiae, fibulae and feet) and three major joints (hip joint, knee joint (patellofemoral joint and tiobiofemoral joint) and ankle joint (talocrural joint and subtalar joint)) involved in daily walking movements which are shown in Figure 2.1. The key bony landmarks of the pelvis and lower limbs are labelled in Figure 2.1. These landmarks are often used to quantify the joint kinematics during motion. The primary application of this research is to measure hip joint kinematics in 6DOF during gait using the developed CAT & MAUS system (defined in detail in Chapter 6). As the hip joint is a spheroidal (ball in socket) joint linking the pelvis and femur, the movement between the

pelvis and the femur can be described and quantified by rotations in three degrees of freedom (3DOF). Thus, from a practical point of view and the scope of this thesis, only the bones of the pelvis and lower limbs are considered in this section.

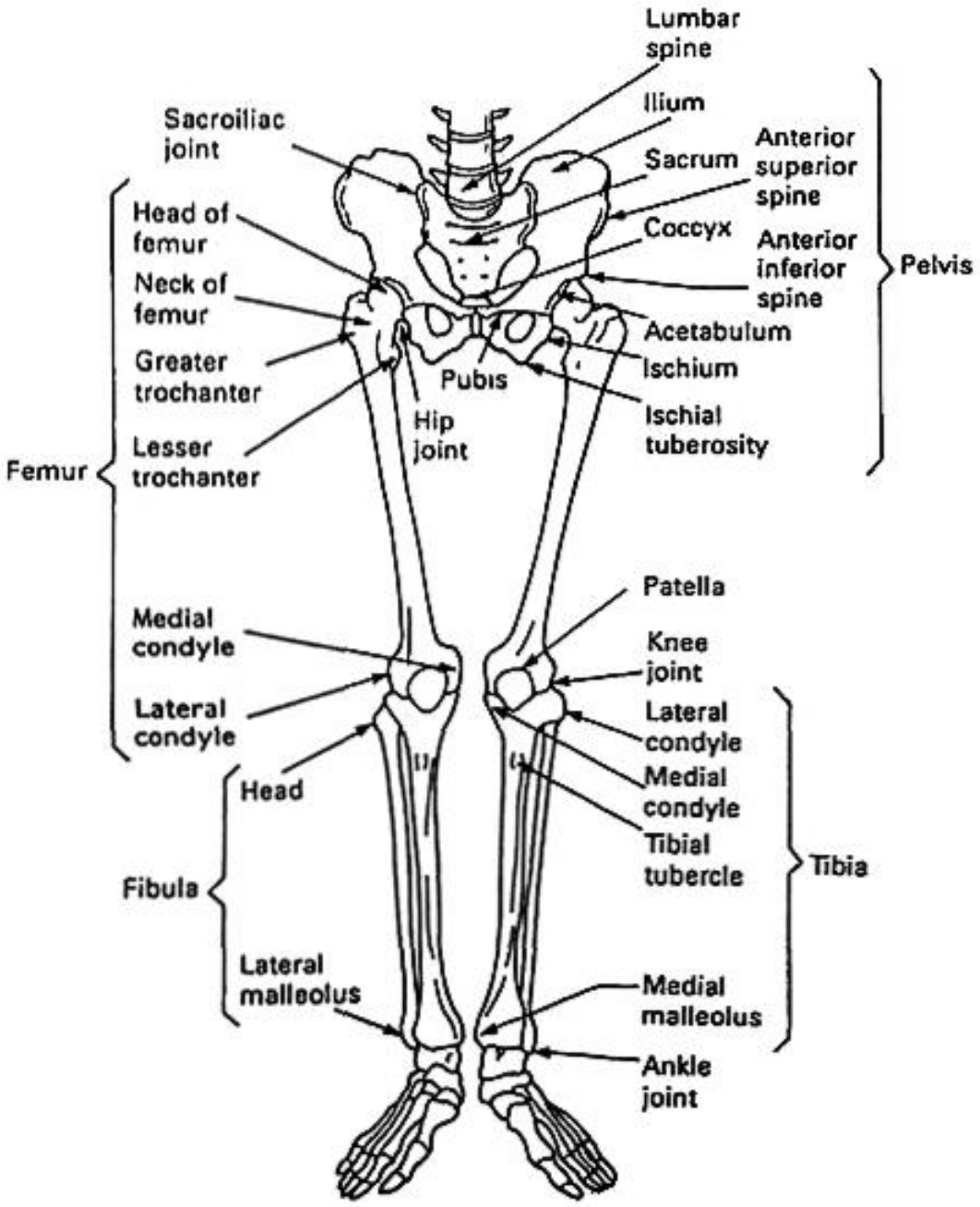

Figure 2.1: *Bones and joints of the lower limbs. Taken from: Figure 1.3 in [140]*

The pelvis is part of the skeleton embedded in the trunk of the human body between the abdomen and the thighs [127]. It consists of the sacrum, the coccyx and the two innominate hip bones. The sacrum is the fusion of the five sacral vertebrae. The coccyx is the vestigital 'tail', consisting of three to five rudimentary vertebrae. Each of those two innominate hip bones is the fusion of three bones: the ilium, ischium and pubis, as in Figure 2.1 [90]. The only movement between the separate bone parts of the pelvis occurs at the sacroiliac joint. However, this movement is generally very subtle in adults [127]. Thus, in gait analysis, the pelvis as a whole is regarded as a single rigid bony structure. In the inferior pelvis, there is a socket structure on each side called the acetabulum, which is the proximal part of the hip joint, with which the femoral head is almost entirely congruent.

The femur is the only bone in the thigh. The spherical head of the femur articulates with the acetabulum of the pelvis, which forms the hip joint. The bone part of the femur from the head of the femur pointing to the shaft of the femur is called the neck of the femur which links the shaft of the femur bone to the hip joint [140]. Lateral to the junction of the femoral neck and shaft are two bony protuberances, which are the site of muscular insertion. The lateral femoral protuberance is called the greater trochanter (GT) which can be palpated under the skin. The GT is also the target bony landmark focused on in this thesis. The second protuberance, the lesser trochanter is medial to the GT. The proximal femur extends downwards to the knee joint. Distally, the lateral and medial femoral condyles form the trochlear groove anteriorly. This forms the proximal part of the knee joint (patellofemoral joint), which articulates with the patella [46].

A joint is formed where one bone segment articulates with another. Most joints that can perform a significant movement can be classified as synovial joints [139]. There are other joint types in which only small movements can occur, for example fibrous joints and cartilaginous. The ends of the bone segments which articulate in a synovial joint are covered by cartilage and surrounded by a synovial capsule which secretes the lubricant synovial fluid [140]. The hip joint is a synovial joint since it can perform a substantial

range of motion, for example gait. The hip joint, formed by the femoral head and the pelvic acetabulum, is the only true spheroidal joint in human lower limbs. The hip joint is protected by the synovial capsule around the joint, a number of ligaments between the pelvis and the femur and the ligament teres between the centre of the femoral head and the centre of the pelvic acetabulum as in Figure 2.2. Injuries of the ligaments or the synovial

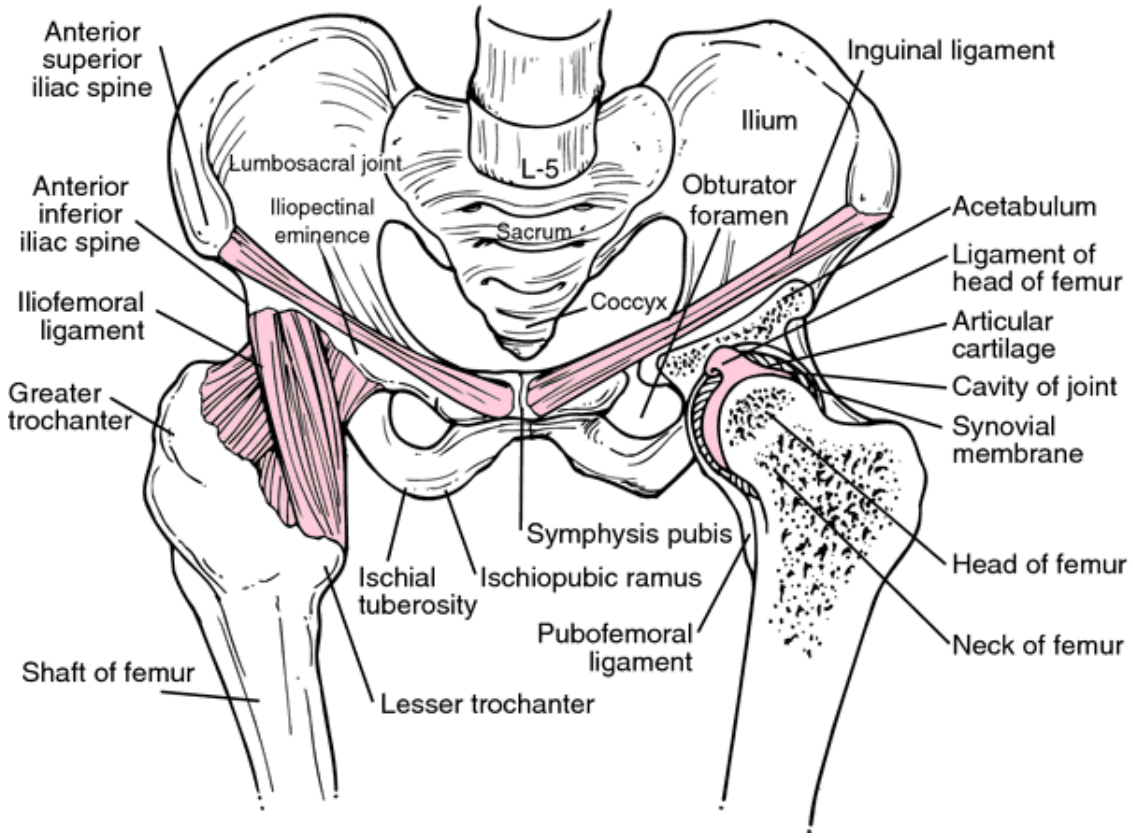

Figure 2.2: *The ligaments and the synovial capsule surrounding the hip joint. Taken from: http://medical-dictionary.thefreedictionary.com/hip+laxity*

capsule may lead to various hip joint pains as well as abnormal hip joint kinematics during movements [20]. However, ligament injury is beyond the scope of this thesis, but remains an interesting and relevant question, the correlation between ligament injury and hip joint pain as ligaments influence joint movements. Joint kinematics describe joint movements, but without reference to the forces involved [139]. Thus, quantification of joint kinematics can help clinicians to better understand musculoskeletal pathologies [88].

Since the hip joint is a spheroidal joint, it performs rotations in three degrees of

freedom as flexion/extension, adduction/abduction and internal/external rotation. As this thesis is mainly focused on hip joint kinematics during gait, these rotations of the hip joint in 3DOF are described and quantified in Chapter 6. The hip joint rotations are quantified at different events of one gait cycle. Gait events and phases are introduced in Section 2.1.2.

2.1.2 Gait cycle

A single gait cycle is defined as the time interval between two sequential performances of one repetitive pose of walking [140]. Most studies define the start of the full gait cycle using heel strike, the instant when one foot makes contact with the ground surface, with the end of the cycle being the instant immediately before the same foot contacts again with the ground surface [4] [40].

There are two main phases during one gait cycle: the stance phase and the swing phase [99]. The stance phase is the period when all or part of the foot contacts the ground surface. The swing phase is the period during which one lower limb swings forward between the end of one stance phase and the start of the next. The stance phase takes around 60% of a gait cycle and the swing phase takes around 40% of a gait cycle [32]. The first and the last 10% of the stance phase are two periods of double support, i.e. both feet are in contact with the ground surface [32]. Moreover, the following events during gait can be identified by characteristic poses. An illustration of four gait poses of one gait cycle is shown in Figure 2.3 and the gait phases are shown in Figure 2.4.

- **Heel strike**: the beginning of the stance phase of one gait cycle. The position at which the foot heel of the reference leg just makes contact with the ground surface.
- **Mid stance**: the mid point of the stance phase. The position at which the foot of the opposite leg is passing the reference leg.
- **Toe off**: the final pose of foot contact during the stance phase of one gait cycle. The position at which the foot toe of the reference leg is just off the ground surface.

- **Mid swing**: the mid point of the swing phase. The position at which the foot of the swinging reference leg is passing the opposite leg in stance.

2.1.3 Normal gait

In order to identify musculoskeletal pathology from gait patterns, it is essential to firstly characterise normal gait as a reference against which abnormal gait can be compared. The narrow definition of 'normal' gait is walking performed by a subject who is healthy without any joint replacement, musculoskeletal conditions or diseases that can lead to abnormal musculoskeletal kinematics [5]. However, an appropriate 'normal' reference should take gender, age and other anthropometric parameters, such as height, weight and so on, into consideration for individual comparison [139]. It is reasonable to assume, for example, that the gait of an elderly female subject may differ substantively from that of a young fit male subject. Although every individual has a unique gait, the narrow meaning of a 'normal' gait is considered in this research to generalise a healthy gait pattern.

From a physiological perspective, a normal gait depends upon the integrated action of many components, including bones, muscles and nervous system, that make up the musculoskeletal system. This integration determines the gait pattern difference. Any defect in any component of this integration may lead to a pathological gait pattern [135].

From a mechanical perspective, a normal gait is a form of bipedal locomotion by an alternating motion between the lower limbs. The reference leg in the stance phase goes through three stages; restraining, supporting and propulsion, while the opposite leg in the swing phase creates a new step forward. So a normal gait is a consecutive, rhythmic and alternating motion of subjects upper limbs, lower limbs and trunk to generate a forward movement. A subject who performs normal gait should have the ability to support an upright position, to maintain balance during gait and to develop a new forward step [140]. In biomechanics, gait analysis describes kinetics and kinematics. For kinetics, it describes force performance during gait, including muscular force, gravitational force, forces of

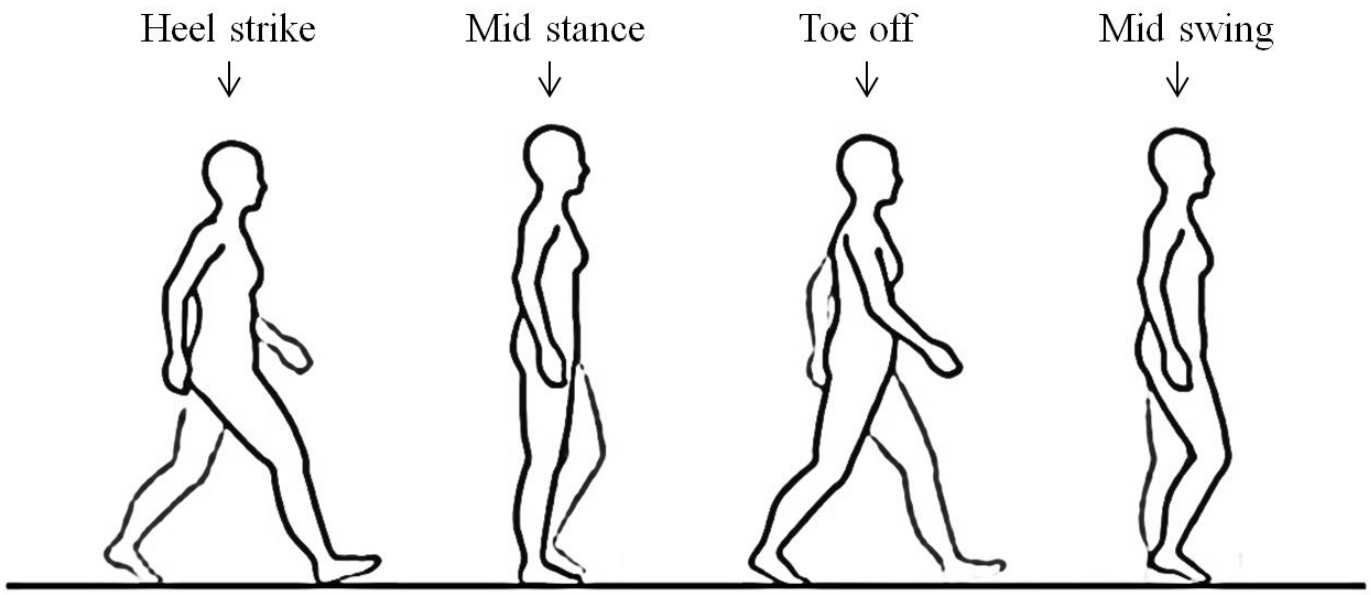

Figure 2.3: *Four gait poses of one gait cycle, heel strike, mid stance, toe off and mid swing.*

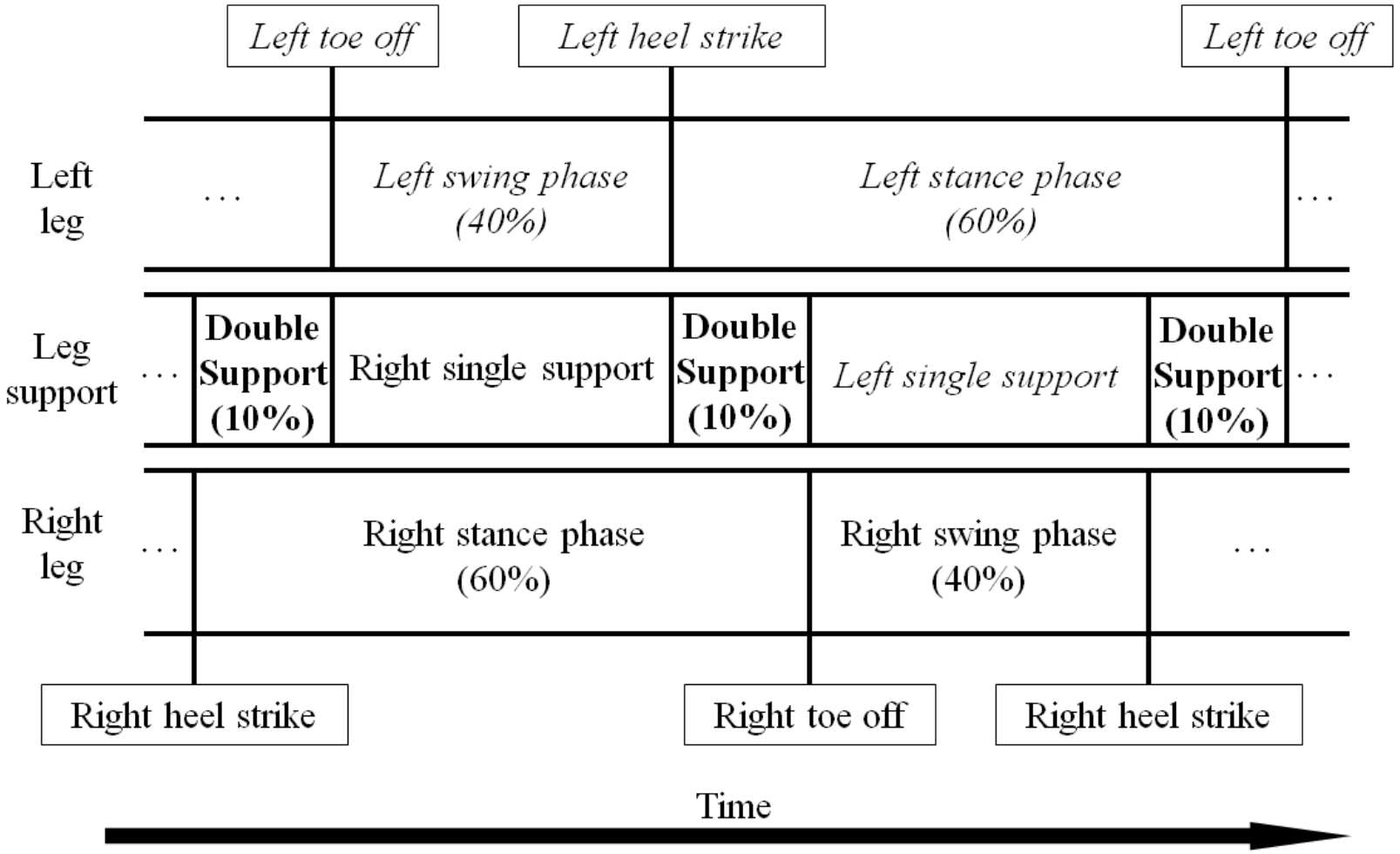

Figure 2.4: *Gait phases of a little more than one gait cycle beginning with right heel strike. Gait events of the left leg are in italic while the gait events of the right leg are in normal font. The double supports during gait are in bold.*

momentum and floor reaction force, all of which have been investigated by modelling or using force plates [31] [53] [81] [139]. However, kinetics during gait is beyond the scope of this thesis.

In this thesis, hip joint kinematics during gait is mainly considered. Kinematics describe the motion of an object (displacements, velocity, acceleration, etc.). Describing hip joint kinematics is to quantify the rotation of this spheroidal joint in three degrees of freedom during movements [65]. However, it is non-trivial to describe hip joint kinematics in the coronal plane and the transverse plane as the movements in these two planes are relatively small compared to the movement in the sagittal plane. Thus, in the literature, most studies have focused on quantifying the rotation in the sagittal plane which is defined as flexion/extension as in [3] [8] [50] [59] [69] [73] [77]. One example of the average flexion/extension reported in [59] is shown in Figure 2.5.

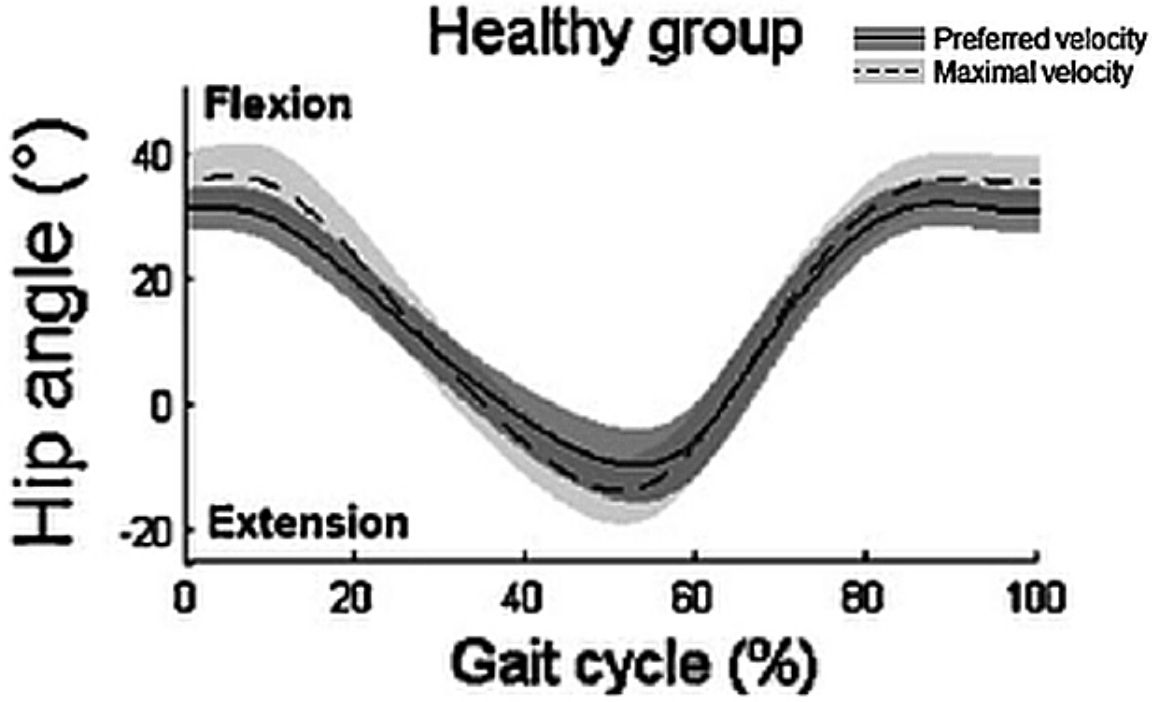

Figure 2.5: *Hip flexion/extension at preferred and maximal gait speed. Mean angle of the hip flexion/extension for 20 healthy subjects. Dark line, gait at preferred velocity; light gray line, maximal velocity. Taken from: Figure 1 in [59]*

The flexion/extension angle for healthy subjects at the preferred gait speed varies

from $30^\circ \pm 4^\circ$ to $-8^\circ \pm 6^\circ$ while the angle for healthy subjects at the maximal gait speed varies from $38^\circ \pm 5^\circ$ to $-12^\circ \pm 6^\circ$. Literature on the quantification of hip joint rotation during gait in the coronal plane and the transverse plane can be found in [34] [49] [134]. However, since the real bony landmarks cannot be tracked using the technologies reported in the literature above, the full rotation of the hip joint cannot be quantified accurately. State-of-the-art technologies used for measuring joint movements are reviewed in Section 2.2.

2.2 Current measuring technologies

Modalities for monitoring joint kinematics in native joints have been applied to the knee [19] [38] [88] [125] and the hip [27] [64] [87] [105]. In this section, several commonly used measuring modalities are briefly introduced with their advantages and disadvantages discussed.

2.2.1 Motion capture systems

Motion capture systems are frequently utilised to monitor joint movements. In this section, three of them (two optoelectronic systems and one accelerometer sensor system) are reviewed.

Optoelectronic motion analysis (MA) systems, such as a VICON infra-red camera system (*Oxford, UK*), are the most widely used in clinics to analyse a subject's gait pattern, for example in [30] [33] [145]. It is composed of a set of infra-red cameras covering the 3D volume of interest. In musculoskeletal studies, retro-reflective markers are attached on the skin of a test subject. By capturing reflectivity of these skin-attached retro-reflective markers under infra-red, these markers can be reconstructed in 3D space to provide position information of the test subject as in Figure 2.6. Researchers assume that these retro-reflective markers move in the same way as their represented underlying bony landmarks during the assessment. However, in practice, these markers slide away



Figure 2.6: *One gait analysis experiment on a marker attached subject in the Oxford Gait Laboratory with VICON motion analysis system (16 Cara infra-red cameras).*

relative to the underlying bony landmarks to produce what is known as soft tissue artefact (STA) [76]. Motion analysis systems suffer from STA associated with skin based markers. Soft tissue artefact can cause severe errors as high as 50 mm varying based on a test subject's gender, body size and body position during assessments [1].

This type of motion capture system is non-invasive, non-ionising and flexible. However, it can not describe the actual movements of underlying bony structures and it is subject to spatial constrains because of cameras placement.

Another commonly used optoelectronic motion capture system is the Kinect (*Microsoft*). The Kinect uses an infra-red projector and sensor to compute and construct a depth map by analysing a speckle pattern of infra-red laser light as in Figure 2.7 [80].

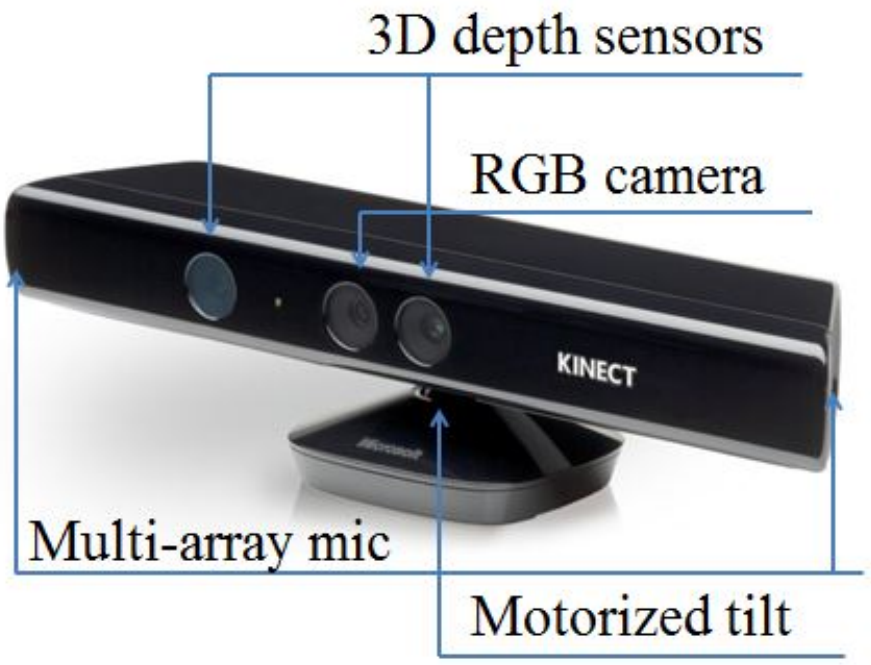

Figure 2.7: *A Kinect device (Microsoft).*

The Kinect has been used in gait analysis to recognise the gait gesture as in [39] [85] [109]. Compared to other motion analysis systems, the Kinect is cheap and portable. However, the Kinect only captures the subject in a limited scope in front of the device. The system may lose track of the subject when obscured by other objects. Moreover, the data from the Kinect only outlines the overall shape of the subject as in Figure 2.8. Similar to the optoelectronic motion analysis systems, the Kinect cannot detect underlying bony structures either.

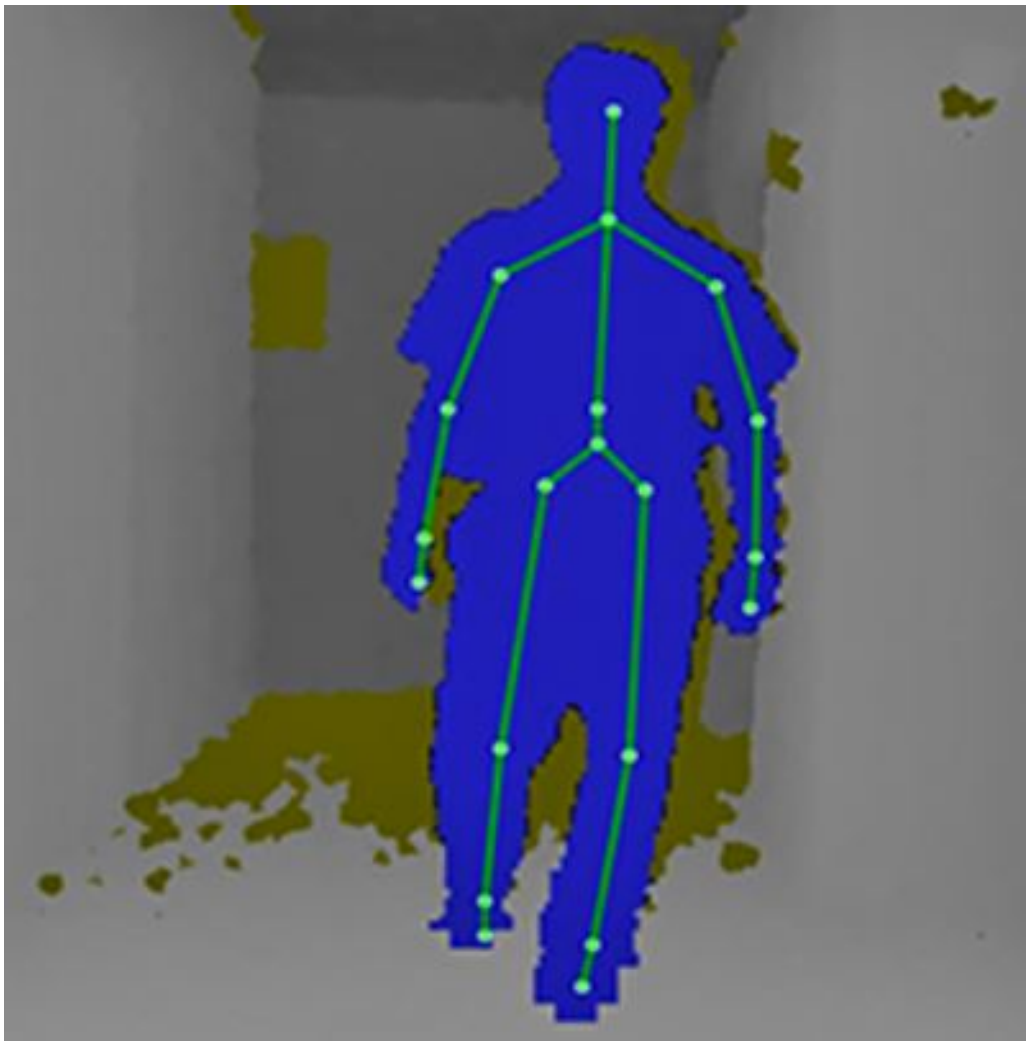

Figure 2.8: *Microsoft Kinect data captured during gait. Taken from: [9].*

Another type of motion capture system is based on mechanical sensors as in [10] [78] [111] [129]. For this type of motion capture systems, most of the sensors are tied to body limb segments. One example with accelerometer sensors (*GaitSmart, Hertford, UK*) is shown in Figure 2.9.



Figure 2.9: *An accelerometer sensor based motion capture system (GaitSmart). Taken from: http://www.gaitsmart.com/*

This type of motion capture systems solves the issue of spatial limitation during measurements. It is much easier and less time consuming to set up the experiments than the optoelectronic motion analysis system. However, it still cannot track the actual underlying bony structures during movements.

To overcome the above limitations of motion capture systems, the following modalities have been utilised to image underlying bony structures.

2.2.2 Radiography and fluoroscopy

X-ray radiography has been used to image the patellofemoral joint [74]. The bone structures under X-ray are clearly visible. For example, to image the native knee joint, although the patella and the femoral condyles are overlapped in the coronal plane of the X-ray image, the patella (outlined with white colour) and the femur are still distinguishable because of the different bone density as in Figure 2.2.2.

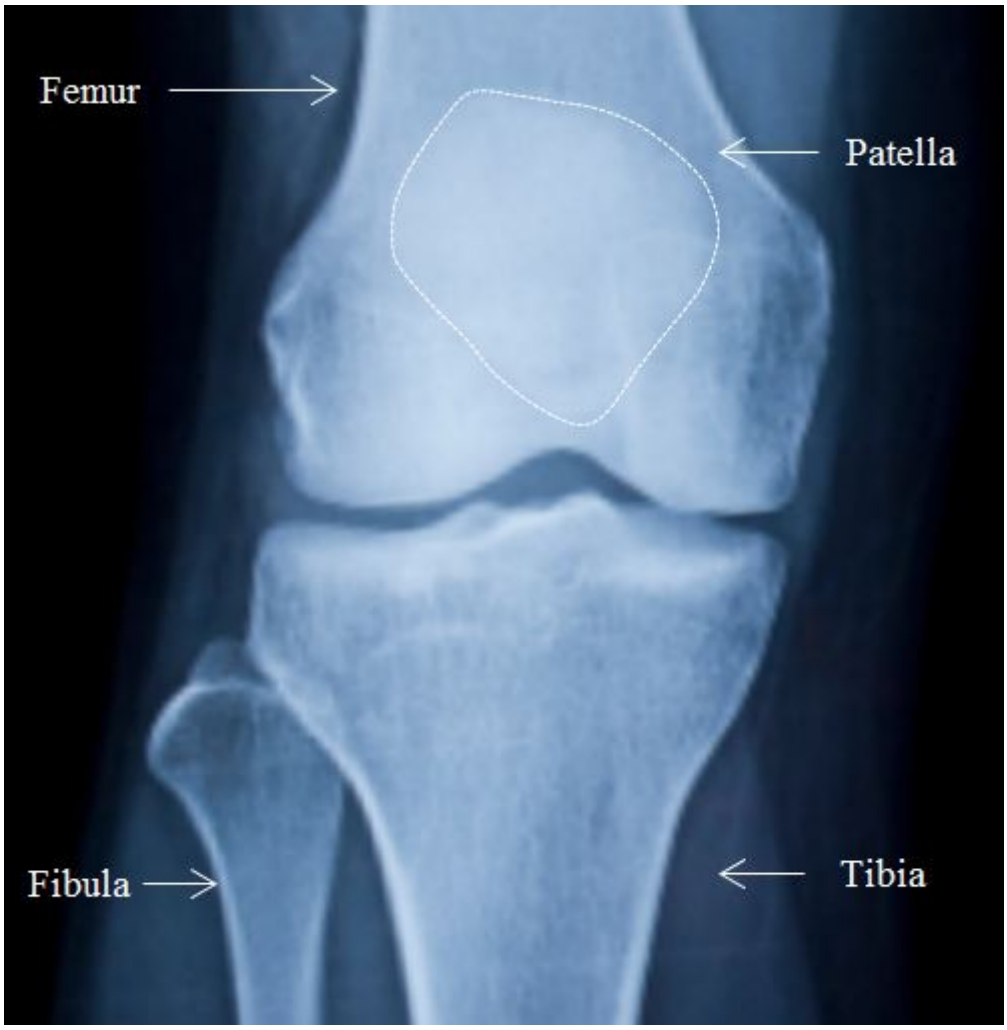

Figure 2.10: *Anterior-posterior X-ray radiography of the native patellofemoral joint. Note: this image is cropped from the C-arm fluoroscopic data collected in Nuffield Orthopaedics Hospital, Oxford with the ethical approval (08/H00606/114) in [88]*

.

However, X-ray radiography may fail to present the clear joint structure at least in one dimension of the three dimensional imaging if the patient have had a joint replacement.

As the prosthesis is highly radiopaque in the X-ray radiography images, the responses of real bony structures are obscured by the prosthesis as in Figure 2.11.

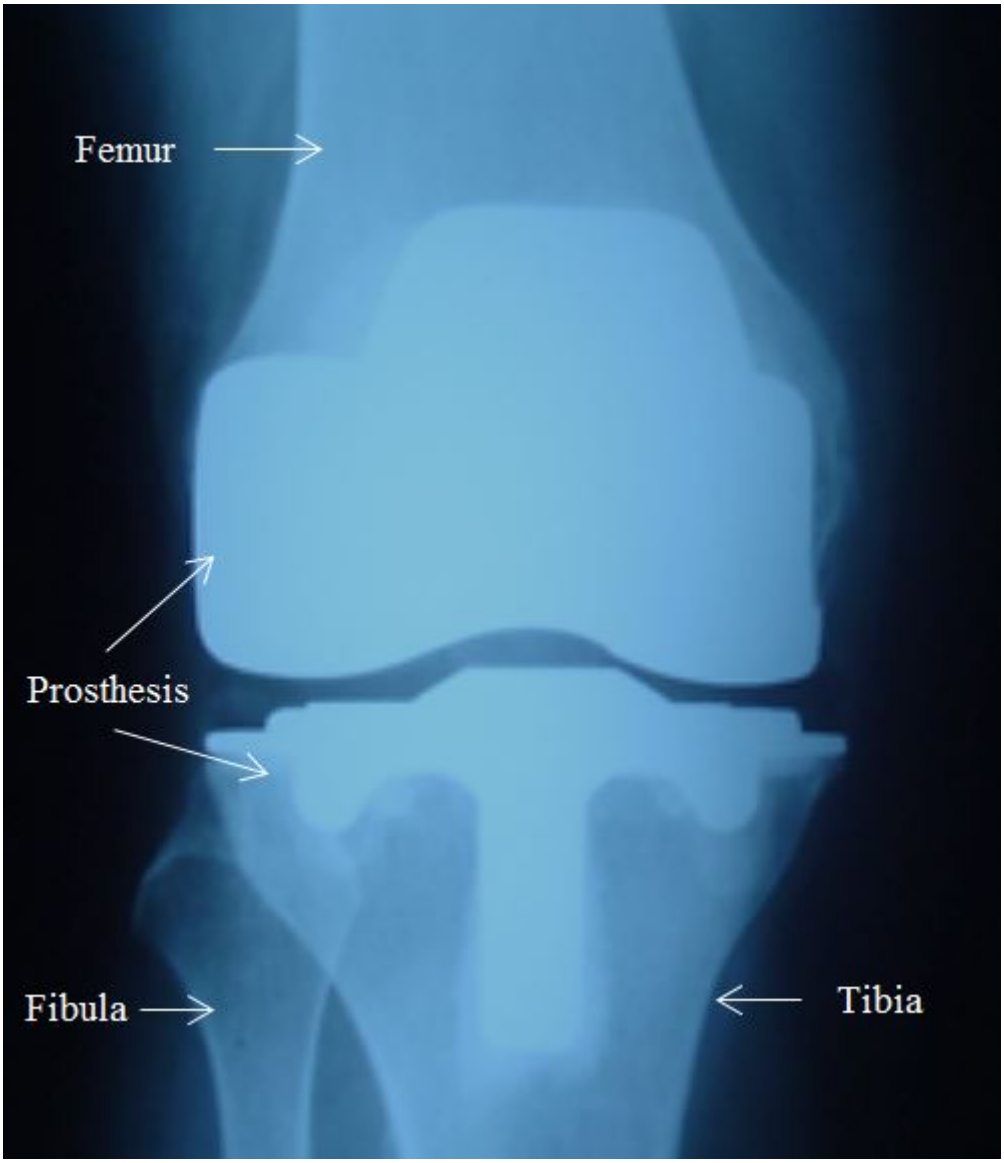

Figure 2.11: *Anterior-posterior X-ray radiography of the patellofemoral joint with joint replacement. Note: this image is cropped from the C-arm fluoroscopic data collected in Nuffield Orthopaedics Hospital, Oxford with the ethical approval (08/H00606/114) in [88].*

In Figure 2.11, the patella is obscured under the prosthesis compared to Figure 2.2.2. The prosthesis may also change the original shape of subject's bony structures.

In addition, X-ray radiography and fluoroscopy generate radiation, and excessive exposure to radiation is associated with the occurrence of certain forms of cancer in humans [88].

2.2.3 Magnetic resonance imaging

Magnetic resonance imaging (MRI) is based on the principle of nuclear magnetic resonance [47]. In clinical use, the MRI coil is composed of three layers, the primary magnetic coil, the gradient coil and the radio frequency (RF) coil, the first two of which generate a strong magnetic field [56]. The RF coil both generates and receives RF signals [56].

Hydrogen atoms are most-often used to absorb and emit RF signals. Since the human body is composed of 70% of water, hydrogen atoms naturally and abundantly exist in the human body, especially in soft tissues like skin (64%) muscle (79 %) and fat (83%) [86]. Thus, most MRI scans essentially map the location of these soft tissues in human body. RF signals excite the nuclear spin energy transition. By tuning the parameters of the signal sequence, the image contrast between different tissues vary based on the relaxation properties of the hydrogen therein.

Besides imaging the soft tissues, MRI has also been applied to investigate the musculoskeletal problems as in [6] [42] [70]. An example of an anterior-posterior T2 MRI slice of the hip joint is shown in Figure 2.12.

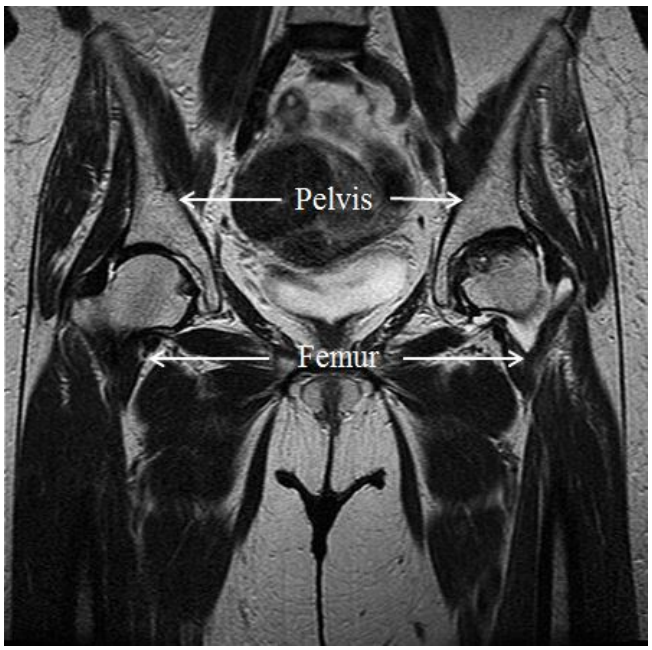

Figure 2.12: *Anterior-posterior T2 MRI of the hip joint. Note: this image is cropped from the T2 MRI data collected in Nuffield Orthopaedics Hospital, Oxford with the ethical approval (08/H00606/114) in [88].*

Compared to X-ray radiography, magnetic resonance imaging (MRI) is non-ionizing, non-invasive and it produces high quality images as well. However, it is difficult to detect bone edges especially at endplates and processes where soft tissues attach [70]. Moreover, a full diagnostic MRI scan of the femur segment takes around 20-30 minutes, which is time consuming and hard to measure dynamically. Another issue is that the bore of a typical MRI scanner is limited to 600 mm depending on its manufacture, which cannot provide a sufficient space for the subject to present a full range of motion of the hip joint.

Dynamic open MRI technology has been used to investigate the knee joint movements as in [55] [125]. An open MRI machine has a larger opening compared to a standard MRI machine. Some have magnets that do not completely surround a human being's body as in Figure 2.13. Open MRI technology is more flexible than the conventional coil MRI



Figure 2.13: *A subject standing within one open MRI system for dynamic measurement.Cropped from Figure.1 in [125].*

in data acquisition. However, the extra weight of the wearable coil affects the normal movements of the joint. To the author's knowledge, there is no literature focused on hip kinematics using open MRI.

2.2.4 Ultrasound

As a cheaper (comparing to MRI and CT), more dynamic and non-ionising imaging modality, ultrasound has been used as a real-time monitoring tool for different clinical diagnosis for over 10 years and is considered as a possible solution for imaging musculoskeletal conditions [83] [110] [115]. Despite being an effective modality to qualitatively describe how anatomy functions, when used quantitatively, ultrasound poses unique challenges. For example, an ultrasound image contains speckles as in Figure 2.14 and definition of landmarks is difficult.

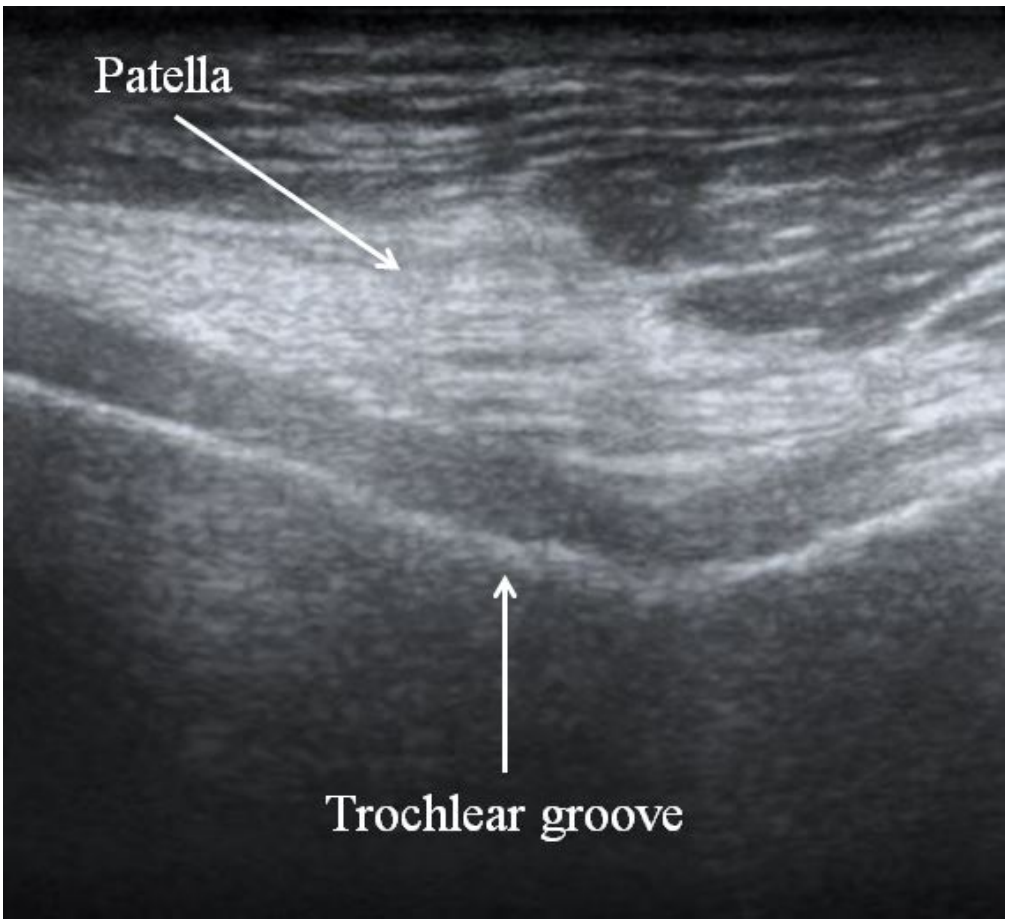

Figure 2.14: *A 2D ultrasound image of the patellofemoral joint.*

Researchers have attempted to quantify patella movements in the coronal plane during flexion using ultrasound; however, the measurement error has been reported to be up to 6.4 mm [54], which is a quite large error when compared with the subtle knee joint movements (maximum around 10 mm) [88]. Ultrasound alone does not give an accurate

result with an accepted tolerance. Moreover, only the area being covered by field of view can be imaged by ultrasound. Thus, an ultrasound device alone may not be desirable to provide a big enough footprint to capture all the information of interest.

2.2.5 Motion analysis with ultrasound

To not only detect the actual underlying bone structures but also provide more structural information in 3D space, Monk *et al.,* developed a motion analysis with ultrasound (MAUS) system to measure the difference in knee joint kinematics between normal subjects and people who had a knee joint replacement. The MAUS system is composed of a motion analysis system and a 2D ultrasound (US) system. It is non-ionising and can detect the actual underlying bony landmarks [88]. It relies on US to find the target bony landmark during movements. Meanwhile, the position information of the US probe is provided by the MA system so that bony structures in US images can be transformed into 3D space.

As the MAUS system detects actual underlying bony structures, it avoids the error cause by soft tissue artefact. A comparison between the underlying bony landmarks detected by the MAUS system and the results from the MA system is shown in Figure 2.15 demonstrating the difference between MAUS results and MA results caused by STA.

Although MAUS can monitor the movements of underlying bony landmarks, it is non-trivial to track closely related bone structures during movements. In order to acquire the data, the bony structures in US images are located manually by referring to a cross drawn on the US screen and the related bone structures are identified by eyeballing, which is extremely laborious and time consuming (approximately 30 minutes for one test). Moreover, the accuracy and the reproducibility of the MAUS system are highly dependent on an operator's experience to identify the same bony structure every time. Anyhow, the preliminary studies using MAUS inspire researchers to further improve the MAUS system for more practical clinical uses.

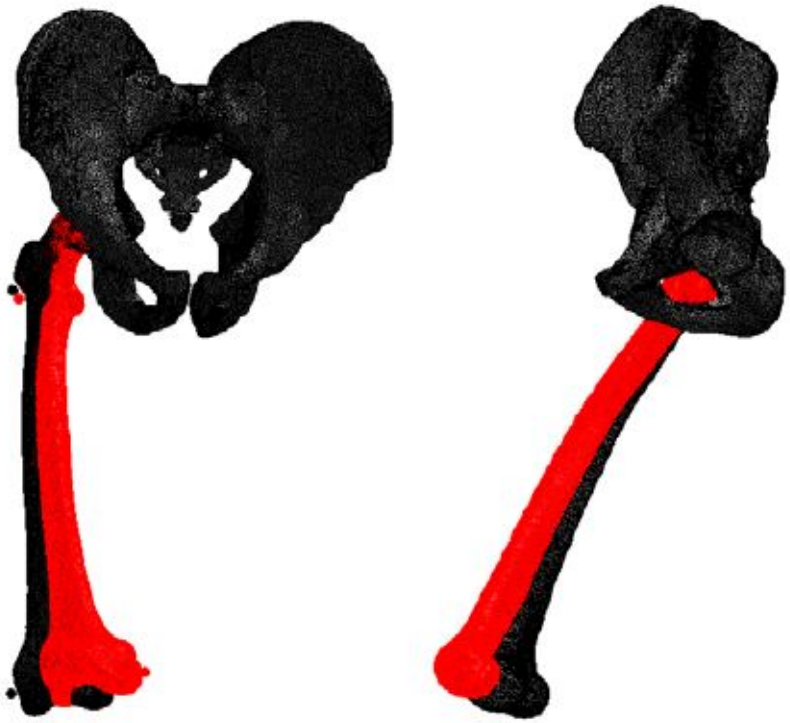

Figure 2.15: *Difference of the results from the MA system (black) compared to the MAUS results (red). Taken from [88].*

2.3 Summary

Musculoskeletal conditions encompass around two hundred different problems affecting the skeleton, joints, or muscles. Analysing a subject's gait pattern contributes to a better understanding of musculoskeletal pathology. The hip joint plays an important role in gait as the flexion and extension of the hip joint drive human body forward. Thus, quantification of hip joint kinematics during gait is scientifically significant. Single imaging modalities have been utilised, but have been found to have their own limitations for measuring joint kinematics. The combination of motion analysis with ultrasound shows its potential to monitor underlying bony structures. However, the accuracy of MAUS is highly dependent on the operator's experience. Thus, these techniques are not currently effective for describing the joint kinematics and not practical for clinical use. In the next chapters, a novel computer-aided tracking and motion analysis with ultrasound system will be described, which combines state-of-the-art computer vision knowledge with an augmented MAUS system to accurately and automatically quantify hip joint kinematics during gait.

Chapter 3

Augmented Motion Analysis with Ultrasound System

In this chapter, an augmented motion analysis with ultrasound (MAUS) is introduced including its construction, calibration and validation. As reviewed in Chapter 2, a motion analysis with ultrasound (MAUS) system [88] shows potential and has advantages for measuring bone movement compared to single diagnostic modalities. In order to transform all the information in a 2D ultrasound image into 3D space instead of targeting related bony structure by eyeballing, a multi-use calibration box is designed to spatially and temporally associate the ultrasound device with the motion analysis system for data acquisition. An automatic patch-based tracking algorithm to assist the validation of the calibration accuracy (Section 3.3.2) has been published in the proceedings of the *International Symposium on Biomedical Imaging, 2015* [66].

3.1 Computer-aided tracking and motion analysis with ultrasound system constitution

A computer-aided tracking and motion analysis with ultrasound system is composed of a computer-aided tracking pipeline and a motion analysis with ultrasound system (MAUS). The MAUS system shares common principles with 3D freehand ultrasound (US) imaging. A 3D freehand US system is comprised of a two-dimensional (2D) US scanner and a localizer. Different types of localizers can be attached to the US probe to provide its position and orientation information, such as a FARO mechanical arms [45], acoustic localizers [84], electromagnetic localizers [108] and optical localizers [88]. In this research, an optoelectronic motion analysis (MA) system (optical localizer), which is a group of infra-red cameras, 16 Cara cameras in this research (*VICON Motion Systems Ltd.*), is chosen because of its higher flexibility and accuracy compared to other types of localizers. These infra-red cameras can capture the positions of the retro-reflective markers placed on a test subject in 3D global space. The MA system is calibrated before experiments by tracking a "T" shaped wand while it is waved in the capture volume, the 3D space surrounded by the infra-red cameras. A LOGIQ S7 (*GE, USA*) US scanner is used with a ML 6-15 transducer to image the target bony structure. Markers are attached to a 3D printed bespoke thermoplastic probe cover to provide location information of the US probe during the scan. The acquired data from both the MA system and the US device are imported into a PC (*8-core Intel Core i7-4770 3.40 GHz running a 64-bit Windows OS*) for image-based computer-aided post-processing (described in Chapters 4, 5 and partly 6). The system setup is shown in Figure 3.1.

3.2 Calibration

In order to transform 2D US information into the actual 3D space using the MAUS system, calibration is essential to correctly align data from the motion analysis system

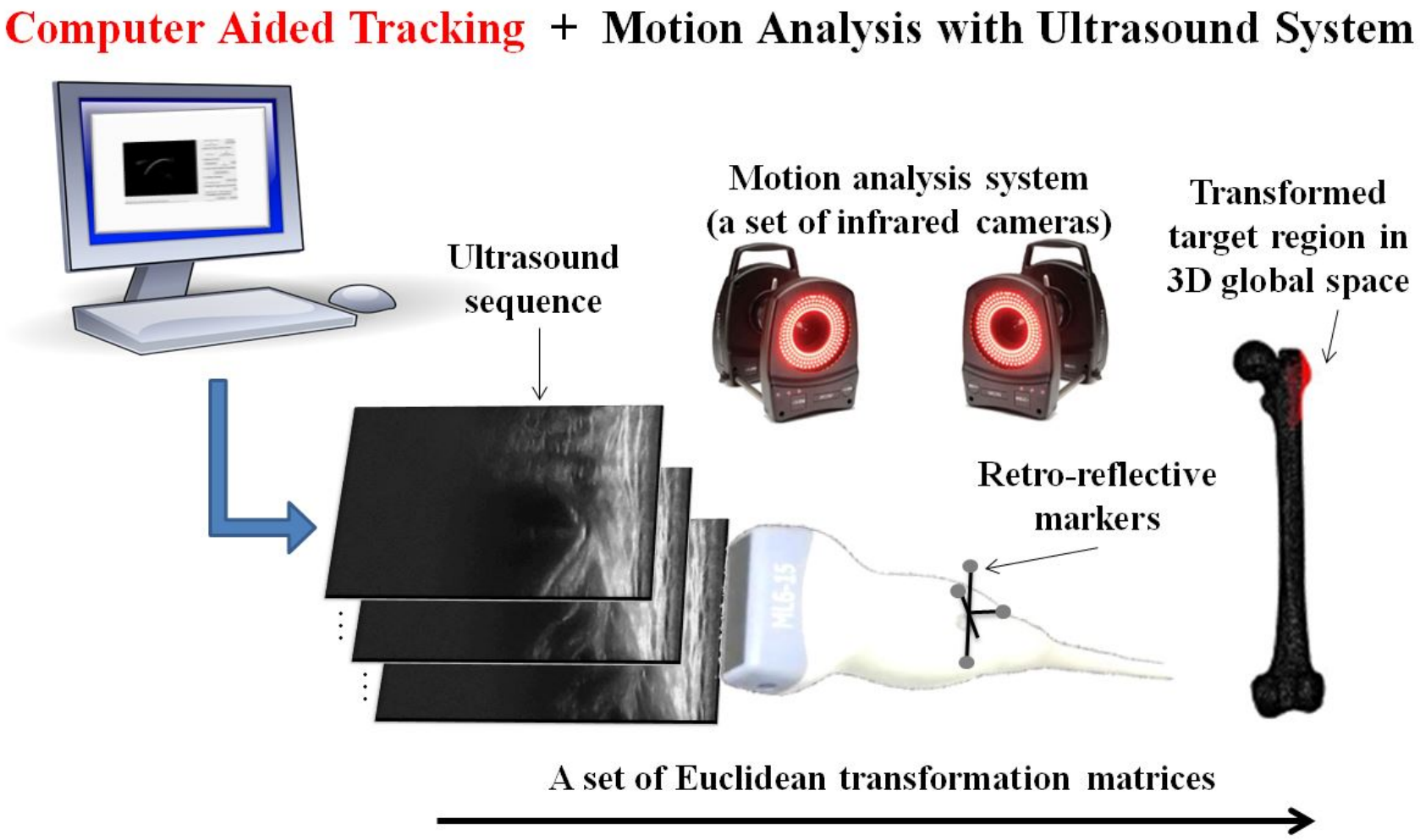

Figure 3.1: *A schematic of the computer-aided tracking and motion analysis with ultrasound system.*

and the ultrasound device spatially and temporally. Firstly, the location and the amount of US image distortion need to be identified and corrected. Then, spatial calibration has to be performed to calculate the transformation matrix, including rotations and translations, in the spatial domain so that the US images can be transformed from the US local coordinate system to the 3D global coordinate system. Last but not least, the synchronization between MA and US is achieved by temporal calibration.

3.2.1 Previous calibration methods

Since MAUS shares similar principles with 3D freehand US, previous calibration methods employed for 3D freehand US are applicable to MAUS.

For the image distortion assessment, Monk *et al.,* [88] used a metallic cuboid which was inserted in 9 different positions in a water tank and ultrasound was used to detect the average length and width of the block with both 50% and 100% signal power to inspect the US image distortion in two dimensions. It was reported that there were no significant ultrasound image distortions with altering positions or signal strengths [88]. However, the block was only built for one particular probe with a field of view slightly bigger than the length of the block. Thus, this result was only validated for a given probe with a certain size of field of view. Other blocks may need to be built for other probes with different fields of view and new assessments would have to be carried out.

Spatial calibration has been done in different ways. To the author's knowledge, all types of previous phantom were built for use within a container filled with coupling medium, such as degassed water or gel, for ultrasound imaging. State *et al.,* designed a single point phantom based on imaging a tiny spherical object [128]. A single cross-wire phantom [29] has been designed using two intersecting wires. Xiao *et al.,* developed a similar single cross wire phantom in which two wires were intersected in the equator plane of a Ping-Pong ball [142]. However, the accuracy of these two types of phantom is highly related to how well the point is targeted, and manual detection of target points is extremely laborious [108]. A multiple cross-wires phantom [60] that forms a triangle

shape and a 2D shaped alignment phantom [120] have also been attempted, however, those shapes must be manually segmented. A Z-fiducial wire phantom [57], which intersects the ultrasound image plane, has been used and are similar to the method introduced in this chapter. There are other methods for calibration, such as the wall phantom using a single wall designed by Prager *et al.,* [108]. However, these led to specular reflection problems which means that most US beams will be reflected away from the probe when the probe was not held perpendicular to the wall.

Regarding temporal calibration, it is crucial in the current research. For some of the 3D freehand ultrasound techniques [29] [128] and previous MAUS technique [88], both the position of the probe and the position of the tested subject are captured in static or quasi-dynamic status. Thus, the temporal relationship between the ultrasound and the motion analysis system is not essential and is ignored. A random sudden movement of the probe is normally induced in the probe position to set a start and an end of one time period [107] [132] [133]. However, such a method can only achieve an accuracy of $\pm\frac{(t_{US}+t_{MA})}{2}$, where t_{US} and t_{MA} represent the time interval between two frames in the ultrasound and the motion analysis system respectively. Gooding *et al.,* designed a button to make sure the two systems trigger simultaneously, and a calibration box with a horizontal slide on which the ultrasound probe can be fixed [45]. It was used to detect the position of the target point when the probe is moved along the guide rail [45]. However, the target point can still be seen if the probe has a slight tilt. Moreover, slight vibration affects the accuracy of temporal calibration. More detailed reviews of the calibration methods can be found in [61] [84].

3.2.2 Design of multi-use calibration box

In order to conduct calibration of the MAUS system more efficiently and accurately, a multi-use calibration box was designed in SolidWorks 2012 (*Dassault Systems SolidWorks Corporation, USA*).

The calibration box was a 300 mm length × 300 mm width × 150 mm tall water tank

made of Polyvinyl Chloride plastic with a 200 mm length × 100 mm width window on the anterior surface. A detailed box design can be found in Appendix B. Four retro-reflective markers were attached to the four corners of the calibration box to locate the box position within the motion analysis laboratory precisely. If the calibration box was moved during the experiment, this four markers can be used to correct the displacement. Two linear guide rails (*TS-04-15-300 T, Igus*) were mounted on the left and right edges of the box (Figure 3.2).



Figure 3.2: *Multi-use calibration box.*

Two wall sections of thickness of 5 mm with rectangular cut-out windows in the middle were mounted on the horizontal sliding frames, screwed onto the carriers for the guide rail and aligned with the box window. The distance between the two frames was 5 mm. As the depth of the field of view of the ultrasound probe was limited, it was ensured

that the first sliding frame was flush with the inner side of the window to save space when the frame was moved away from the window. Two pairs of metal cross wires were fastened on the front frame and three on the back. The distance between two adjacent cross points on the same frame was 10 mm (Figure 3.3). Five 2 mm diameter retro-reflective markers were attached to the top surfaces of the front and back sliding frames to signify the position of the five crosses. The distance between these five markers and their corresponding crosses was 90 mm. The position of these five markers were measured by the motion analysis system and their correspondence to the five cross wires imaged by US provided the ground truth.



Figure 3.3: *Five pairs of metal cross wires on two frames with rectangular cut-out windows in the middle.*

3.2.3 Image distortion assessment

Ultrasound images can suffer from geometrical distortion because of variable speeds of the US wave during propagation or the US generation from a sector shaped transducer [14] [100]. Image distortion assessment is not necessary for qualitative clinical identification, but is an issue where an accurate quantitative measurement is a requirement. In order to test the image distortion of US images with the multi-use calibration box, the US probe was clamped at a fixed position, where all the cross-wires can be captured in the US image, so that the distances between each two of those five crosses can be calculated from the crosses' positions imaged by US (Figure 3.2). The calibration box was filled with degassed water as coupling medium for US imaging.

Then, the flexible frame, on which the metal frames were mounted, was stopped after moving 1 mm, 2 mm and 4 mm respectively, which is shown as "FM" in the second column of Table 3.1. The movement of crosses was captured by the US probe. Meanwhile, the five markers on the sliding frames were captured and located in 3D space by MA. The US depth was set to 45 mm, 60 mm and 90 mm, and the US was triggered at power settings of 50% and 100% respectively (USP in Table 3.1). Crosses in the US image were manually selected. The distance (Dis) between the two crosses in the frame and the movement (Mov) of the left cross in the first frame were then calculated. Table 3.1 shows the maximum image distortion error is ± 0.14 mm (two pixels) in both horizontal and vertical directions which shows no significant lateral and axial image distortion along the US propagation.

3.2.4 Spatial calibration

The aim of spatial calibration is to find the transformation matrices to transform the points in the 2D local US image coordinate system into the 3D global coordinate system by referring to the tracked US probe positions captured by MA. As US can suffer from

USP (%)	FM (mm)	US depth of 45 mm		US depth of 60 mm		US depth of 90 mm	
		Dis(mm)	Mov(mm)	Dis(mm)	Mov(mm)	Dis(mm)	Mov(mm)
50	1	9.93	0.93	10.07	0.93	10.07	0.93
	2	9.86	1.93	9.93	2.00	9.93	1.86
	4	10.14	3.86	10.00	4.07	10.07	3.93
100	1	10.00	0.93	9.93	1.07	10.14	0.93
	2	10.07	1.93	10.07	2.07	9.86	2.00
	4	9.86	4.14	9.93	3.93	10.07	4.07

Table 3.1: *Ultrasound image distortion analysis with different ultrasound powers (USP) after moving the frame to different positions (FM).*

beam thickness artefact [117], the crosses can be imaged as small dots only when the middle scanning plane (Orange plane in Figure 3.4) intersects all five crosses, i.e. the middle scanning plane coincides with the co-plane formed by the five crosses. If the

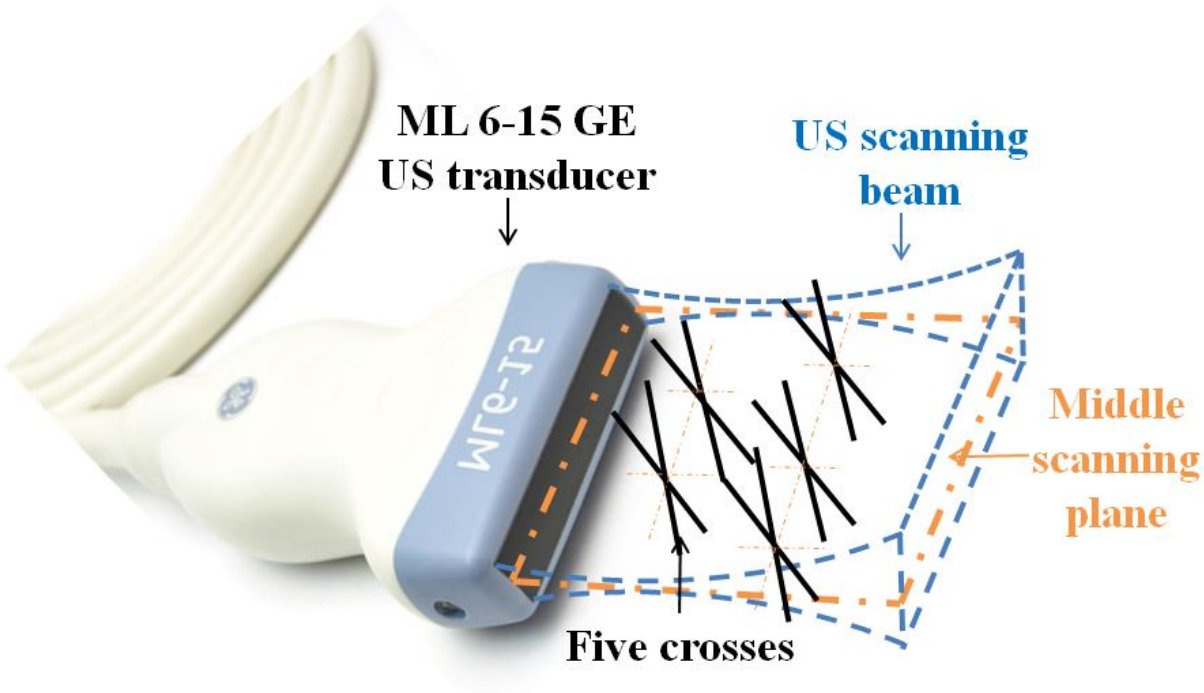

Figure 3.4: *Schematic of spatial calibration.*

middle scanning plane is slightly tilted, the crosses present as dots with long tails shown in Figure 3.5a while the image contains ten dots if the middle scanning plane doesn't intersect any of those five crosses shown in Figure 3.5b.

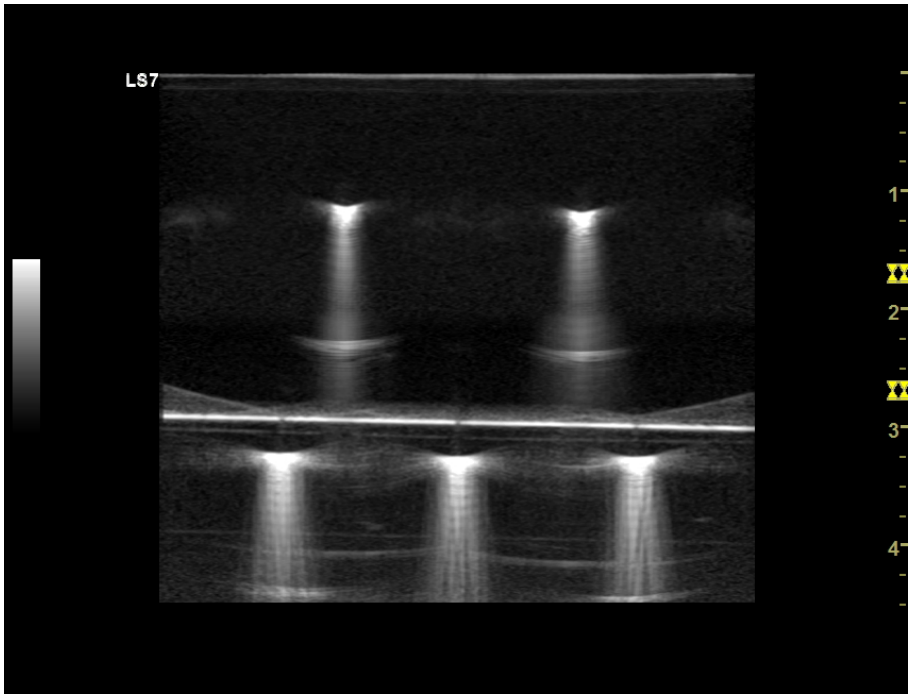

(a)

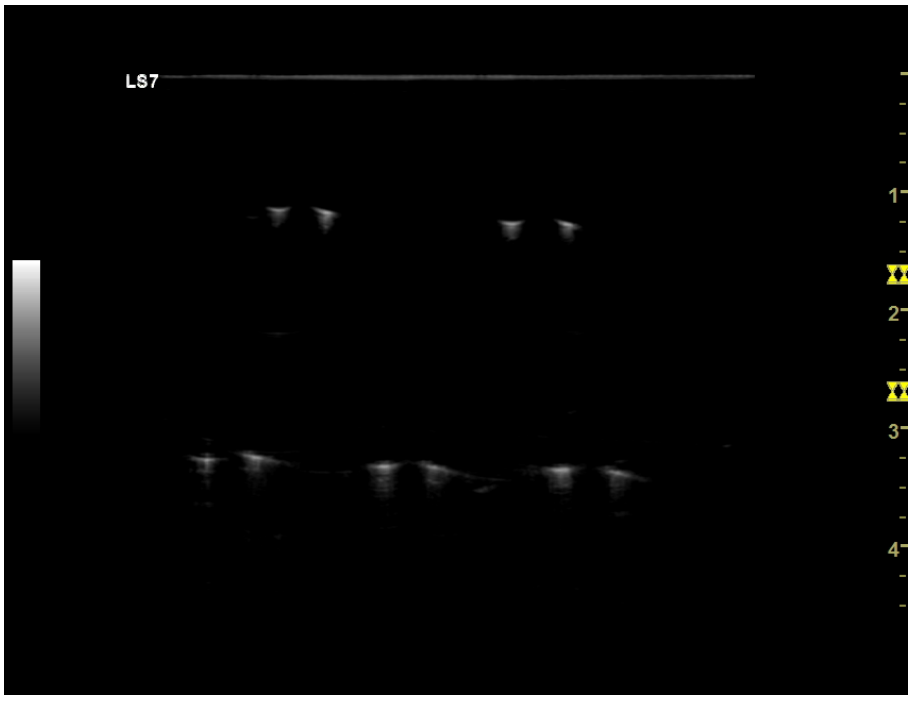

(b)

Figure 3.5: *Two representations of the cross-wires under US when the US image mis-aligned with the cross-wires plane.*

Thus, the US probe is adjusted and clamped when all the five crosses are imaged clearly as smallest dots without tails in the US image as in Figure 3.6.

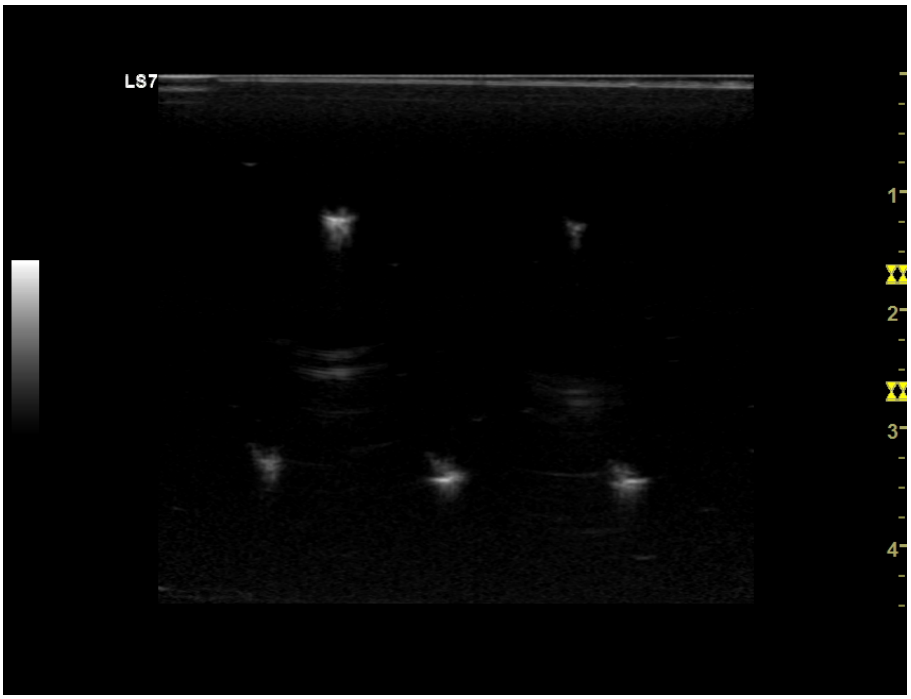

Figure 3.6: *Representation of the cross-wires under US when the US image well-aligned with the cross-wires plane.*

Ultrasound images are cropped into images with a size of 500 × 562 to get rid of the boundary of US images. The pixel (1,1) of the cropped US image is set as the origin of the ultrasound local coordinate system (ULCS). The X_{ulcs} axis of the ULCS is defined as the axis pointing from the origin to the last column of the first row, the Y_{ulcs} axis of the ULCS is pointing from the origin to the last row and the Z_{ulcs} axis is perpendicularly pointing into the US images as in Figure 3.7a. Because an US image is two dimensional, the Z_{ulcs} values of all the pixels in the US image are set to 0s. The mass centres of each cross in the US image are then found to match the position of these five markers captured by MA. The markers attached on the probe and the sliding frames are captured by MA and form the probe local coordinate system (PLCS) and cross-wires local coordinate system (CLCS) respectively. For the PLCS, the origin is defined as the mid point of the left and right markers. The Y_{plcs} axis is pointing from the origin to the right marker, the Z_{plcs} axis is perpendicularly pointing out the plane formed by the origin, the right and tail

markers, and the X_{plcs} axis is perpendicular to Y_{plcs} axis and Z_{plcs} axis shown in Figure 3.7b. Similarly, for the CLCS, the origin is defined as the mid point of the F1 and F2 markers. The Y_{clcs} axis is pointing from the origin to the F2 marker, the Z_{clcs} axis is perpendicularly pointing out the plane formed by the origin, the F2 and B2 markers, and the X_{clcs} axis is perpendicular to Y_{clcs} axis and Z_{clcs} axis shown in Figure 3.7c.

The transformations from coordinate system a to coordinate system b are denoted by $T_{b\leftarrow a}$, where the subscripts indicate the direction of the transformation which should be read from right to left. The rotations are represented by the matrix Rot, with subscripts indicating which axis the rotation is around. The translations are denoted by the matrix Tsl.

In order to meet the requirement of matrices multiplication, the 4 $\times$ 4 rotation matrices and translation matrix are calculated as in Equation (3.1) and (3.2) respectively.

$$Rot_Z = \begin{bmatrix} \cos\theta & -\sin\theta & 0 & 0 \\ \sin\theta & \cos\theta & 0 & 0 \\ 0 & 0 & 1 & 0 \\ 0 & 0 & 0 & 1 \end{bmatrix} \quad Rot_X = \begin{bmatrix} 1 & 0 & 0 & 0 \\ 0 & \cos\alpha & -\sin\alpha & 0 \\ 0 & \sin\alpha & \cos\alpha & 0 \\ 0 & 0 & 0 & 1 \end{bmatrix} \quad Rot_Y = \begin{bmatrix} \cos\beta & 0 & \sin\beta & 0 \\ 0 & 1 & 0 & 0 \\ -\sin\beta & 0 & \cos\beta & 0 \\ 0 & 0 & 0 & 1 \end{bmatrix} \tag{3.1}$$

where α, β and θ are rotation angles around the X, Y and Z axis respectively.

$$Tsl = \begin{bmatrix} S_X & 0 & 0 & d_X \\ 0 & S_Y & 0 & d_Y \\ 0 & 0 & S_Z & d_Z \\ 0 & 0 & 0 & 1 \end{bmatrix} \tag{3.2}$$

where d_X, d_Y and d_Z are the translations along the X, Y and Z axes respectively. S_X, S_Y and S_Z are the scaling factors of the X, Y and Z axes respectively.

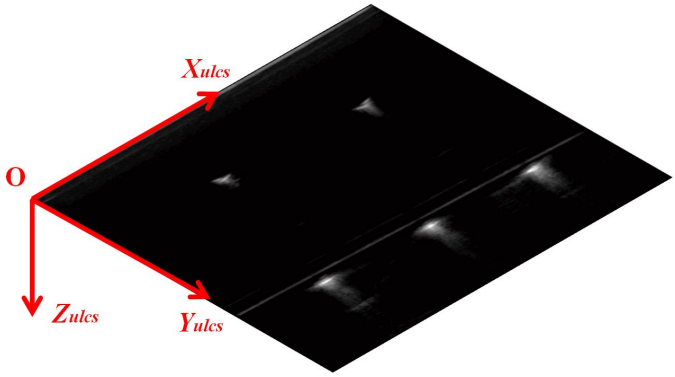

(a)

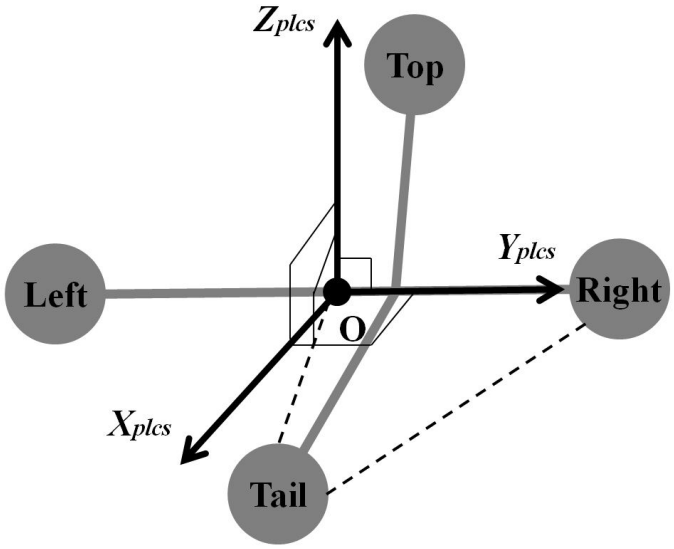

(b)

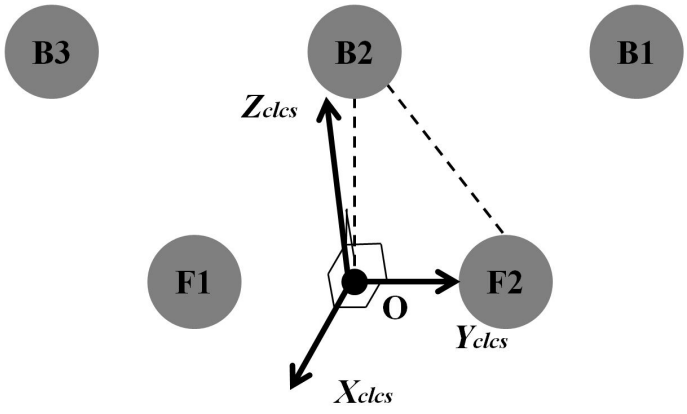

(c)

Figure 3.7: *Local coordinate systems, a) ultrasound local coordinate system (ULCS), b) probe local coordinate system (PLCS) and c) crosses local coordinate system (CLCS).*

The 4×4 transformation matrix from coordinate system a to coordinate system b is calculated using Equation (3.3):

$$T_{b \leftarrow a} = Rot_Z \cdot Rot_X \cdot Rot_Y \cdot Tsl \tag{3.3}$$

In the augmented MAUS system, all the points in an US image (i.e. ULCS) are transformed into the global coordinate system (GCS) so that the manually drawn cross-hair on the US screen of the previous MAUS system to locate the bony structure can be gotten rid of. Firstly, based on the cross wire positions in both US and MA, an US point $(x_{ULCS}, y_{ULCS}, 0)$ in ULCS can be transformed into CLCS with a transformation matrix $T_{CLCS \leftarrow ULCS}$. Since the positions of the probe and the metal cross wires in GCS are known, the transformation matrix between CLCS and PLCS, $T_{PLCS \leftarrow CLCS}$, and the transformation matrix between PLCS and GCS, $T_{GCS \leftarrow PLCS}$, can be calculated. A transformation relationship map is shown in Figure 3.8. The blue boxes in Figure 3.8 represent

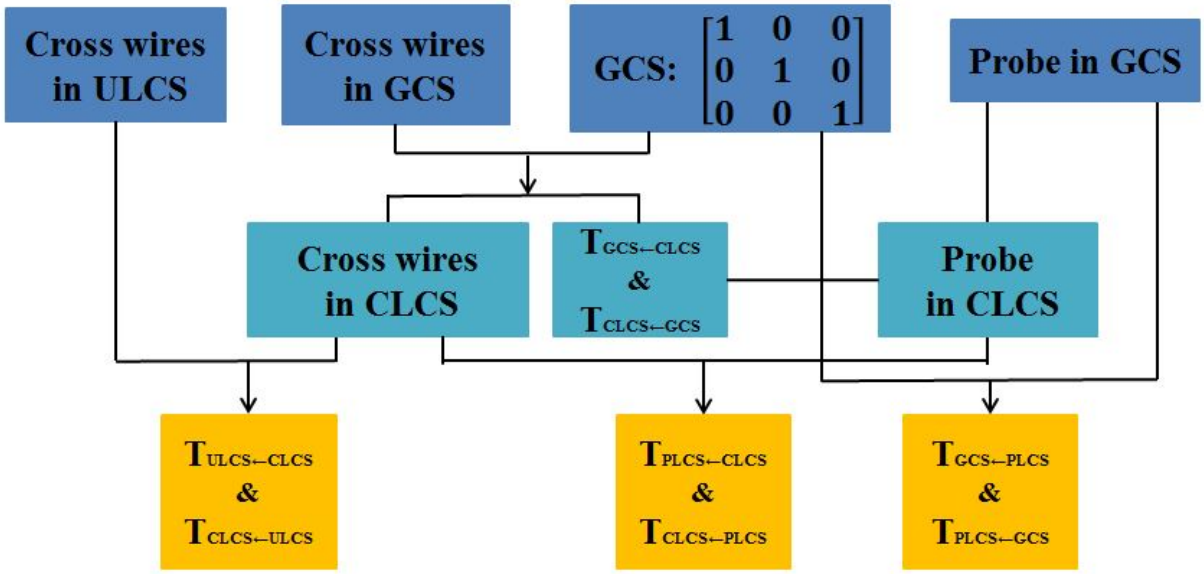

Figure 3.8: *Transformation relationship map of spatial coordinate systems.*

the known information, the cyan boxes are intermediate information and the orange boxes are the final transformation matrices to transform an US point $(x_{ULCS}, y_{ULCS}, 0)$ into the

3D GCS as in Equation (3.4).

$$\begin{bmatrix} x_{GCS} \\ y_{GCS} \\ z_{GCS} \\ 1 \end{bmatrix} = T_{GCS \leftarrow PLCS} \cdot T_{PLCS \leftarrow CLCS} \cdot T_{CLCS \leftarrow ULCS} \cdot \begin{bmatrix} x_{ULCS} \\ y_{ULCS} \\ 0 \\ 1 \end{bmatrix} \tag{3.4}$$

Where $(x_{ULCS}, y_{ULCS}, 0)$ is the point coordinates in ULCS. As the ultrasound image is two dimensional, the third coordinate of an US pixel is set to zero. $(x_{GCS}, y_{GCS}, z_{GCS})$ is the transformed point coordinates in GCS.

3.2.5 Temporal calibration

In order to transform a 2D US image into the 3D GCS based on the tracked probe positions, synchronization between the US and MA system is essential to match a given US frame to the corresponding probe position in the sequence captured by MA. However, the sampling frequencies of the US and MA systems are different. Therefore, without temporal calibration, the US frames incorrectly coincide with the probe positions captured by MA, which results in erroneous spatial transformation estimation [84]. Thus, the MA data have to be resampled so that a continuous synchronized US-MA data set can be obtained. To get the resampling rate, temporal calibration is conducted by manually sliding the cross-wire frames, which is similar to the method in [45].

The temporal calibration set up is shown in Figure 3.2. Firstly, after triggering both the US and MA system, the sliding frame is suddenly moved. Then, after a pause of a few seconds, the sliding frame is suddenly moved again. During the movement, the cross wires should always be within the US image field of view so that the whole movement can be captured by both US and MA. The starts of the two sudden movements from both US video and MA data are found and labelled as the start and end of a time period T. The frame numbers of both US and MA during time period T are counted and denoted by

N_{US} and N_{MA} respectively. The time intervals between two adjacent ultrasound frames t_{US} and two continuous positions of the probe captured by the motion analysis system t_{MA} can be calculated by Equation (3.5).

$$t_{US} = \left(\frac{T}{N_{US}}\right); \quad t_{MA} = \left(\frac{T}{N_{MA}}\right) \tag{3.5}$$

The mth position of the probe captured by MA and the nth frame in the US video are denoted by m^{th}_{MA} and n^{th}_{US} respectively. A position of the probe can be calculated to match a given US frame by satisfying Equation (3.6).

$$m^{th}_{MA} = \left(\frac{t_{MA} \cdot n^{th}_{US}}{t_{MA}}\right) \tag{3.6}$$

However, occasionally, the probe position m^{th}_{MA} is not an integer. The result is rounded by Gaussian rounding [116] so that it is guaranteed the maximum temporal error is $\frac{t_{MA}}{2}$.

3.3 Validation

3.3.1 Validation setup

The accuracy of the spatial and temporal calibration was validated using a proximal femur model shown in Figure 3.9. Five non-coplanar retro-reflective markers were attached to the femur model with one marker attached on the greater trochanter (GT). Then the femur model was inserted into the water tank with degassed water, submerging the marker on the GT but leaving the rest visible above the water (Figure 3.9). The femur model was manually rotated around a fixed axis that goes through the femoral head and was in line with the long axis of the femur. Only the four markers above the water line can be captured by the MA system during the manual rotation. A US probe was clamped at a fixed position where the GT marker can be imaged during the rotation as in Figure 3.10a. The positions of the other twelve markers on the femur (yellow segment), the

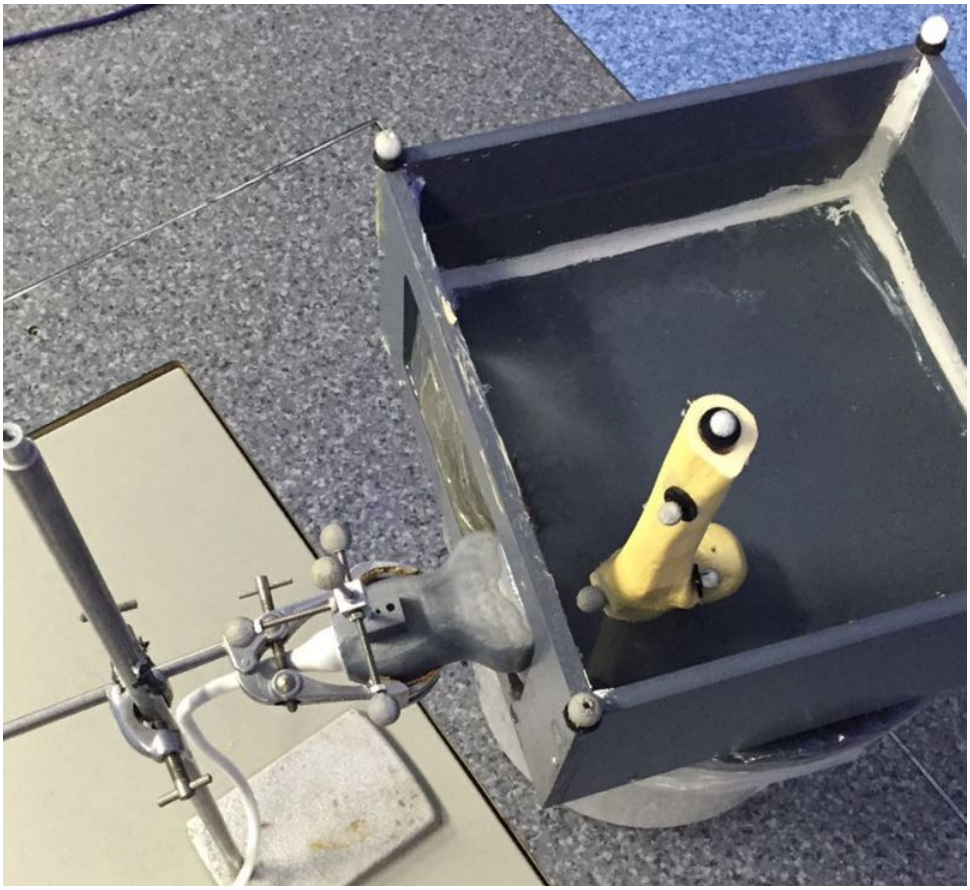

Figure 3.9: *Experimental setup for validation of spatial and temporal calibration with a proximal femur model.*

water tank (blue segment) and the probe (red segment) were captured by the MA system as in Figure 3.10b.

The femur was rotated such that the femoral head moves from the right most position to the left most position within the US field of view. As the femur model is a rigid body, the GT marker can be reconstructed from the positions of the other four markers on the femur captured by the MA system at a sampling frequency of $100Hz$. Meanwhile, the position of the GT marker can be captured by the US device at a sampling frequency of $32Hz$ in water through the membrane window and later transformed into the 3D GCS. In order to locate the GT marker in the US video, a patch-based tracking algorithm was employed and described in Section 3.3.2.



(a)

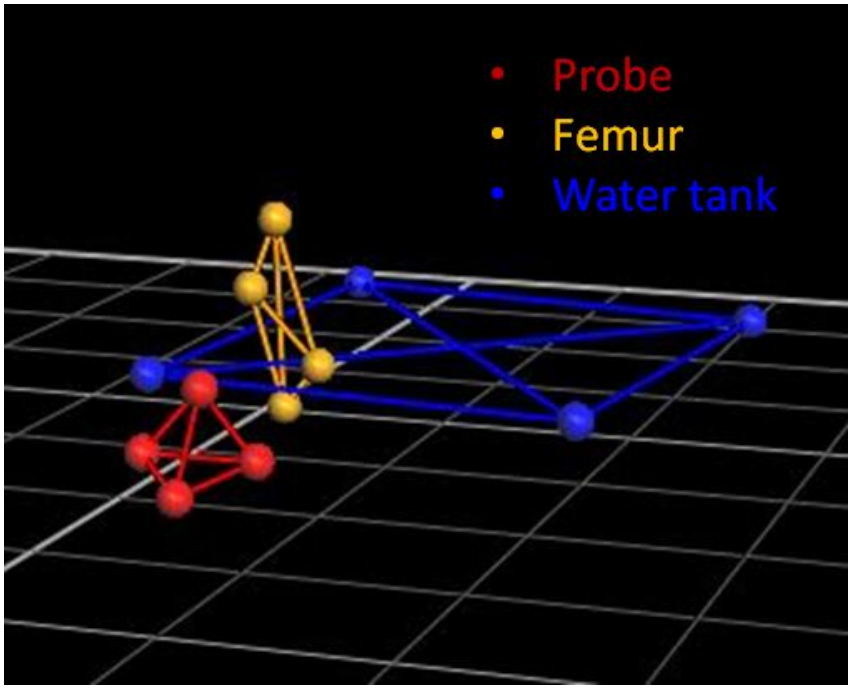

(b)

Figure 3.10: *Data of the validation experiment of spatial and temporal calibration, a) cropped US image of the GT marker and b) markers captured by MA system.*

3.3.2 Patch-based tracking

In order to quantify the Euclidean distance between the measurements of the GT landmark location from the rigid body reconstruction and the MAUS system, the GT has to be located in each frame throughout the US video of the femur phantom rotations, each of which includes around 200 - 300 frames. In the work carried out by Monk [88], the target point in every frame was picked manually, which was a less accurate and extremely laborious process.

Some early work on object tracking in videos of natural scenes has been described by Kanade *et al.,* [79] [131] (referred to here as the KLT tracker). These algorithms, adapted from optical flow, are suited to small motion tracking. Mean-shift is another commonly used approach where a shift vector from the feature of initialized patch of interest to the mean value of a the target patch feature throughout frames is found [24]. This approach is however sensitive to initialization [18].

In this subsection, a US key feature tracker is introduced in four steps. A schematic diagram of the patch-based tracking algorithm is shown in Figure 3.11.

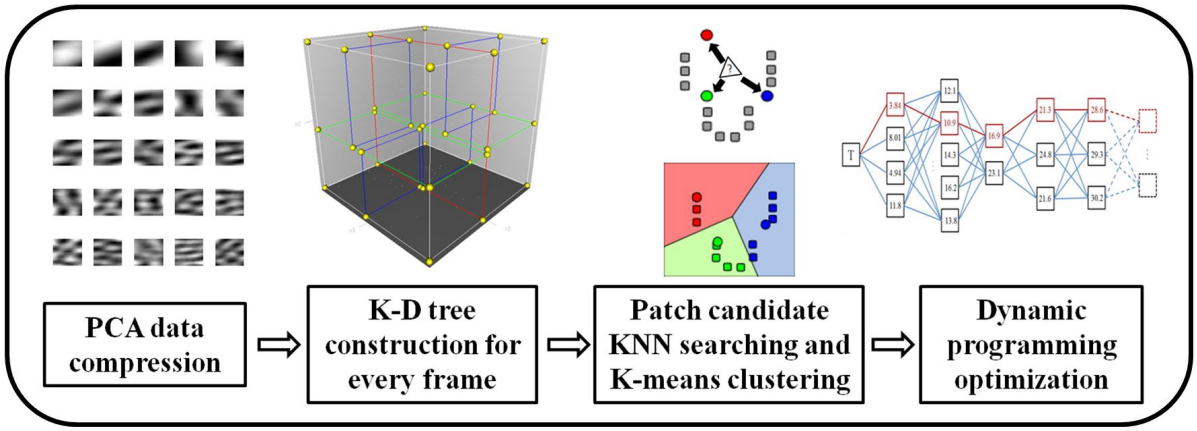

Figure 3.11: *Schematic diagram of patch-based tracking.*

Firstly, all the patches in the ultrasound video are compressed to shorter vectors (descriptors) using principal components analysis (PCA) [130]. The principal components are obtained from a large set of randomly selected patches over the whole sequence. Then a K-D tree is built for every frame for later query. Instead of finding the motion vectors

iteratively between two frames, as with mean shift and KLT trackers, match candidates with similar compressed image intensity profiles are sought independently in each frame by querying the K-D tree of each frame. The similar tracked nodes are clustered to retain the best representation of each cluster. Lastly, dynamic programming [146] is used to find the optimal tracking locations.

• Target patch selection

A target square patch is selected manually in the first frame as a tracking template. As the selected patch needs to enclose the target structure, the size of the selected patch is determined by the size of the target structure. In order to show this algorithm can be used in a generic case, an US video of a femur model is used instead of a circular marker, one frame of which with a selected patch is shown in Figure 3.12.

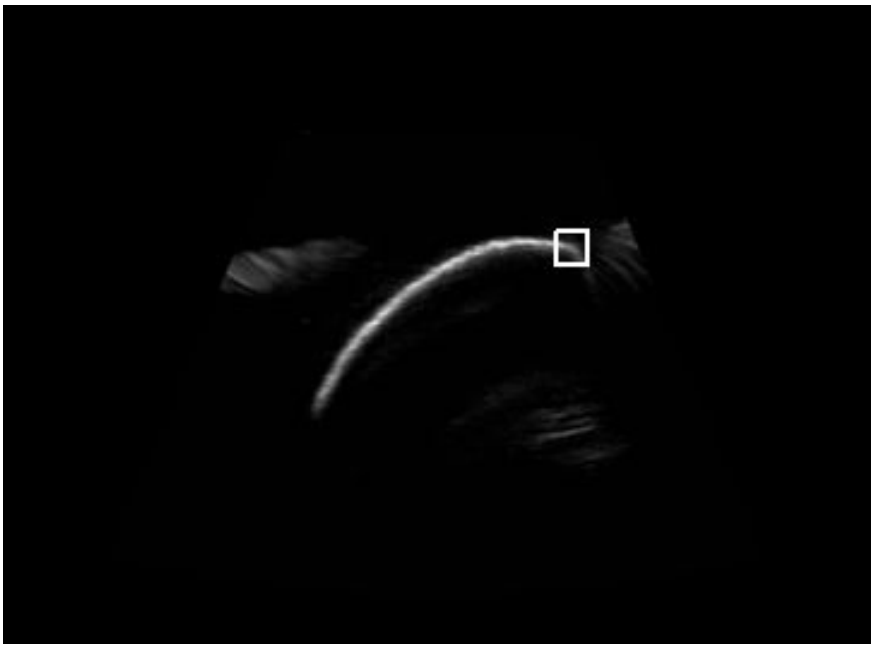

Figure 3.12: *US image of a proximal femur with a selected patch (white box).*

To select the target patch in the US video, the size of the target patch was optimized as in Figure 3.13. The tracking results with a given sized patch are compared to the manually picked ground truth. A Euclidean distance error threshold is set to ±1 mm (around 10 pixels in the ultrasound image), which is the clinical tolerance of computer-aided orthopaedics surgery (±1 mm) [21]. The amounts of incorrect tracked frames with

an Euclidean distance error larger than the threshold were counted for different patch sizes over 10 videos as shown in Figure 3.13. The deviations of incorrect tracked frame number of tracking errors over 10 videos are also shown in Figure 3.13. An optimal 30×30 patch is chosen. The intensity feature of one 30×30 patch is reformatted as a 900-element column vector. Every frame has around 275 thousand possible patch candidates (around 250 million elements). Carrying out an exhaustive search within the size of the US frame (500×562) is computationally expensive but gives minimal error.

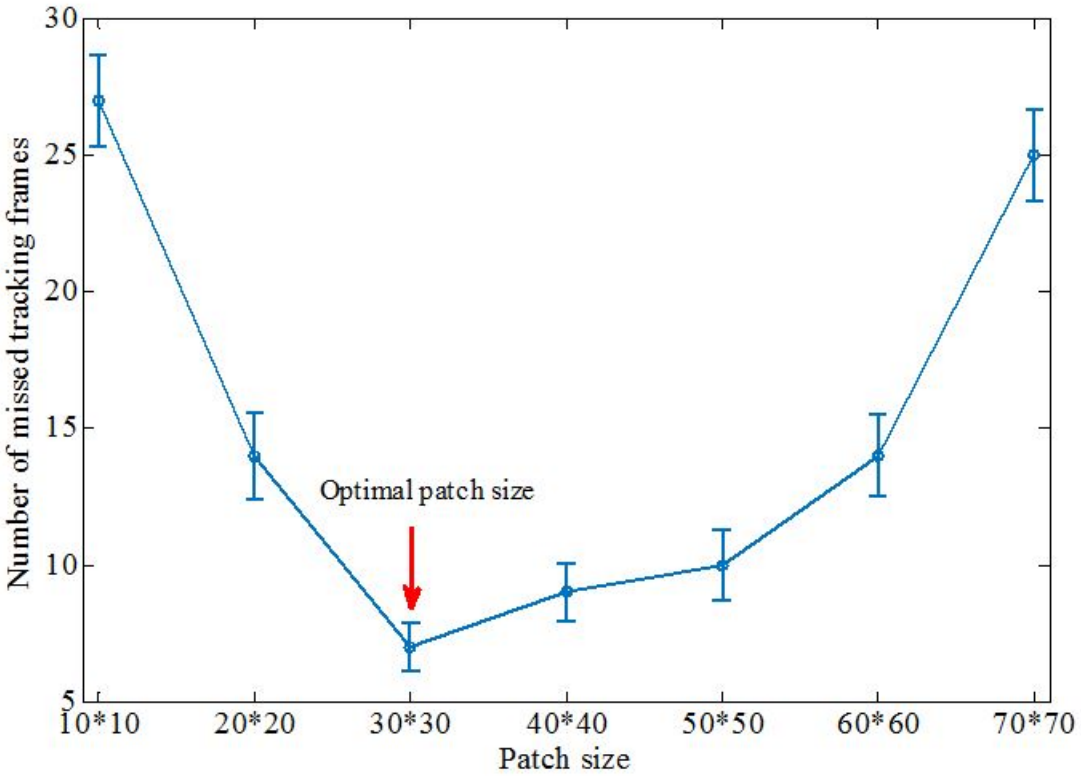

Figure 3.13: *Number of incorrect tracked frames with different patch sizes in a single ultrasound video and the deviation of number of incorrect tracked frames over ten videos.*

• Data compression

In order to reduce the dimension of the patch descriptor, principal component analysis (PCA) is applied to find the linearly uncorrelated principal components so that the original vector can be compressed to a shorter vector by being projected on the first few of these uncorrelated principal components [17]. PCA converts a set of possibly correlated observations into a set of linearly uncorrelated variables called principal components by

an orthogonal transformation [51]. PCA data compression guarantees that the projected data on the first principal component have the largest variance. To build up the principal components, a large number of patches are randomly selected throughout the US video, and the first M principal components are selected as the projection base. Five thousand patches were randomly selected as more patches number returned very similar results. Then, the patch vectors in every frame are projected to the first M principal components. However, if a large M is chosen, the compressed patches would take more storage and more time in the K-dimensional (K-D) trees construction described in the next part. Similar to optimizing the patch size, the number of missed tracking frames with different numbers M of principal components (blue line in Figure 3.14) and the elapsed time for building the K-D trees, with the compressed data (red line in Figure 3.14) are compared in Figure 3.14.

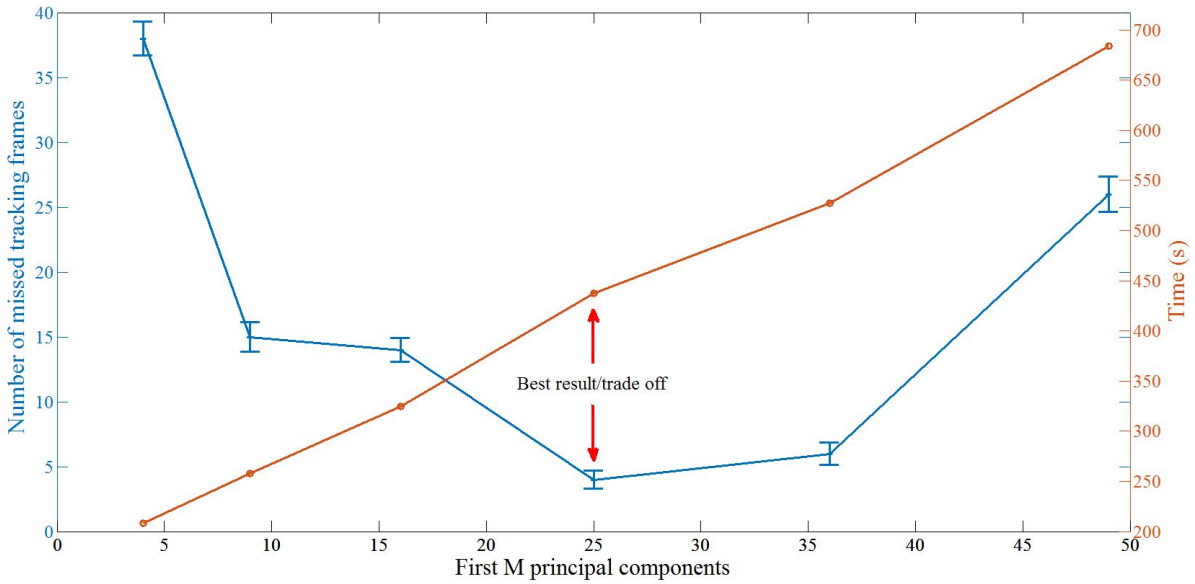

Figure 3.14: *Number of missed tracking frames in a single ultrasound video with its deviation over ten videos (blue line) and the elapsed time when building the K-D trees (red line) with different numbers, M, of PCA components in a single ultrasound video.*

After balancing the number of tracking errors and the elapsed time of building up the K-D trees with compressed data, it has been found that using the first 25 principal components as basis vectors for compressing the 900-element patches is the best (Figure 3.14).

The first 25 principal components are reshaped as 30×30 patches shown in Figure 3.15. Then all the patches in US frames over the video data are compressed into these first 25 principal components.

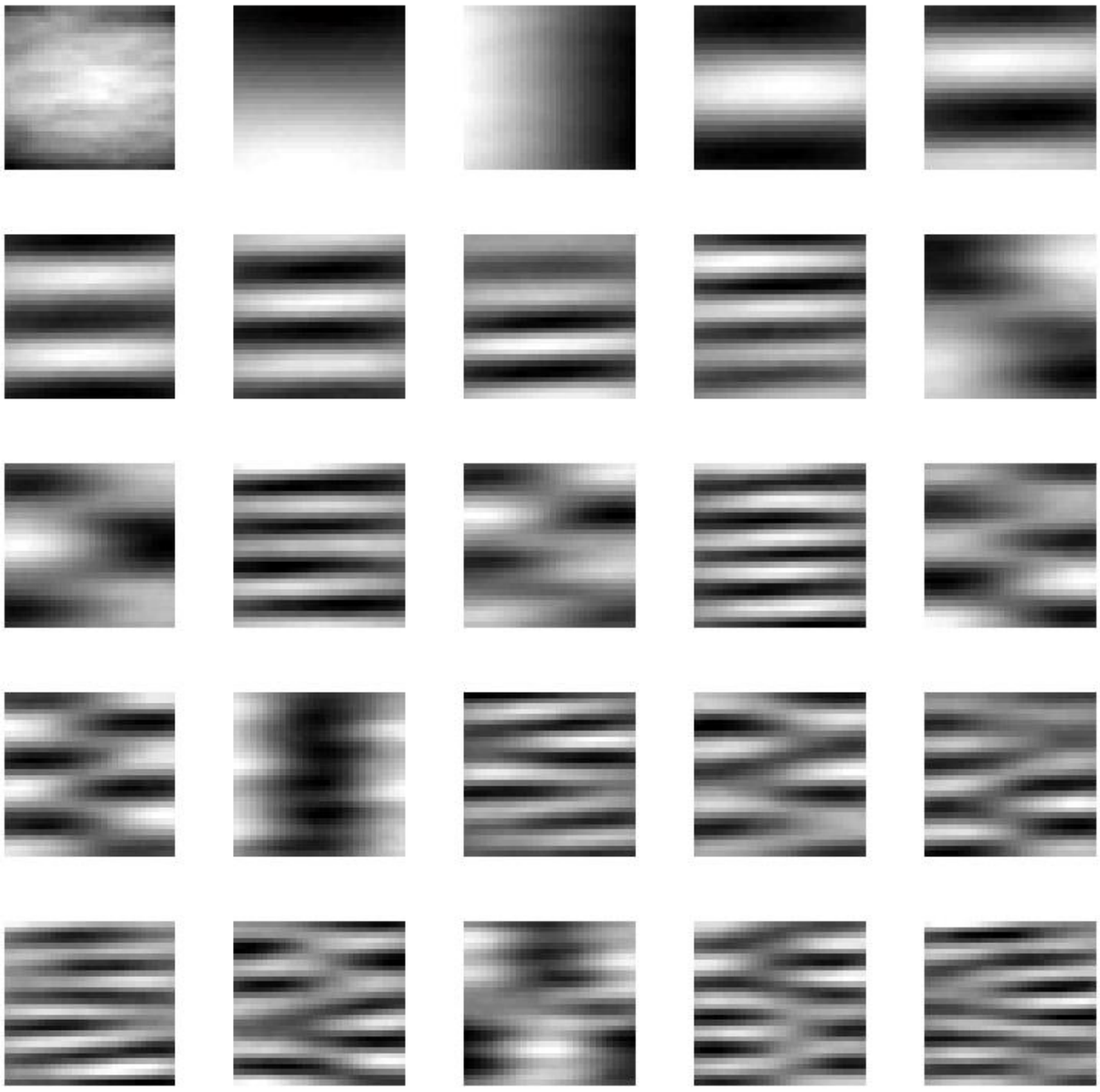

Figure 3.15: *The first 25 principal components for patches projection.*

A comparison of an US image with the compressed image is shown in Figure 3.16. It can be seen that the compressed image presents most information, i.e. boundaries, corners and so on, in the original US image.



(a)

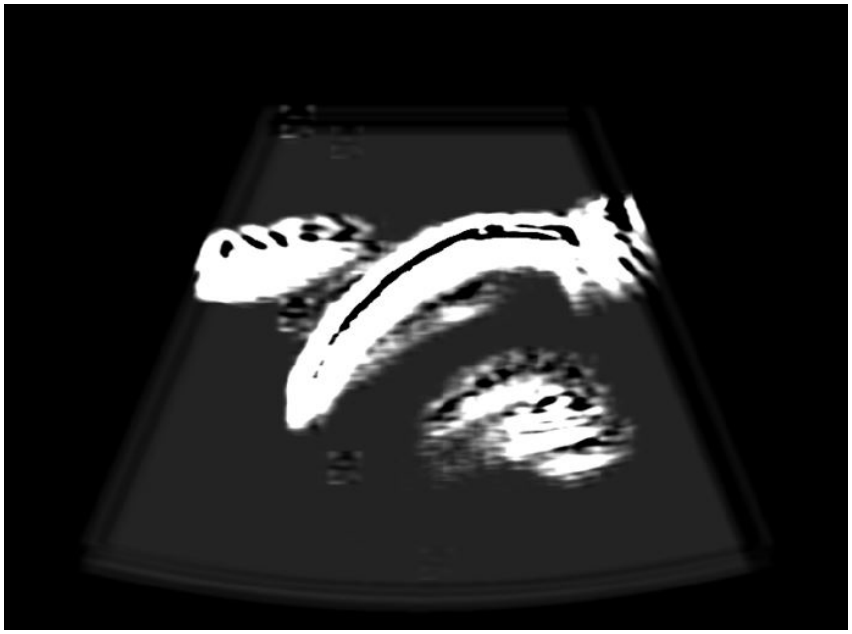

(b)

Figure 3.16: *Comparison between an US image and the its compressed image.*

In each frame, the US image can be described as a $25 \times P$ matrix with the compressed representation of each patch forming one column, where P is denoted as the number of

the patches in one frame with an interval of one pixel between adjacent patches. All patch candidates (i.e. all the columns in the $25 \times P$ matrix) are indexed in order for the next tree search.

• K-dimensional tree searching

In order to search for the target patch in every frame, a tree structure is considered in this subsection. A K-dimensional (K-D) tree is a useful data structure to partition the data for organizing points in a K-D space for the multi-dimensional search [126]. It is a binary tree in which the data are split into half iteratively by hyper-planes [114]. After all the patches are compressed to indexed shorter vectors, a K-D tree is constructed for every frame and the compressed patch vectors are stored in the leaf nodes of the K-D tree. To save computational time, each leaf node in the tree contained 100 patches.

The target patch is searched for in every frame in turn by querying the K-D trees of every frame with the target patch descriptor as input to find the top N matches. In other words, the top N nearest neighbours to the template patch are retained from the search [104]. In this study, the top 30 nearest neighbours are found as there will not be more than 30 similar matches within an US image and, in practice, using the top 30 nearest neighbours does give fairly good results (more than 90% accurate tracking frames of different US videos).

• k-means clustering

Although the top N matches are found in each frame, some of these matches may be very close to each other in space. In order to keep the best responses and remove matches adjacent to any existing matches, a fast k-means clustering algorithm is employed to the image coordinates of the top N matches. The k-means clustering partitions the N matches into k clusters so that the shortlisted patches that are close to one another can be clustered into one group and replaced by a single patch at the mean location [136]. If the top N matches is denoted as $(x_1, x_2, \ldots, x_N)$, the k clusters as $(C_1, C_2, \ldots, C_k)$ and

the mean values of the clusters as $(\mu_1, \mu_2, \ldots, \mu_k)$, the k-means clustering's objective is to find:

$$\arg\min_{S} \sum_{i=1}^{k} \sum_{x \in S_i} \| x - \mu_i \|^2 \tag{3.7}$$

The top N matches are clustered into k clusters in each frame and the k clusters are left to find the best match using dynamic programming optimization, which is sensitive to the number of matches [17]. Empirically, the top six matches are chosen as the clusters as these six matches are the most likely correct tracking patches.

• Dynamic programming optimization

Dynamic programming is efficiently used for optimization. It breaks down one optimization problem into several sub-problems to avoid overlapping calculations [41]. Here, the sub-problems are to find the costs of the possible matches in each frame.

The frame length of an US video is denoted by F. The tracked positions in the video are represented as a set $\mathcal{X} = \{X_f\}_{f=1,2,\ldots,F}$, where X_f is a 2D vector (x_f, y_f), that describes the position of the tracked patch throughout the US video. The set of image intensity description vectors are denoted as $\mathcal{I}_{\mathcal{X}} = \{I_f\}_{f=1,2,\ldots,F}$, where I_f is the compressed intensity vector, i.e. the patch appearance, associated with the location X_f.

To track the top match in every frame, a tracking template T is initialized by the user in frames of the US video by selecting the desired bony landmark (Figure 3.12). Multiple templates can be initialized if multiple patch tracking is required. When there is a tracking error, another template T_i can be picked in the erroneous tracking frame and added to the template patch set $\mathcal{T}$ which may have R tuples. The template set $\mathcal{T} = \{T_i\}_{i \in R} = \{(Y_i, t_i)\}_{i \in R}$ contains the location $Y_i = (x_i, y_i)$ and the compressed intensity descriptor (the patch appearance) t_i of the template.

The error function of the dynamic programming optimization considers the patches' locations and appearances of the clusters, and the appearance difference between the

template set $\mathcal{T}$ and the clusters in every frame, which is calculated as in Equation (3.8).

$$E(\mathcal{X}) = \sum_{f} e(f)$$
$$e(f) = \lambda_d \cdot D(X_f, X_{f-1}) + \lambda_a \cdot A(I_f, I_{f-1}) + \min_i(A(I_f, t_i)) \tag{3.8}$$

where $D(,)$ is the spatial Euclidean distance of the locations between two tracked patches in two consecutive frames f and frame $(f-1)$, $A(,)$ is the appearance difference, i.e. the sum of squared difference of the compressed intensity descriptors between tracked patches in any two successive frames, λ_d and λ_a are the weight coefficients for the distance difference and appearance difference. The λ_d and λ_a can be tuned to find the best tracking result depending on user's US video. Both λ_d and λ_a are tuned from 0.1 to 1.0. 0.9 for λ_d and 0.6 for λ_a are set respectively to give best tracking results over 10 US videos (around 2500 frames) of the femur phantom rotation. An accuracy percentage map for selecting the best parameters is shown in Figure 3.17.

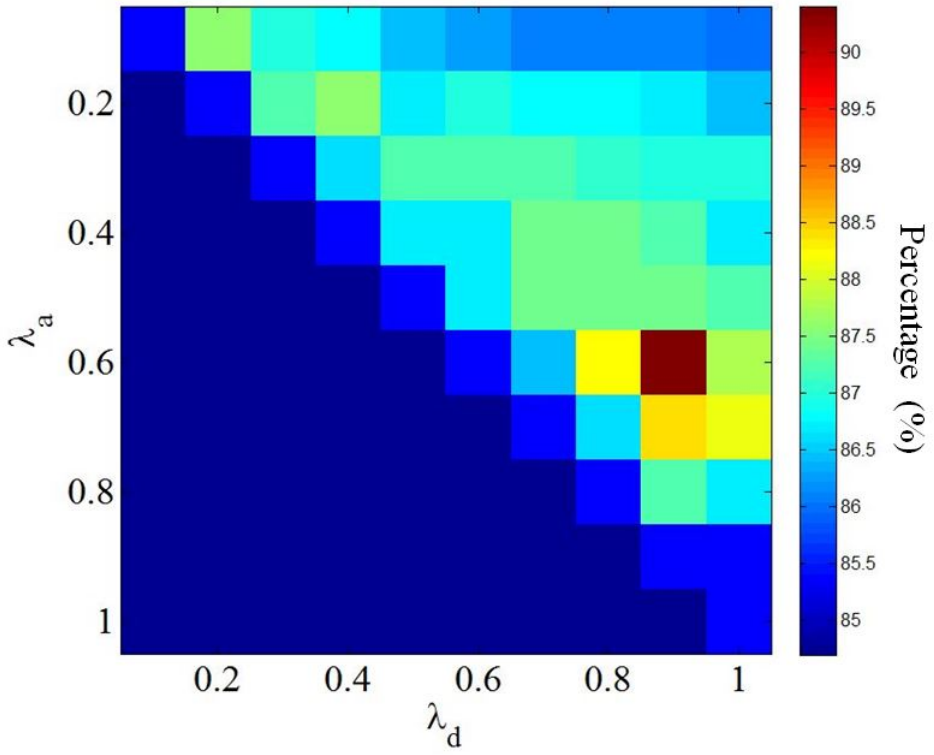

Figure 3.17: *The accuracy percentage map for λ_d and λ_a parameters selection.*

A set of tracked positions $\mathcal{X}$ is chosen to minimize the error function $E(\mathcal{X})$. The error costs for each tracked patch candidates in frame f tracked from the candidate with the smallest error cost in frame $(f-1)$ are calculated, and the corresponding index numbers of the candidates with smallest error cost in frame $(f-1)$ to every candidate in frame f are stored. Lastly, the tracked patch positions are traced back from the last to the first frames with minimal error cost. If a tracking error occurs in frame f, a new template can be selected and t_i in the error function will be changed. The dynamic programming optimization needs to be applied again from frame f to the end. The correct tracking in the previous frames before frame f is retained.

Figure 3.18 illustrates an example of the dynamic programming optimization for the first five frames of a sequence. The boxes represent the top clustered matches found from the K-D trees in each frame throughout the US video. The error cost for every shortlisted patch P_t in frame f related to every patch Q_r in frame $(f-1)$ is calculated. The minimal error cost and the associated index number of patch Q_r in frame $(f-1)$ are stored for each patch P_t. Then, the optimal path (red dot lines) from the last to the first frames is found in Figure 3.18. The table beneath the diagram shows the Euclidean distance error of the tracked patch with respect to the manually picked ground truth from two field experts. Each column of the table is corresponding to each column of the diagram above the table.

Since this research is concerned with only one bony landmark, a single template patch of the greater trochanter is selected. Multiple target patches can be selected for user's particular case.

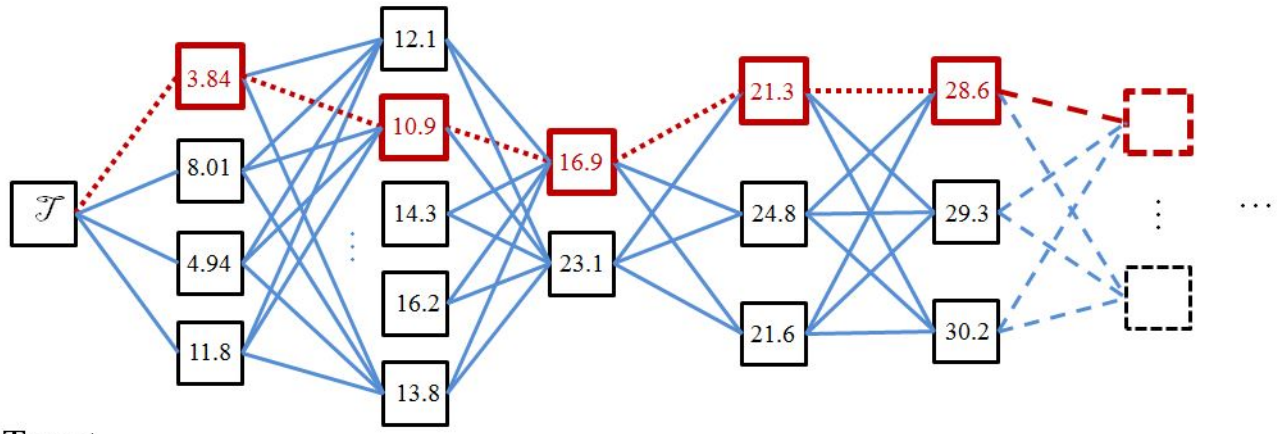

Frame No.	Target patch	f_1	f_2	f_3	f_4	f_5	⋯	f_n
Error (pixel)	0	2.8	2.4	1.3	2.0	1.8	⋯	

Figure 3.18: *Example results from the dynamic programming stage. The diagram illustrates the graph constructed from frames 1 to 5 of example video. The table shows the Euclidean distance error with respect to the ground truth.*

3.3.3 Validation results

• Spatial calibration

The data were collected from five trials of the femur phantom rotation protocol with both MAUS and MA. The positions of the GT marker in the US video were tracked and transformed into the 3D GCS. The GT marker was also reconstructed from the other four femur markers. The spatial error was calculated as the Euclidean distance between the MAUS GT marker and the MA GT marker during the rotation shown in Figure 3.19. The average Euclidean distance error over all five trials was 0.34 mm less than 1 mm which is within the clinical tolerance (±1 mm).

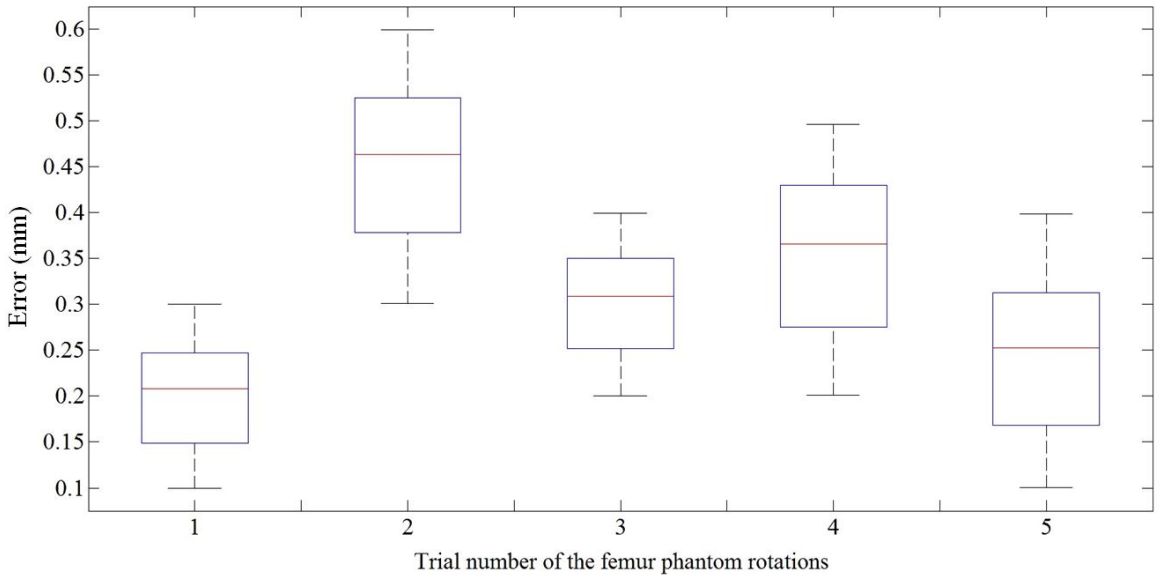

Figure 3.19: *Euclidean distance error between the MA GT marker and the MAUS GT marker over five trials.*

• Temporal calibration

After the temporal calibration, a resampling rate of 0.32 was calculated. Figure 3.20a shows the frame number of the MA and MAUS data before resampling the MA data while Figure 3.20b shows the result after resampling the MA data. The MA frame corresponding to each US frame was found and the Euclidean distance was calculated between the MA GT marker and the MAUS GT marker with an clinically tolerated accuracy of 1 mm presented above.

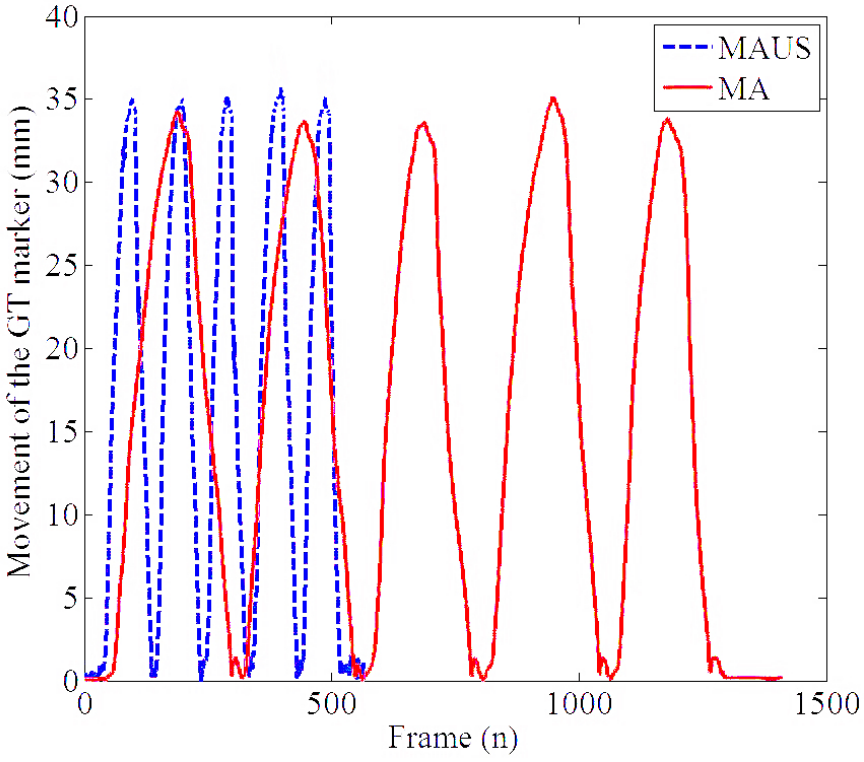

(a)

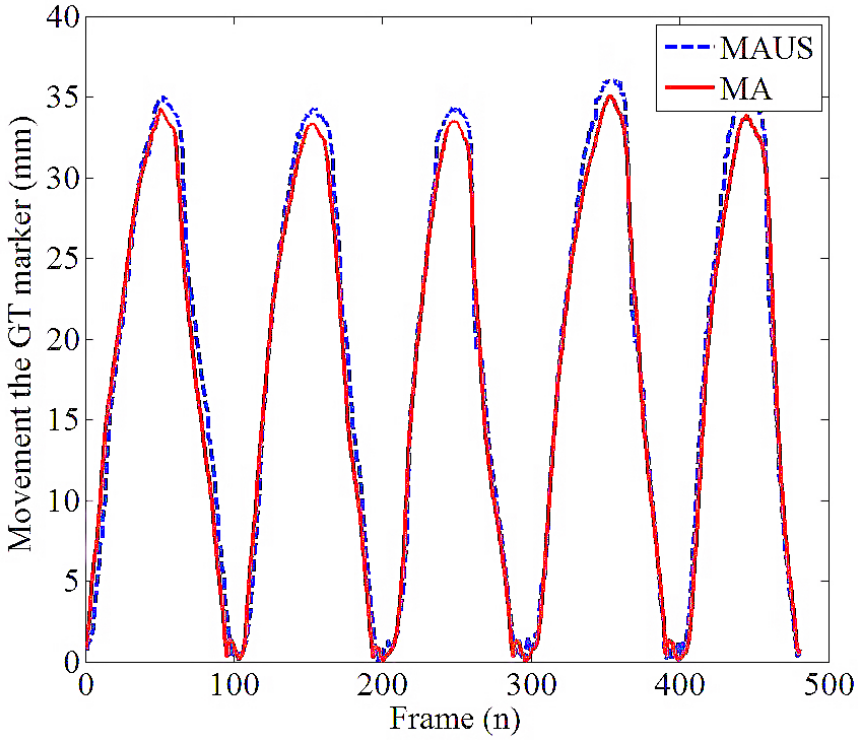

(b)

Figure 3.20: *Results of the temporal calibration, a) before and b) after.*

With the both spatially and temporally validated MAUS system, 2D US slices can be transformed into the 3D GCS and reconstructed as a 3D volume. A detailed description of three dimensional (3D) US volume reconstruction and interpolation using MAUS has been published for 3D visualization in the proceedings of *Medical Image Understanding and Analysis, 2015* [63] and is included in Appendix C.

3.4 Conclusions

This chapter has outlined an augmented MAUS system developed in this research. The new MAUS system transforms full 2D ultrasound information into 3D space instead of locating structure-of-interest by eyeballing with previous Monk's MAUS system. A novel multi-use calibration box has been introduced for image distortion assessment, spatial calibration and temporal calibration. Validation of the calibration procedures has been conducted with a proximal femur phantom. A patch-based tracking algorithm has been developed to assist the validation procedure. Compared to other separate calibration equipment for individual tasks, this multi-use calibration box has shown its efficiency and convenience with both a high spatial accuracy and a high temporal accuracy. The spatially and temporally calibrated MAUS system can then be used to acquire data for computer-aided post-processing in the following chapters (4, 5 and 6).

Chapter 4

Globally Optimal Iterative Closest Point Registration

In this chapter, a globally optimal iterative closest point (ICP) registration algorithm is employed to locate the bone of interest in 3D space. After an augmented motion analysis with ultrasound (MAUS) system was introduced in Chapter 3 that compounds frames from a 2D ultrasound (US) sweep to form a 3D US volume, a computer-aided post-processing pipeline is introduced from this chapter to make the system more accurate and automatic. Since the aim of this research is to describe hip joint kinematics, an important bony landmark of interest, i.e. the greater trochanter (GT), has to be located in 3D space. However, with the previous MAUS system [88], the target bony landmark was located by visual inspection from an US screen; this is less accurate, time consuming and extremely dependent on the operator's experience. To tackle this problem, automatic 3D registration is considered to find the spatial transformation between the GT at two different poses. By referring to the transformation calculated from registration, the target GT point at the reference position can be transformed to the other position accurately. This method combines a globally optimal search scheme with conventional ICP registration to guarantee the truly optimal result without requiring a good initialization. The content of this chapter has been published in *Procedia of Computer Science, 2016* [65].

4.1 Related registration methods

Data registration, also known as data matching, is a fundamental problem in image and geometry analysis. Its aim is to find the optimal solution (i.e. transformation) to best align two or more 2D and/or 3D images from one or more image modalities [96]. Registration of the musculoskeletal structures between different subjects is particularly challenging since it involves a number of interrelated components undergoing large, non-linear deformations with significant anatomical variations in the population [43]. In this research, this issue is avoided as the aim is to calculate the transformation between two data sets of one particular bone structure from one test subject. Since the bone of interest, the greater trochanter (GT), is a rigid geometry, a rigid geometric registration algorithm is considered to find the spatial transformation between GT surfaces at different poses. Registrations between the data from different modalities, for example computed tomography (CT) data and the ultrasound (US) data, of one same anatomy structure has been widely applied on the spine [93] [94], pelvis [16] and femur [137] [138] for diagnostic imaging and image-guided interventions. However, it has been shown that prolonged exposure to X-ray radiation increases the risk of cancer [44]. As this research focuses on the movement of one particular bone structure during daily routine activities and the limited CT bore space cannot provide a big enough space for a full joint motion, it is unnecessary and not ideal to expose the subject to radiation. Thus, instead of the registration between US data and CT data, the registration between reconstructed US bone surfaces at different poses is performed.

The GT surfaces reconstructed from a set of 2D bony structures from US sweeps are represented by a group of 3D points. The iterative closest point (ICP) algorithm proposed by Besl and McKay [12] is one of the most commonly used methods for point cloud registration under Euclidean transformations [144]. Conventional ICP is intuitive. It evolves the minimal sum of the L_2 Euclidean norm between all matched pairs of points in two 2D or 3D point clouds to best align these two data sets. The cost function

optimization of the conventional ICP algorithm however suffers from getting trapped in local minima which may lead to an incorrect registration result. In other words, the optimal registration result from a conventional ICP algorithm may be far away from the true optimal solution [65] as illustrated by the red crosses (incorrect solutions) in Figure 4.1. More critically, there is no reliable way to tell whether or not the algorithm is trapped in a local minimum. From Figure 4.1, it can be seen that conventional ICP can only converge to the global minimum and get the correct result when it starts with a good initialization within the blue dash box. Thus, a well defined initialization is required to start the conventional ICP algorithm to obtain a correct registration result.

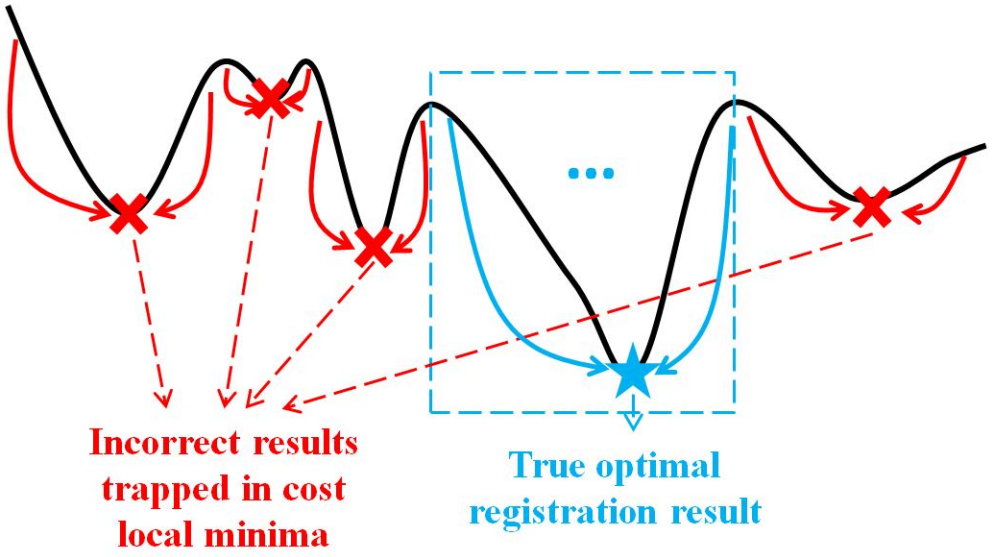

Figure 4.1: *Limitation of the conventional ICP algorithm.*

Moreover, because each of the two point sets may contain a different number of points, there might be a large number of points that are not matched to a corresponding point in the other point set. Thus, if the initialization was not well defined, it may lead to an erroneous registration where the optimization of the registration would be trapped into a local minimum L_2 norm (red crosses in Figure 4.1). The L_2 norm optimization is also sensitive to outliers. A small number of outliers may adversely affect the entire registration. In order to solve these issues, a trimmed ICP has been proposed by Chetverikov *et al.,* to find the best match between two point sets [22]. For conventional ICP, it is

assumed that the data points can be paired in the reference point cloud. In Chetverikov's paper, only a guaranteed rate ξ of the data points can be matched to the reference point cloud. Then the ICP was called multiple times with different values of ξ until the cost got converged. However, it still relies on a good initialization to better align two point clouds by pre-registering these two point sets at the beginning. Fitzgibbon reported a LM-ICP method in which the L_2 norm of ICP was optimized using the Levenberg-Marquardt algorithm [36]. A smoothing kernel was applied to enlarge the convergence basin, which improved the robustness of general ICP. As the conventional ICP is sensitive to the noise and outliers, to tackle this problem, Jian *et al.,* presented a method to register between the Gaussian mixture models of the data sets instead of a direct registration between two point clouds [68]. However, these still end up as a local search.

Yang *et al.,* recently proposed a globally optimal ICP registration algorithm using branch-and-bound (BnB) search for natural images [144]. It guarantees a globally optimal solution without requiring a good initialization. In this chapter, Yang's method is validated with a proximal femur phantom (Section 4.3) and employed to locate the bony structure of interest, i.e. the greater trochanter. From the globally optimal registration result, it enables the quantification of hip joint kinematics described in Chapter 6. The 3D surfaces for registration can be obtained from the manual segmentation of the bony structure in either each frame of the 2D US videos or each slice of the 3D reconstructed US volumes (Appendix C).

4.2 Globally optimal iterative closest point algorithm

As the globally optimal ICP registration algorithm is to introduce a global search scheme to conventional ICP registration, a brief recap of the conventional ICP is presented in Section 4.2.1 followed by a branch-and-bound (BnB) globally optimal search scheme in Section 4.2.2.

4.2.1 Iterative closest point registration

Iterative closest point (ICP) registration addresses the Euclidean alignment of two 3D point clouds [22]. It minimizes the sum of the L_2 norm between all matched pairs of points in two point clouds.

In ICP, the reference point cloud, which another point cloud registers to, is commonly defined as the model ($\boldsymbol{M}$) while the other point cloud is defined as the data ($\boldsymbol{D}$). In this research, the GT surface reconstructed while the test subject is at an upright standing pose is chosen to be the model and the GT surfaces captured while the testing subject is at other typical gait poses, i.e. heel strike, mid stance, toe off and mid swing, are treated as the data.

The model and data are denoted by $\boldsymbol{M} = \{m_i\}, i = 1, \cdots, M$ and $\boldsymbol{D} = \{d_j\}, j = 1, \cdots, D$, where m_i and d_j are point coordinates of point i in the model and point j in the data respectively in 3D space $\mathbb{R}^3$. The goal of ICP is to minimize the L_2 norm E between the closest corresponding points in model and data (Equation 4.1) by estimating a rigid body rotation $\mathbf{R}$ in special orthogonal rotation group $\mathbf{SO}(3)$ and translation $\mathbf{t} \in \mathbb{R}^3$ [13].

$$E(\mathbf{R}, \mathbf{t}) = \sum_{j=1}^{D} e_j(\mathbf{R}, \mathbf{t})^2 = \sum_{j=1}^{D} \parallel \mathbf{R}d_j + \mathbf{t} - m_{i*} \parallel^2 \tag{4.1}$$

where e_j is the Euclidean distance between the transformed point d_j in the data point cloud and the closest corresponding point m_{i*} in the model point cloud. The optimal

corresponding point m_{i*} of d_j is found by Equation 4.2.

$$i* = \underset{i\in(1,\cdots,M)}{\operatorname{argmin}} \parallel \mathbf{R}d_j + \mathbf{t} - m_{i*} \parallel^2 \tag{4.2}$$

If the point correspondences between the points in data and model are known, the rotation $\mathbf{R}$ and the translation $\mathbf{t}$ can be calculated using least-squares fitting [7]. alternatively, if the transformation is given, it is trivial to obtain the optimal set of correspondences between model and data. However, neither the best correspondence nor the optimal transformation are known which makes this problem non-trivial to solve. For the conventional ICP algorithm, the rotation $\mathbf{R}$ and the translation $\mathbf{t}$ are initialized and adapted iteratively until the error defined by Equation 4.1 converges. Because of the nature of the iteration, the conventional ICP algorithm may get trapped in a local minimum of the cost function [144]. Thus, well-initialized $\mathbf{R}$ and $\mathbf{t}$ parameters are essential for a correct ICP registration result.

4.2.2 Branch-and-bound global optimization

Branch-and-bound (BnB) is a computationally efficient approach for performing global searches that has been used for non-convex optimization problems [75]. To tackle the local minima traps in conventional ICP, a combination of conventional ICP and BnB search [144] is applied iteratively to guarantee a globally optimal solution with no requirement for a good initialization or pre-registration. The global search is started with a randomly initialized ICP result. The BnB method is then applied to find whether there is a better solution with a lower L_2 norm than the current ICP result in the 3D space. Whenever a better solution is found, another ICP process is launched with the initialization at this solution. Finally, the upper bound of BnB search is updated by the ICP result until its convergence. Although ICP registration and BnB search are well-known algorithms, it is non-trivial to parameterize the 3D space to the 3D special Euclidean group, $\mathbf{SE}(3)$, and define the bounds of each branch for BnB search.

3D global space parametrization

To minimize the error in Equation 4.1, all movements in 3D space can be covered within the $\mathbf{SE}(3)$ group. All the members in $\mathbf{SE}(3)$ can be parameterized with a minimum of six parameters: three rotation parameters and three translation parameters, i.e. $\mathbf{SE}(3) = \mathbf{SO}(3) \times \mathbb{R}^3$. For the rotation, each rotation is presented as a vector $\mathbf{r}$ using an angle-axis representation [52]. The direction of vector $\mathbf{r}$ indicates the rotation axis and the norm of $\mathbf{r}$ is the rotation angle. $\mathbf{R_r} \in \mathbf{SO}(3)$ is used to denote the 3×3 rotation matrix to achieve rotation $\mathbf{r}$. It is formulated by the Rodrigues' rotation formula as in Equation 4.3 [52].

$$\mathbf{R_r} = \exp\left([\mathbf{r}]_\times\right) = \mathbf{I} + \frac{[\mathbf{r}]_\times \sin\|\mathbf{r}\|}{\|\mathbf{r}\|} + \frac{[\mathbf{r}]_\times^2 (1 - \cos\|\mathbf{r}\|)}{\|\mathbf{r}\|^2} \tag{4.3}$$

where $\exp(\cdot)$ is the matrix exponential map and $[\cdot]_\times$ is a skew-symmetric matrix composed of three decomposed rotation angles (r^1, r^2, r^3) as in Equation 4.4 .

$$[\mathbf{r}]_\times = \begin{bmatrix} 0 & -r^3 & r^2 \\ r^3 & 0 & -r^1 \\ -r^2 & r^1 & 0 \end{bmatrix} \tag{4.4}$$

The entire 3D rotation space can now be compactly represented as a sphere with a radius of π using the angle-axis representation. This rotation sphere is enclosed in the minimum cube $[-\pi, \pi]^3$ for easy use. For the translation, a bounded cube $[-\xi, \xi]^3$ with a side length of 2ξ is assumed to be big enough to include the optimal translation.

The rotation and translation cubes are subdivided into smaller sub-cubes denoted as C_r and C_t respectively for BnB search using an Octree structure.

Upper and lower bounds definition

For the BnB search, the bounds of the L_2 norm within a space $C_r \times C_t$ have to be derived for every branch the algorithm explores. Here, the concept of uncertainty radii is introduced for the preparation of calculating the bounds. A mathematical explanation on uncertainty radii is presented below in preparation for defining the bounds.

The uncertainty radius is the radius of a ball that can enclose all possible locations of a 3D data point d after any transformation with which the rotation $\mathbf{r}$ lies within C_r and the translation $\mathbf{t}$ lies within C_t. Given a 3D data point d and two rotations $\mathbf{R_r}$ and $\mathbf{R_{r_0}}$ around axes $\mathbf{r}$ and $\mathbf{r_0}$, the maximum angle between $\mathbf{R_r}d$ and $\mathbf{R_{r_0}}d$ can be obtained from Equation 4.5 which is a lemma in paper [144].

$$\angle(\mathbf{R_r}d, \mathbf{R_{r_0}}d) \leqslant \angle(\mathbf{R_r}, \mathbf{R_{r_0}}) \leqslant \| \mathbf{r} - \mathbf{r_0} \| \tag{4.5}$$

where $\angle(\mathbf{R_r}, \mathbf{R_{r_0}}) = \arccos(\frac{(\mathrm{trace}(\mathbf{R_r^T R_{r_0}})-1)}{2})$ is the angular distance between these two rotations [52]. Based on the lemma above, for any rotation $\mathbf{r} \in C_r$, the rotation uncertainty radius can be calculated using Equation 4.6. An illustration on the derivation of the rotation uncertainty radius is shown in Figure 4.2.

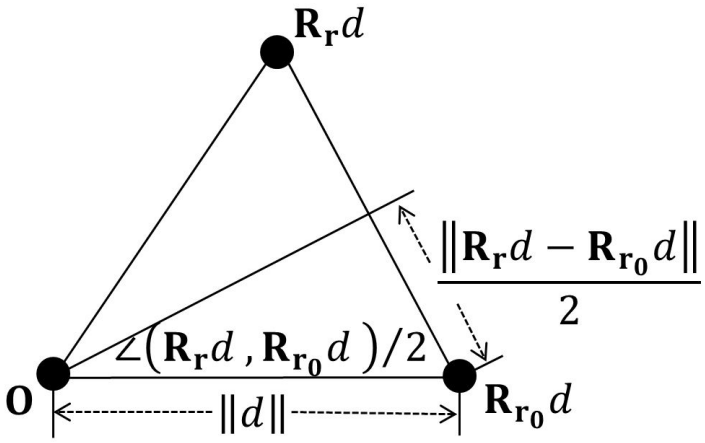

Figure 4.2: *Derivation of the rotation uncertainty radius.*

$$
\begin{aligned}
\|\mathbf{R_r}d - \mathbf{R_{r_0}}d\| &= 2\sin\left(\angle(\mathbf{R_r}d, \mathbf{R_{r_0}}d)/2\right)\|d\| \\
&\leqslant 2\sin\left(\min\left(\angle(\mathbf{R_r}d, \mathbf{R_{r_0}}d)/2, \pi/2\right)\right)\|d\| \\
&\leqslant 2\sin\left(\min\left(\angle(\|\mathbf{r} - \mathbf{r_0}\|)/2, \pi/2\right)\right)\|d\| \\
&\leqslant 2\sin\left(\min\left(\frac{\sqrt{3}\sigma_r}{2}, \frac{\pi}{2}\right)\right)\|d\| = \gamma_r
\end{aligned}
\tag{4.6}
$$

where $\mathbf{R_{r_0}}$ is the rotation matrix of rotation $\mathbf{r_0}$ within the rotation cube C_r with a side length of $2\sigma_r$ with $\mathbf{R_{r_0}}d$ as the centre. The rotation uncertainty radius γ_r is the maximum distance between $\mathbf{R_r}d$ and $\mathbf{R_{r_0}}d$, shown in Figure 4.3. As the γ_r is point-dependent, γ_{r_j} is denoted as the rotation uncertainty radius at point d_j. In Figure 4.3, the yellow ball

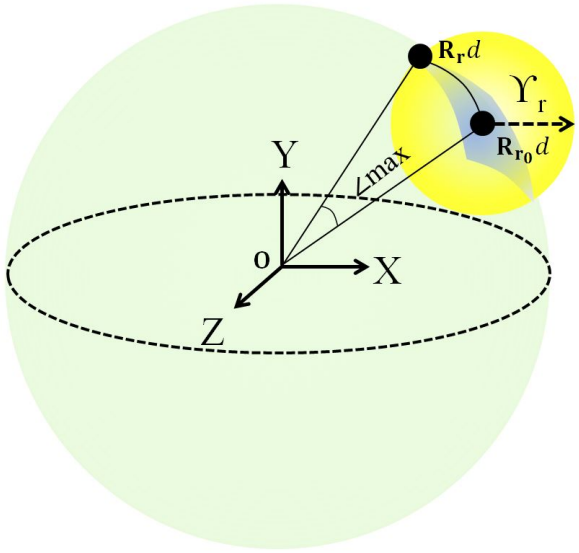

Figure 4.3: *Rotation uncertainty radius.*

is defined as the rotation uncertainty ball in which obviously the rotation uncertainty radius is the radius of this yellow ball. As 3D rotations belonging to the $\mathbf{SO}(3)$ group are enclosed in the light green ball, the blue surface is defined as the rotation uncertainty area of a given 3D point d from $\boldsymbol{D}$ perturbed by an arbitrary rotation $\mathbf{r}$ centred $\mathbf{r_0}$.

Similarly, for any translation $\mathbf{t} \in C_t$, the translation uncertainty radius is defined as the maximum distance between point $(d - \mathbf{t})$ and point $(d - \mathbf{t_0})$. It is the radius of a minimum translation ball, also defined as the translation uncertainty ball, that can

enclose the translation cube C_t with a side length of $2\sigma_t$. In this research, maximum σ_t, which is the largest translation distance between two data sets, is set to 1 to meet the clinical tolerance ($\pm 1mm$). γ_t is denoted as the translation uncertainty radius which can be calculated using Equation 4.7 and is shown in Figure 4.4.

$$\begin{aligned} \| (d - \mathbf{t}) - (d - \mathbf{t_0}) \| &= \| \mathbf{t} - \mathbf{t_0} \| \\ &\leqslant \sqrt{3}\sigma_t = \gamma_t \end{aligned} \tag{4.7}$$

where $\mathbf{t_0}$ is initial translation. The translated 3D data point $d + \mathbf{t_0}$ is represented as the centre of the translation uncertainty ball, i.e. the centre of the translation cube C_t. In Figure 4.4, the yellow ball is the translation uncertainty ball and the blue cube is

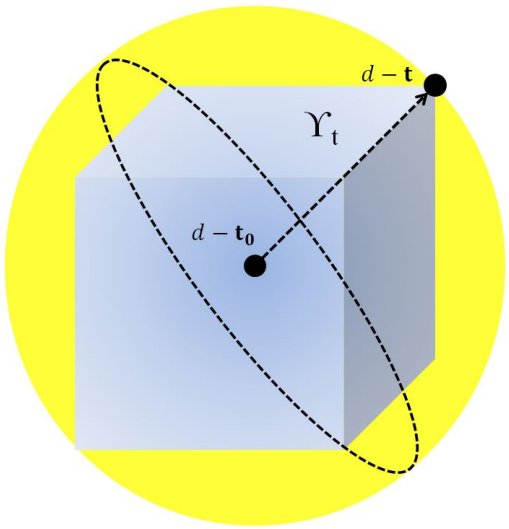

Figure 4.4: *Translation uncertainty radius.*

the rotation uncertainty area of a given 3D point d from $\mathbf{D}$ perturbed by an arbitrary translation $\mathbf{t}$ centred $\mathbf{t_0}$.

After the uncertainty radii of the rotation and translation have been defined separately, the upper and lower bounds of the L_2 norm $e_j(\mathbf{R}, \mathbf{t})$ can be derived for a given point d_j. It is trivial to to define the upper bound $\overline{e_j}$ with any rotation and translation $(\mathbf{R}, \mathbf{t}) \in C_r \times C_t$. Because of the nature of ICP, the L_2 norm of a given point with the specific rotation and translation $(\mathbf{R}, \mathbf{t})$ must be no smaller than the smallest L_2 norm

within the uncertainty space $(C_r \times C_t)$ as Equation 4.8.

$$e_j(\mathbf{R_{r_0}}, \mathbf{t_0}) \geqslant \min_{\forall(\mathbf{r},\mathbf{t})\in(C_r\times C_t)} e_j(\mathbf{R_r}, \mathbf{t}) \tag{4.8}$$

Thus, the upper bound $\overline{e_j}$ can be defined as:

$$\overline{e_j} = e_j(\mathbf{R_{r_0}}, \mathbf{t_0}) \tag{4.9}$$

It is straightforward to define the upper bound $\overline{e_j}$. However, it is non-trivial to define the lower bound $\underline{e_j}$ of point d_j with any rotation and translation $(\mathbf{R}, \mathbf{t}) \in C_r \times C_t$. In order to find the minimal L_2 norm within the uncertainty space, the rotation and translation together have to be taken into consideration. The uncertainty space is a ball centred at $\mathbf{R_0}d_j + \mathbf{t_0}$, where $\mathbf{t_0} = 0$, with the uncertainty radius $\gamma_{r_i} + \gamma_t$ as in Figure 4.5.

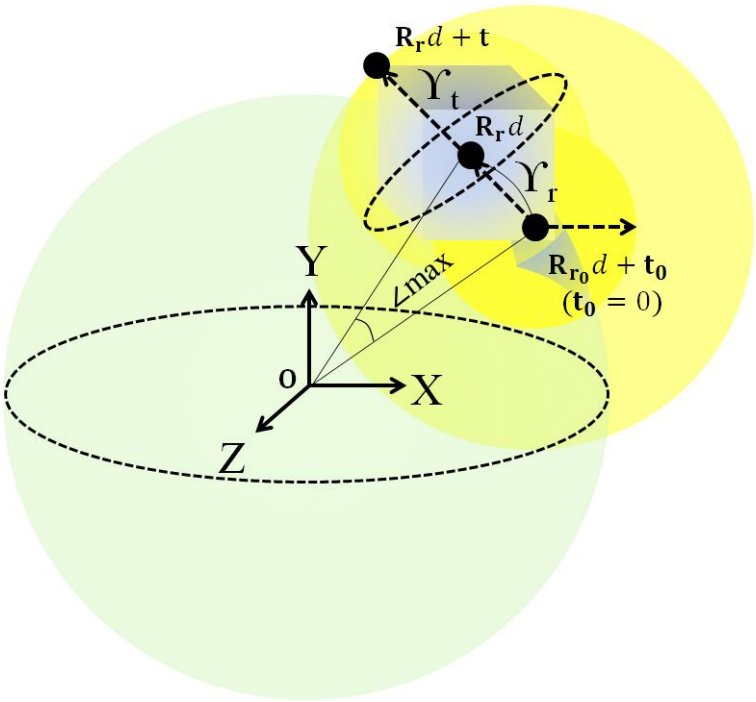

Figure 4.5: *Uncertainty radius.*

As the definition of L_2 norm e_j of point d_j in Equation 4.1 is the distance between the transformed point $(\mathbf{R_r}d_j + \mathbf{t})$ and point $m_{i*} \in \boldsymbol{M}$ which is its closest corresponding

point, for any $(\mathbf{r}, \mathbf{t}) \in (C_r \times C_t)$, the lower bound $\underline{e_j}$ can be calculated as:

$$\underline{e_j} = \max\left(e_j(\mathbf{R_{r_0}}, \mathbf{t_0}) - (\gamma_{r_j} + \gamma_t), 0\right) \tag{4.10}$$

which has been proved in [144]. For all the transformations within the $C_r \times C_t$ uncertainty region, the closest distances to the 3D model point cloud $\boldsymbol{M}$ are no less than $\underline{e_j}$ as shown in Figure 4.6

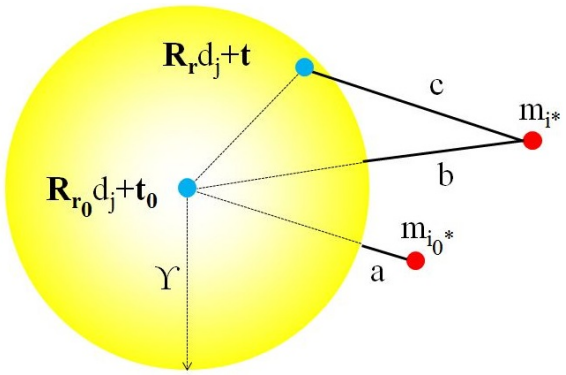

Figure 4.6: *Lower Bound illustration.*

The upper ($\overline{E}$) and lower ($\underline{E}$) L_2 norm bounds for an uncertainty space $C_r \times C_t$ centred at ($\mathbf{r_0}$, $\mathbf{t_0}$) can be calculated by Equations 4.11 and 4.12.

$$\overline{E} = \sum_{j=1}^{D} \overline{e_j}^2 = \sum_{j=1}^{D} e_j(\mathbf{R_{r_0}}, \mathbf{t_0})^2 \tag{4.11}$$

$$\underline{E} = \sum_{j=1}^{D} \underline{e_j}^2 = \sum_{j=1}^{D} \max\left(e_i(\mathbf{R_{r_0}}, \mathbf{t_0}) - (\gamma_{r_j} + \gamma_t), 0\right)^2 \tag{4.12}$$

The full 3D motion space is then divided into sub-cubes, i.e. uncertainty spaces, as a tree structure. Both the upper and lower bounds for a given uncertainty space $C_r \times C_t$ are stored in one tree node for BnB search. However, as explained in the space parametrization, motion in 3D space is parameterized with 6 parameters, 3 for the rotation and another 3 for the translation. This means that one parent space will be divided into $2^6 = 64$ child spaces, which is computationally expensive and memory consuming. In order to find the optimal solution efficiently, a nested BnB search framework is intro-

duced as a two layer BnB search. The rotation space including all rotation $\mathbf{r} \in \mathbf{SO}(3)$ is searched by an outer BnB search, while an inner BnB search is applied to find the corresponding optimal translation in the translation space. The rotation space and the translation space are split into two Octree structures respectively for the BnB search. While calling the outer BnB search for rotation cube C_r, a initialized translation cube ϱ_t is used to calculate the upper bound and lower bound as:

$$\overline{E_r} = \min_{\forall \mathrm{t} \in \varrho_t} \sum_j e_j(\mathbf{R_{r_0}}, \mathbf{t})^2 \tag{4.13}$$

$$\underline{E_r} = \min_{\forall \mathrm{t} \in \varrho_t} \sum_j \max\left(e_j(\mathbf{R_{r_0}}, \mathbf{t}) - (\gamma_{r_j} + \gamma_t), 0\right)^2 \tag{4.14}$$

To derive the rotation lower bound $\underline{E_r}$ with an inner BnB searched translation, the upper and lower bounds for a translation uncertainty space C_t is defined as:

$$\overline{E_t} = \sum_j \max\left(e_j(\mathbf{R_{r_0}}, \mathbf{t_0}) - \gamma_{r_j}, 0\right)^2 \tag{4.15}$$

$$\underline{E_t} = \sum_j \max\left(e_j(\mathbf{R_{r_0}}, \mathbf{t_0}) - (\gamma_{r_j} + \gamma_t), 0\right)^2 \tag{4.16}$$

Thus, the $\overline{E_r}$ can be found by setting zero values to all the rotation uncertainty radii γ_{r_j} in $\overline{E_t}$ and $\underline{E_t}$.

The globally optimal ICP procedure starts with a random initialization in order to prove how the algorithm is independent of an initialization. To speed up the search, the initial ${E_t}^*$ is set to be E^* as the search is useless when the error ${E_t}^*$ from the inner BnB search is greater or equal to the smallest $E*$ from the BnB search so far. Then, a best-first-search strategy is applied to both inner and outer BnB searches to determine whether there is an uncertainty space with a upper bound $\overline{E_r}$ of the L_2 norm smaller than the current smallest error $E*$. If there is, another ICP is performed with the initialization of $(\mathbf{R_0}, \mathbf{t_0})$ of this new uncertainty space to refine the cost function. The ICP registration and BnB search are iteratively integrated to reach to a global minimum

as in Figure 4.7. Whenever the difference between the current smallest error E^* and the lowest bound $\underline{E}$ of the current uncertainty cube is less than the threshold ϵ, the globally optimal ICP algorithm stops. The globally optimal ICP registration algorithm

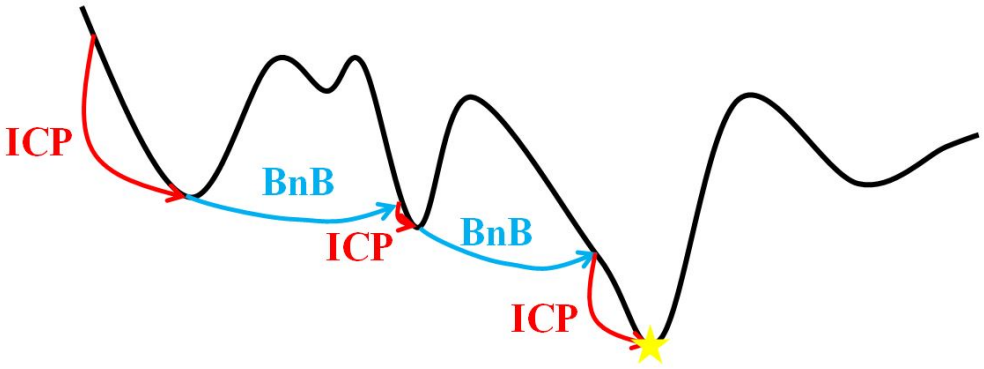

Figure 4.7: *BnB global searched ICP.*

was implemented in MATLAB (*MathWorks, R2014a, US*). The BnB search was an open source implementation from [144] written as a executable C file which can be called back from Matlab.

The 3D reconstructed surfaces were from the proximal femur phantom test in Section 4.3 and from human volunteers in Chapter 6. A detailed description of data acquisition will be presented in Section 4.3 and Chapter 6. All the collected data were processed in MATLAB (*MathWorks, R2014a, US*) on a desktop computer (*8-core Intel Core i7-4770 3.40 GHz running a 64-bit Windows OS*).

4.3 *In-vitro* validation

To validate the globally optimal ICP algorithm, data was acquired on a proximal femur phantom [121] with a spheroidal (ball in socket) joint. The spheroidal joint was fixed in the femur head to mimic the hip spheroidal joint as in Figure 4.8 so that the femur phantom could be rotated in three degrees of freedom (3DOF). Four non-coplanar retro-reflective markers were attached on the proximal femur phantom to provide femur location information as ground truth.

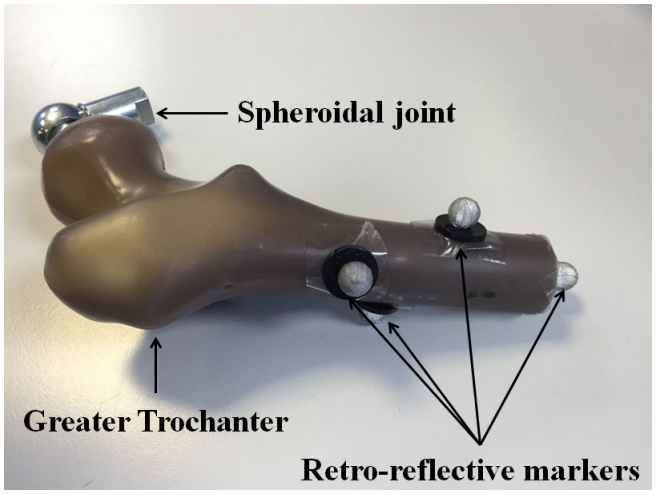

Figure 4.8: *The proximal femur phantom with a ball joint at the femur head*

The femur phantom was then clamped in a water tank which had four retro-reflective markers attached at each corner to give position information of the water tank. Errors caused by small movements of the water tank during the experiment were eliminated by consideration of the tank's position in space throughout the duration. The water tank has a plastic membrane (*Mylar sheet*) window in the front surface through which the ultrasound wave can pass to scan the femur phantom, shown in Figure 4.9. Degassed

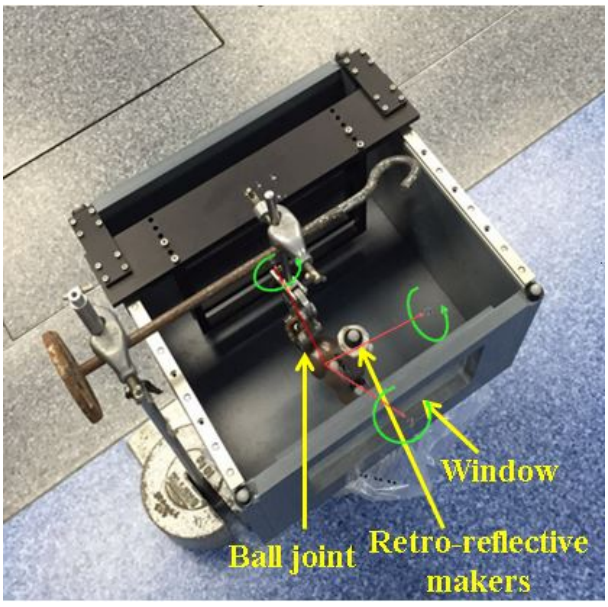

Figure 4.9: *Proximal femur model clapped in a water tank.*

water was added to the water tank and the greater trochanter (GT), which was the

target bony structure, was entirely submerged in the degassed water. Retro-reflective markers for tracking the position of the femur phantom were kept above the water level as retro-reflective markers submerged in the water cannot be captured by the motion analysis system. The femur model was rotated and fixed at five different positions with one approximately vertical reference position.

The *in-vitro* experiment was conducted in the Oxford Gait Laboratory where there are 16 infra-red cameras (*Cara, Vicon, Oxford, UK*) to capture retro-reflective markers with a sampling frequency of 100 Hz in the 3D global space. An ultrasound (US) device (*LOGIQ S7, GE, USA*) was used to scan the target object at 23 Hz (45 mm US depth). Four markers were attached to a bespoke thermoplastic probe cover for a ML 6-15 US transducer as a local coordinate reference of the US probe, shown in Figure 4.10.

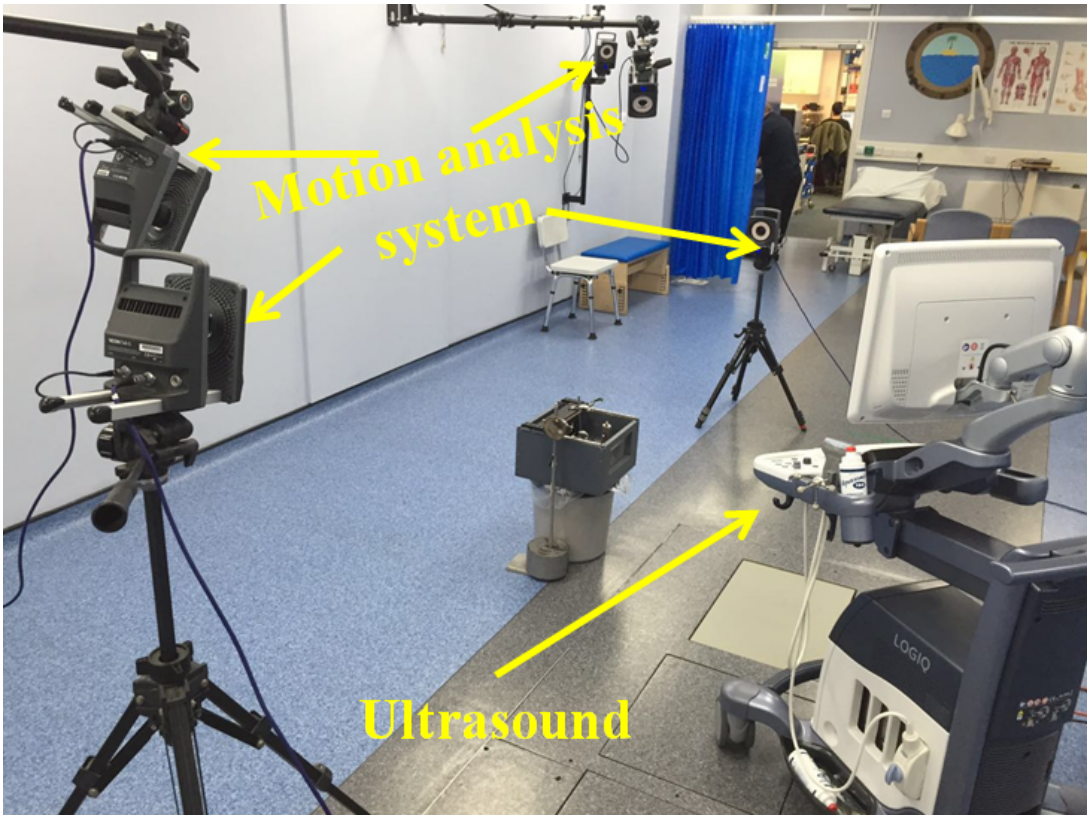

Figure 4.10: *In-vitro experiment setup.*

The femur phantom was then rotated into five positions. An US scan of a target bony structure (i.e. the greater trochanter (GT)) was constrained in a parallel sweep, i.e. the US probe is moved such that consecutive US images are parallel, at each of those five positions as in Figure 4.11. The GT was scanned three times at each position to test the repeatability of the algorithm. Meanwhile, the positions of all the markers attached

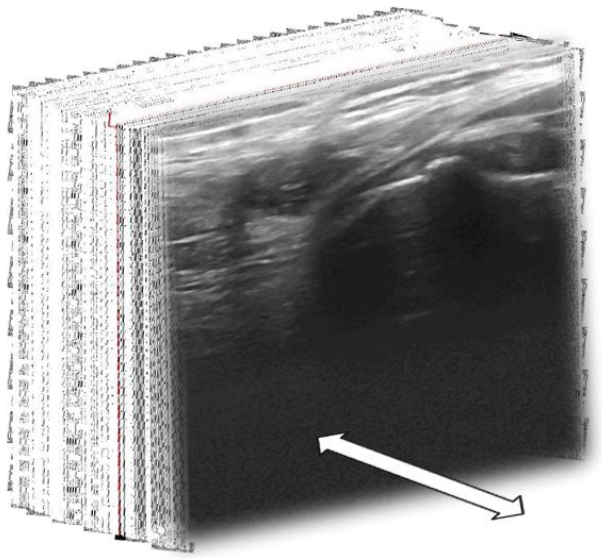

Figure 4.11: *Ultrasound parallel scanning.*

on the box, the femur phantom and the US probe were captured by the motion analysis system at each of those positions during US scanning as in Figure 4.12.

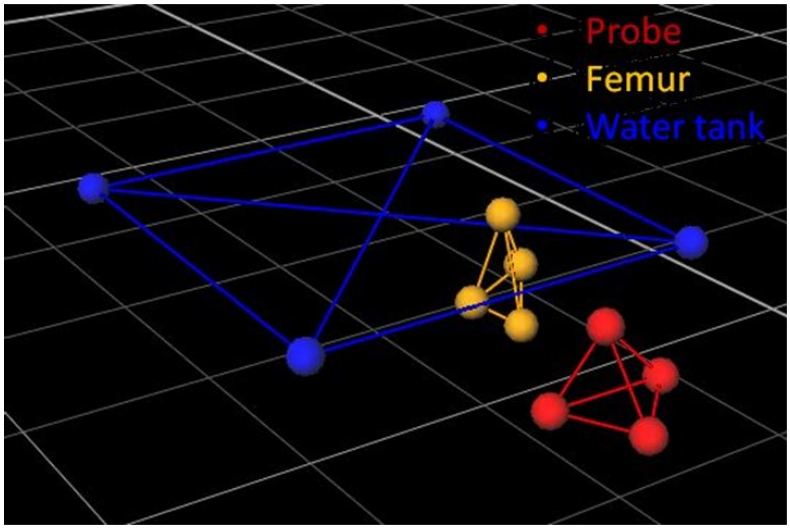

Figure 4.12: *All markers used in the registration validation captured by motion analysis system.*

The bone structures in US slices were manually segmented by two clinicians. The inter- and intra-observer errors were calculated. The average intra-observer error over three segmentations on the same US image was 1.2 pixels and the inter-observer error over two clinicians was 1.4 pixels. The error of the manual segmentation was calculated by average Euclidean distance between the segmentation results on one same US image. Based on the transformation matrix calculated from spatial calibration, those 2D segmented bone structures were transformed into 3D space to reconstruct a 3D bone surface, i.e. greater trochanter (GT), as in Figure 4.13. The GT surface reconstructed

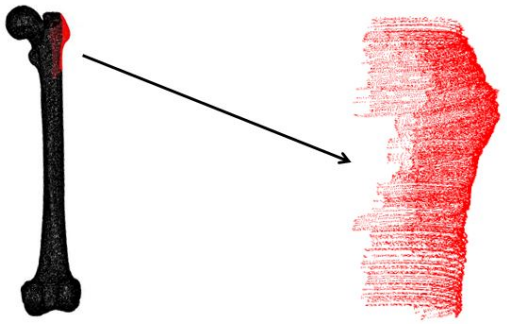

Figure 4.13: *Reconstructed greater trochanter surface of the proximal femur phantom.*

at the first pose was regarded as the reference surface and surfaces reconstructed at the other four positions were regarded as the data to be registered to the reference. In order to save computational time, N ($N = 1000$) points were randomly resampled from both model and data point clouds as registration data sets. All resampled points were normalized into the space of $[-1, 1]^3$. The rotation space and the translation space were set to be $[-\pi, \pi]^3$ and $[-1, 1]^3$ respectively which were large enough to enclose the optimal solution. The minimal rotation uncertainty radius was set to $1.5 \times 10^{-5} (\approx 1^\circ)$ and the minimal translation uncertainty radius was set to 0.01. The denormalized convergence threshold was set to $\frac{1}{N}$ which was 0.001 in this research to satisfy the clinical tolerance of computer-aided orthopaedics surgery ($\pm 1\ mm$) [21]. In the experiments, two point clouds at different positions were pre-registered with a random initialization. The globally optimal registration results were then compared to the ground truth obtained from the four non-coplanar markers captured by the motion analysis system.

4.4 Results

In the femur phantom validation, conventional ICP failed at many angular initializations while globally optimal ICP registration performed well at any angular initialization because of the global search. One example is shown in Fig.4.14.

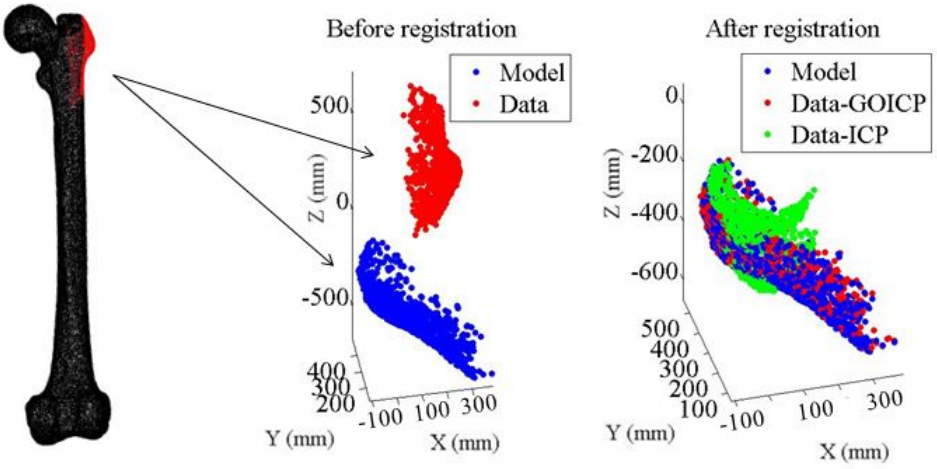

Figure 4.14: *Results comparison between globally optimal ICP registration and conventional ICP registration.*

Compared to the ground truth obtained from the four retro-reflective markers on the femur phantom, the average rotation errors of the globally optimal ICP over three scans of the proximal femur phantom at each positions were 0.52°, 0.55° and 0.071° with standard deviations of 0.90°, 1.15° and 1.13° about the X, Y and Z axes (Figure 4.15a) respectively, while the average rotation errors of the conventional ICP over three scans of the proximal femur phantom at each positions were −24.71°, −56.54° and −1.75° with standard deviations of 103.24°, 79.56° and 11.03° about the X, Y and Z axes (Figure 4.15b) respectively. After denormalizing registered data into the original millimetre scale, the average translation errors of the globally optimal ICP were 0.37 mm, 0.12 mm and 0.46 mm with standard deviations of 0.37 mm, 0.41 mm and 0.38 mm along the X, Y and Z axes in Figure 4.16a respectively, while the average translation errors of the conventional ICP were 1.03 mm, 0.03 mm and 0.38 mm with standard deviations of 2.87 mm, 2.34 mm and 2.30 mm along the X, Y and Z axes in Figure 4.16b.

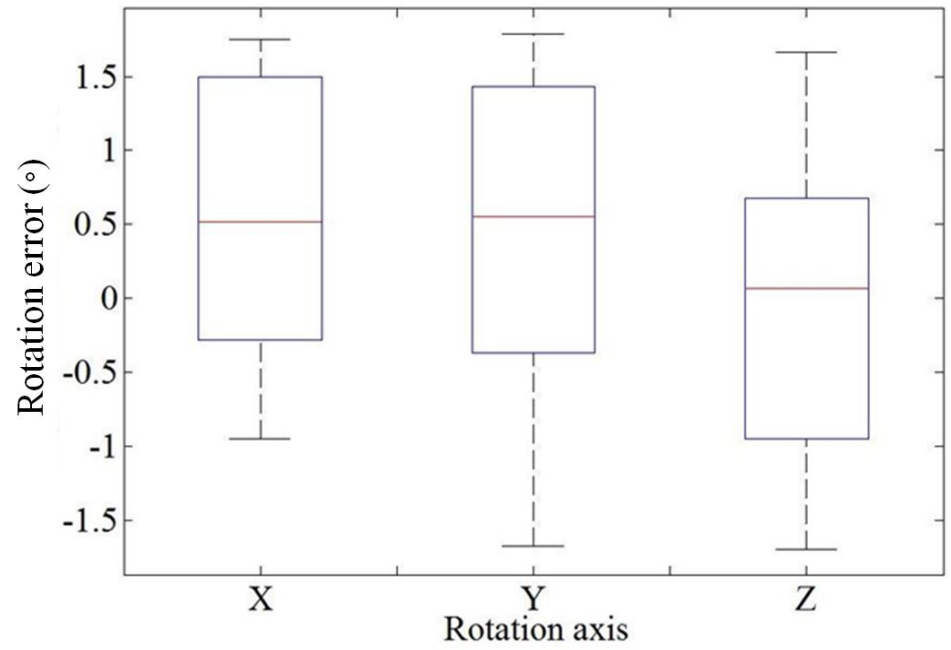

(a)

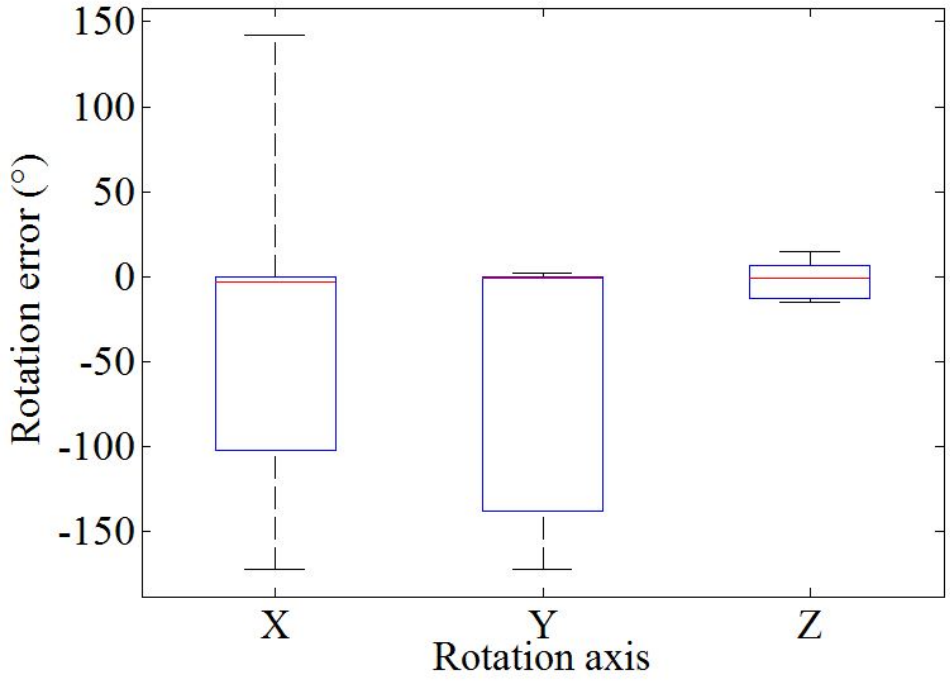

(b)

Figure 4.15: *Rotation errors around three axes compared to the ground truth of a) the globally optimal ICP registration and b) the conventional ICP registration.*

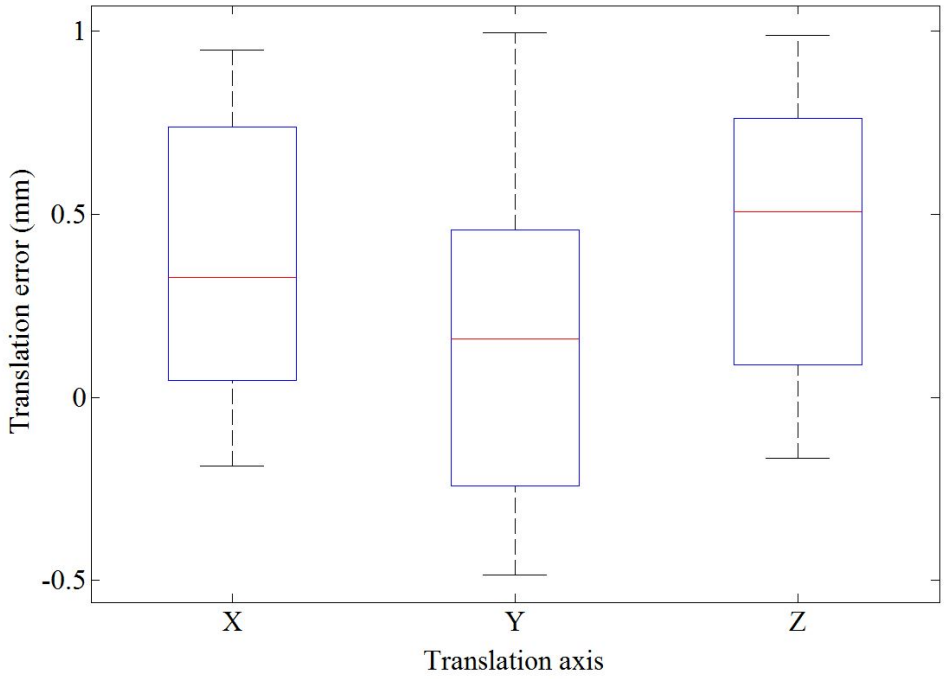

(a)

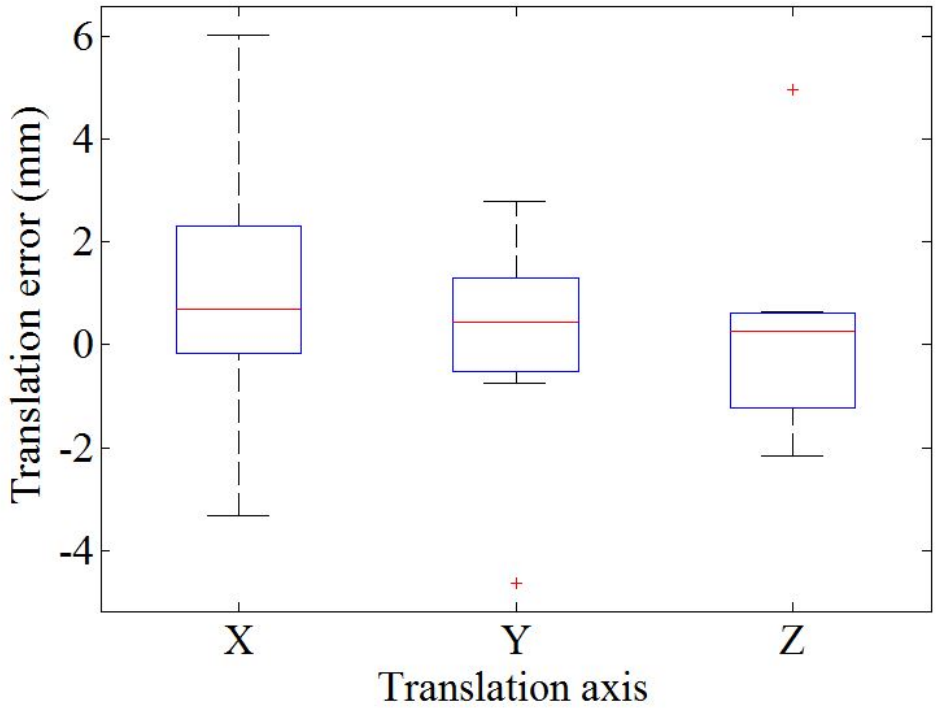

(b)

Figure 4.16: *Translation errors along three axes compared to the ground truth of a) the globally optimal ICP registration and b) the conventional ICP registration.*

From Figure 4.15 and Figure 4.16, the globally optimal ICP registration reduced the average absolute rotation error around three axes from 27.77° of the conventional ICP registration to 0.38°, and the average absolute translation error along three axes was reduced from 0.48 mm of the conventional ICP registration to 0.38 mm by utilising the globally optimal ICP registration. Although there was no significant difference between the average absolute translation error of the globally optimal ICP and the conventional ICP, because of the erroneous registration results from the conventional ICP registration, the variations of both the rotation errors and the translation errors of the conventional ICP were much bigger then the globally optimal ICP.

The elapsed time for a single registration between two reconstructed GT surfaces at different positions was approximately 20s, which was slower than conventional ICP (0.23s) because of the extra execution time for the BnB global search.

4.5 Conclusions

In this chapter, a globally optimal ICP registration algorithm has been employed as one important component of the computer-aided tracking and motion analysis with ultrasound (CAT & MAUS) system. The algorithm presented in this chapter integrated the BnB search scheme with the conventional ICP algorithm to guarantee a globally optimal solution without the necessity of a good initialization. This algorithm solved the issue of getting trapped into local minima of the conventional ICP algorithm.

The employed globally optimal ICP registration algorithm is especially effective to register two rigid bodies at two different positions without a good initialization. As the rigid bone is hard to locate during movement, in the previous MAUS system developed by Monk *et al.* [89], the same bony landmarks at different poses were identified by eye, which was time consuming (approximately 30 minutes per test) and less accurate. Thus, the function of the registration component within the CAT & MAUS system is to transform the bone of interest (i.e. the GT) from a reference pose to other gait poses

so that the actual GT could be located at different poses automatically. More detailed *in-vivo* experiments using globally optimal ICP registration will be presented in Chapter 6. Moreover, as the GT surfaces were reconstructed from manual segmentation, it was laborious and potentially prone to inter-observer error, which presents its own challenges and introduces potential for error. Thus, an automatic bone segmentation in US images will be presented in Chapter 5.

Chapter 5

Automatic Bone Segmentation

In this chapter, a novel automatic bone segmentation method is presented as an essential precursor for 3D reconstruction and registration to locate the target bony structure. As explained in Chapter 4, the bone surfaces used for registration were reconstructed from manual segmentation previously. However, manual segmentation was extremely laborious and the accuracy of the manual segmentation was highly dependent on "segmenter's" experience. An automatic patch-based tracking algorithm has been employed to locate the uniform bone structure when the probe was held at a fixed position in Section 3.3.2. However, the bone structure can appear differently in consecutive US images during a US sweep across the anatomy of interest when using the MAUS system. In order to extract an explicit 3D bone geometry from US sweeps, an automatic bone segmentation algorithm is developed based on the phase features and acoustic characteristics of US images to automate the full CAT & MAUS system and improve system accuracy. The content of this chapter has been published in the Proceedings of *International Symposium on Biomedical Imaging, 2016.*

5.1 Related segmentation methods

Bone structure segmentation in US images has numerous applications in computer-aided orthopaedic surgery (CAOS) to pre-operatively plan surgeries and/or intra-operatively navigate surgeries [37]. A reliable bone structure extraction method for ultrasound images is a precursor for an accurate 3D surface to surface registration stated in Chapter 4 [62]. Because of speckle and the indistinct anatomical boundaries in US images, it is nontrivial to automatically segment the bone structure reliably and accurately [37]. As a result, a 3D bone surface is usually reconstructed from manual 2D bone segmentation [11]. However, in order to reconstruct a 3D surface using the MAUS system, one or more US videos each with on average 350 frames must be segmented. Doing this manually is extremely laborious.

Automatic bone segmentation has previously been employed on US images [37] [48] [147]. Zhang *et al.,* calculated the bone likelihood and trimmed pixels far from the estimated bone boundary. An initial segmentation was drawn by the user and the estimate of the bone boundary was based on the boundary location in the last frame. As this segmentation was used for the later radial basis functional interpolation, they reported that there was no need to have a high level of accuracy for the segmentation, which was only accurate to 15 pixels. However, an accurate segmentation of the bone is required for an accurate registration in the next step. Foroughi *et al.,* used knowledge about the physics of US and the appearance of the bone structure in US images giving segmentation results accurate to 3 pixels (0.3 mm) [37]. They modelled the shadow effect of US as the sum of the Gaussian weighted pixel intensities in the shadow area to enhance the bone probability. However, in this application, their method was evaluated and compared with the method in Section 5.3. It was found to be sensitive to areas of strong acoustic response, like the fascia and other soft tissues, which can be incorrectly recognized as bone. Hacihaliloglu *et al.,* applied local phase features, including feature symmetry feature, to localize bone structures. The strength of that approach lay in the effectiveness of detect-

ing multiple bone structures in one frame. Because the feature symmetry feature returns high values in response to ridge-like areas [112], similar problems arose when ridge-like blobs would be mis-detected as bone structures.

In this chapter, a novel method for automatic bone structure segmentation in 2D US images using US physical information, local phase features and dynamic programming is introduced, which significantly decreases the number of erroneous detections of soft tissue as bone.

5.2 Automatic bone segmentation algorithm

The proposed automatic bone segmentation algorithm consists of two parts: bone probability mapping and dynamic programming optimization.

5.2.1 Bone probability mapping

In order to reduce the effect of speckle artefact in an US image, firstly, the pixel intensities of the US image are smoothed by a Gaussian kernel and the smoothed pixel intensities are normalized into the range 0-1 (Figure 5.1). The standard deviation of the Gaussian

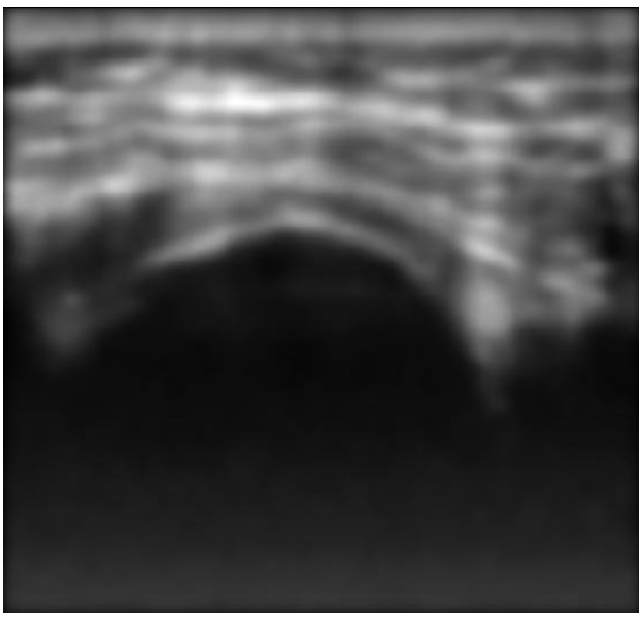

Figure 5.1: *The ultrasound image smoothed by a Gaussian filter ($\sigma = 6$).*

kernel depends on the thickness of the bone structure. As the Gaussian kernel smooths the US image, the higher the value of the standard deviation of the Gaussian kernel, the smoother the US image obtained. In this study, as the thickness of the bone structure is approximately 6 pixels in the US image, the standard deviation is set to 6 pixels. Speckle and other soft tissues under US whose sizes are smaller than the bone structure are smoothed out from the original US image as in Figure 5.1.

Then, based on the US imaging knowledge [2], internal physical characteristics of the US images are considered to get rid of redundant information within the US images. As the soft tissue between the skin and the greater trochanter (GT) is unlikely to be thinner than 5 mm (approximately 50 pixels in US images) and US image pixels with a normalized intensity lower than 0.125 are unlikely to be bony anatomy [62], a binary mask is employed to eliminate these pixels which are unlikely to be the bone structure. As these useless pixels are removed, it saves on processing time of the overall algorithm (Figure 5.2).



Figure 5.2: *The binary mask for the ultrasound image to get rid of useless pixels.*

Due to the large acoustic impedance difference between the bone and the soft tissue at the bone surface, the bone surface generates a strong reflection and appears as a bright ridge in the US images. Thus, it is more likely that pixels with a locally high intensity value correspond to the bone structure. A Laplacian of Gaussian (LoG) filter was reported to be effective to detect the blobs and smooth the noise in an image [71]. Similar to defining the standard deviation of the Gaussian kernel used in the smoothing step, the kernel length "l" and the standard deviation "σ" of the LoG kernel depend on the scale of the blob to be detected [26]. In this study, a LoG kernel with a kernel length of 3 pixels and a σ of 6 pixels is applied to detect the strong reflection response caused by the bone. The LoG filter gives positive responses to the dark areas on both sides of the bone structure, a negative response to the bright bone structure and zeros at the bone boundary. As only the negative responses indicate bright blobs, like bone structures, the negative responses are negated to give positive values and the rest, i.e. non-negative values, are zeroed as in Figure 5.3.

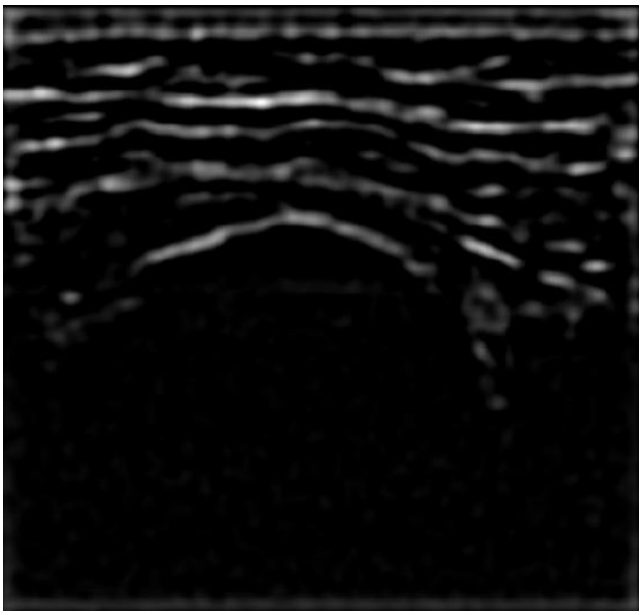

Figure 5.3: *The ultrasound image filtered by a Laplacian of Gaussian filter ($\sigma = 6$).*

Moreover, a bone structure appears as an intensity ridge and as such is a symmetric feature in an US image. Local phase features have been proved to be efficient at extracting ridge-like features [48] and are therefore applied to US images to enhance the probability of the bone detection. These local phase based filters are constructed using the monogenic signal which is composed of an odd part (asymmetric) denoted by $O(,)$ and an even part (symmetric) denoted by $E(,)$ [35]. The even part is the result of convolving the 2D US image $I(,)$ with bandpass filters, for example Gabor, log-Gabor, Poisson, Cauchy and others. In this study, we have focused on log-Gabor filters calculated as in Equation 5.1,

$$LG(\omega) = \exp\left(-\frac{\log\left(\frac{\omega}{\omega_0}\right)^2}{2\log(\sigma_0)^2}\right) \tag{5.1}$$

where ω_0 is the centre frequency of the passband which governs the scale of the structure. Structures with a scale approximately equal to that of the filter, $\lambda_0 = 2\pi/\omega_0$, will be selected. σ_0 governs the bandwidth of the bandpass filter. A visualization of a 2D log-Gabor in the frequency domain is shown in Figure 5.4a.

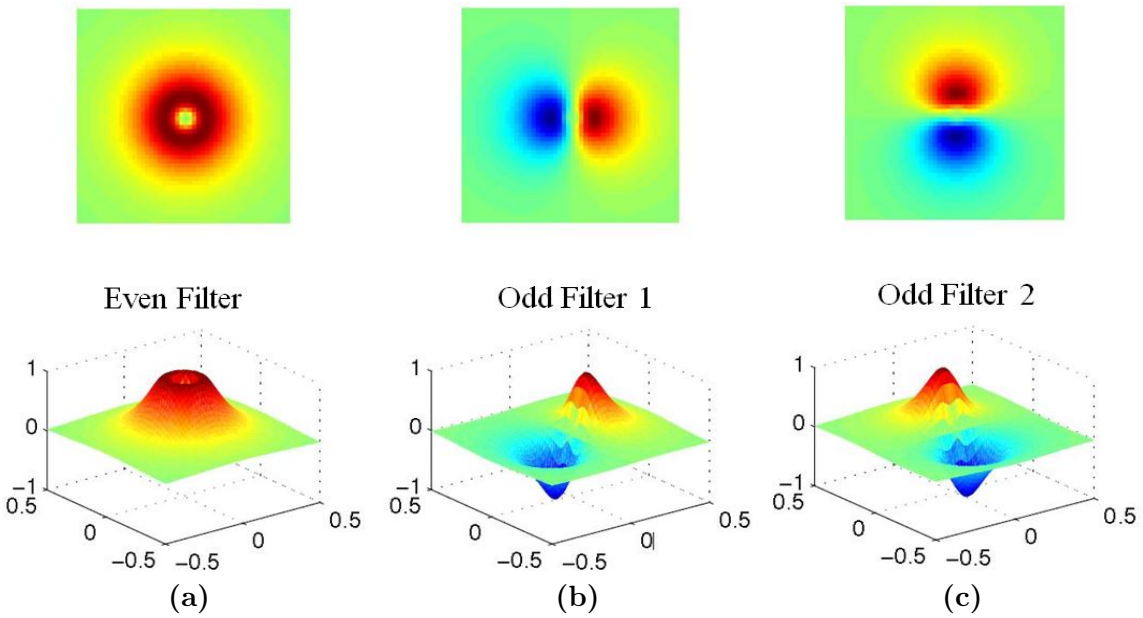

Figure 5.4: *Frequency-domain representations of 2D log-Gabor filter and the two parts after Riesz transformation a) the even filter, b) and c) the odd filters.*

Furthermore, as an US image is a 2D signal, there are two odd parts, O_1 and O_2, which are generated by convolving the 2D US image with the log-Gabor filter after a 2D *Riesz transform* (Figure 5.4b and 5.4c) [15] [82]. The odd part of the monogenic signal is then composed of these two odd parts as in Equation 5.2.

$$O(a,b) = \sqrt{O_1(a,b)^2 + O_2(a,b)^2} \tag{5.2}$$

The even filter highlights the symmetric structures in US images while the odd filter gives higher values to asymmetric structures in two dimensions.

Local intensity changes cause different local energies which are calculated by Equation 5.3.

$$LE(a,b) = E(a,b)^2 + O(a,b)^2 \tag{5.3}$$

A high value (red colour) in the local energy represents a high intensity change compared to the surrounding area (Figure 5.5).

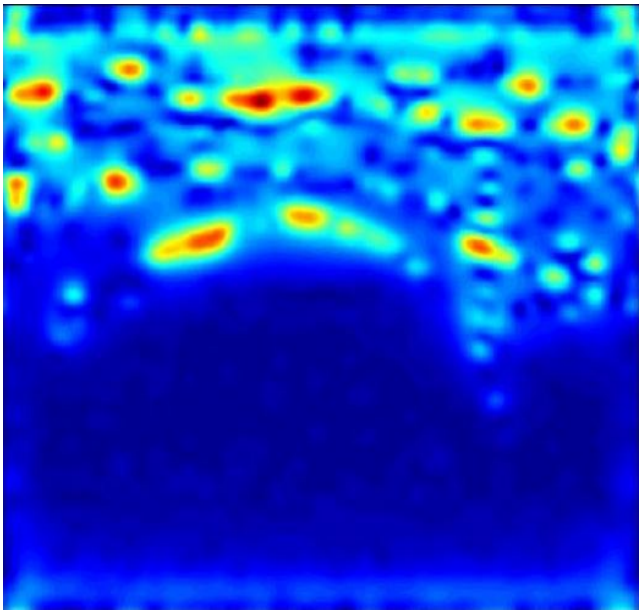

Figure 5.5: *The local Energy of the ultrasound image.*

Local phase is found from the angle between the even part and the odd part, which gives an phase information of the image (Equation 5.4).

$$LP(a,b) = \arctan\left(\frac{|O(a,b)|}{E(a,b)}\right) \tag{5.4}$$

As the top of a ridge-like pattern in an US image has a large even part and a small odd part, it presents a value of π (red colour) in the local phase shown in Figure 5.6.

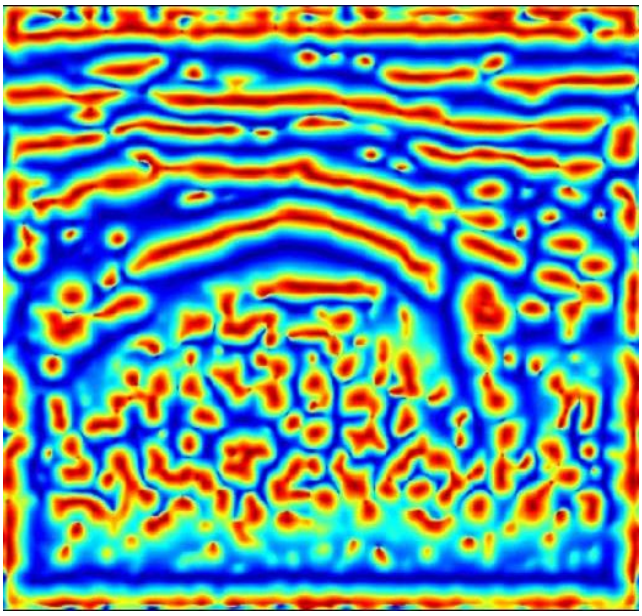

Figure 5.6: *The local phase of the ultrasound image.*

For a signal to be locally symmetric, all the constituent frequency components must be symmetric, i.e. all frequencies must have a phase of π. The bone structure is detected using multiple bandpass filters at different scales, i.e. different wavelengths λ_i, and the sum of the results gives the feature symmetry images as in Equation 5.5 to pick out features at the desired scale and ignore speckles and small scale soft tissue responses [72] [112].

$$FS(a,b) = \sum_i \frac{\lfloor |E_{\lambda_i}(a,b)| - |O_{\lambda_i}(a,b)| - T \rfloor}{\sqrt{LE_{\lambda_i}(a,b)} + \varepsilon} \tag{5.5}$$

where *FS(,)* is the feature symmetry of the US image, $\lfloor . \rfloor$ means values less than zero are

replaced with zero, T is the noise threshold and ε is a small number included to avoid division by zero. As bone structures appear as ridges in an US image, they return high values (red colour) in the feature symmetry images shown in Figure 5.7.

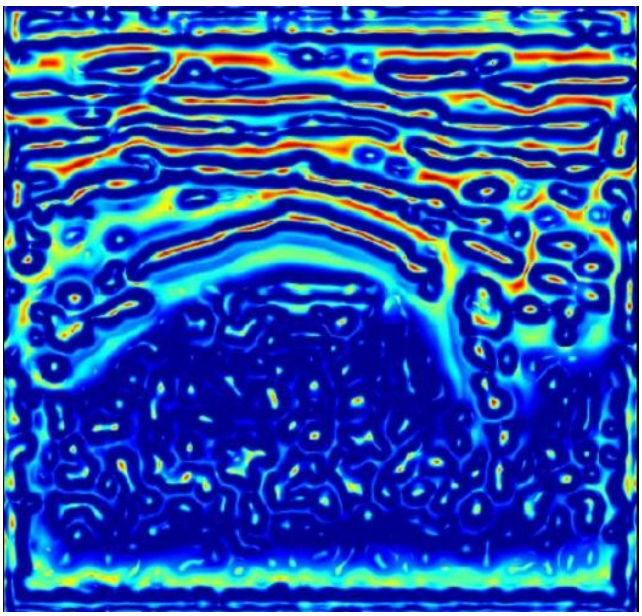

Figure 5.7: *The feature symmetry of the ultrasound image.*

However, soft tissues like the fascia are imaged as ridge-like patterns under US and give high responses in the local phase features. In order to reduce the interference from the unwanted soft tissues in US images, two well-known and prominent US physics features, the shadowing effect and the integrated backscattering (IBS) energy along US scan lines are exploited. As most of the ultrasonic waves are reflected at the bone surface, acoustic shadowing is present behind the bone, which appears to be dark in an US image [103]. A Gaussian weighted accumulation of the pixels below a given pixel is modelled as the shadow value *Shadow(a,b)* of the pixel at row a and scan line b according to Equation (5.6):

$$Shadow(a,b) = \frac{\sum_{j=a}^{R} G(j-a)I(j,b)}{\sum_{j=a}^{R} G(j,b)} \tag{5.6}$$

where R is the number of rows in the US image, *G()* is the Gaussian weighting function

and *I(,)* represents the pixel intensity. The Gaussian weighting function models the transition of high intensity pixels close to bone surface to the dark pixels deeper under the bone [37]. The shadowing effect is shown in Figure 5.8. A higher value in the shadowing map indicates a stronger shadow effect. Thus, by considering the shadowing effect, the bone structure is highlighted.

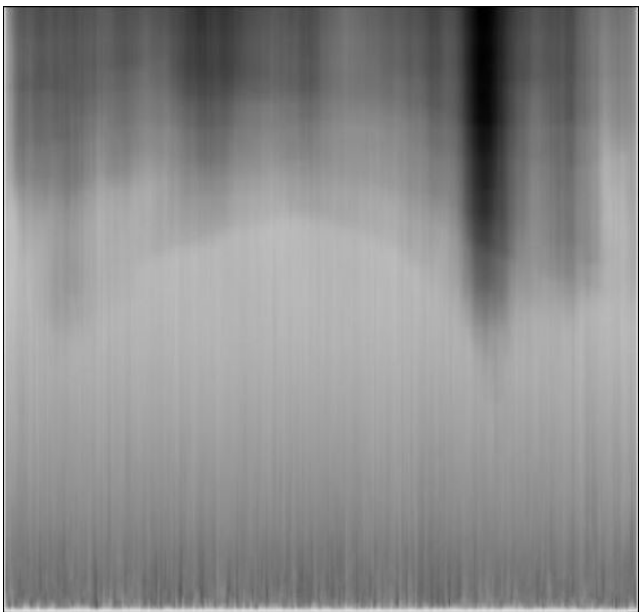

Figure 5.8: *The shadow map of the ultrasound image.*

Another feature caused by the US energy reflection at the bone surface is integrated backscattering energy. The sum of the pixels' intensity values above a given pixel is defined as the energy of integrated backscatters up until that point in the given scan line as in Equation 5.7.

$$IBS(a,b) = \sum_{j=1}^{a} I^2(j,b) \tag{5.7}$$

where $I(,)$ is the pixel intensity and j is the jth row of the US image. As a bone structure is expected to have higher acoustic impedance than the surrounding soft tissues, more US energy is backscattered at the top bone structure boundary. Thus, the bone structures and the areas below have a higher integrated backscattering energy value than the soft

tissues above the bone as shown in Figure 5.9. This efficiently reduces the erroneous detection of soft tissues above the bone as the bone structure.

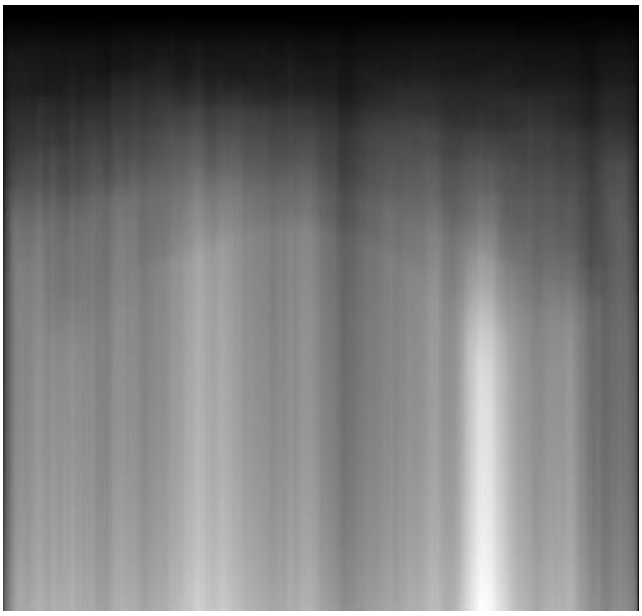

Figure 5.9: *The integrated backscattering map of the ultrasound image.*

The final bone probability map (Figure 5.10) is the normalized multiplication of the Gaussian smoothed image, the mask, the Laplacian of Gaussian of the US image, the local energy, the local phase, the feature symmetry, the shadow and the IBS energy. A threshold of the bone probability can be set to eliminate the noise probabilities.

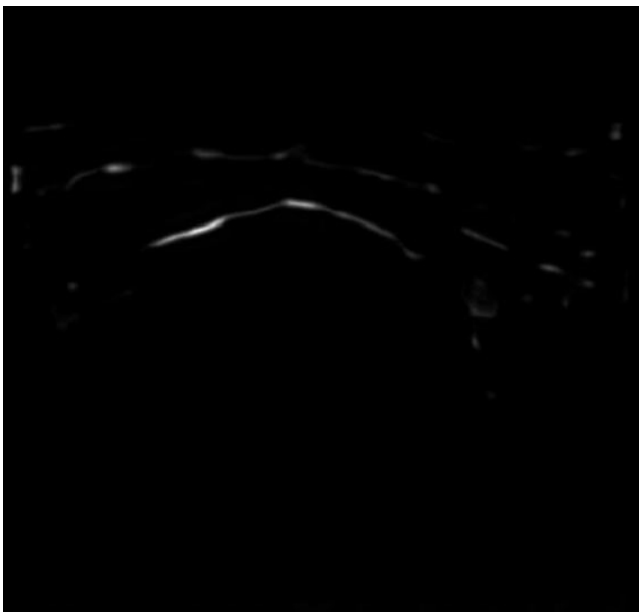

Figure 5.10: *Final bone probability mapping.*

5.2.2 Bone localization optimization

The greater trochanter (GT) appears as a downward crescent in 2D US images. To localize the GT bone structure, it is assumed that there is only one pixel in each scan line (column) of the US image that represents the bone. Each segmented pixel in each column must belong to one of the following three regions i.e. the *bone*, the *boneless* or the *jump* as shown in Figure 5.11.

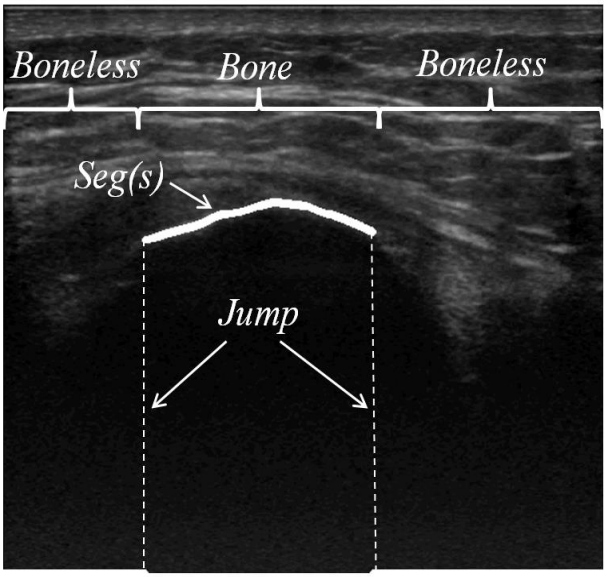

Figure 5.11: *Three parts of the bone segmentation Seg(s). Note: the white line is thickened for better visualization.*

A similar method to [37] has been followed to determine the existence of the bone structure, *Seg(s)*, and its location s by minimizing a cost function parametrized by s. The cost function is composed of internal and external energy components denoted as E_{int} and E_{ext} respectively. The external energy of a given pixel is defined as one minus the bone probability of that pixel. The internal energy incorporates connectivity and the smoothness of the bone segmentation, which is defined separately for the three parts of

the segmentation as defined by Foroughi *et al.,* [37]:

$$E_{int} = \begin{cases} \alpha \parallel \frac{dSeg}{ds} \parallel^2 + \beta \parallel \frac{d^2Seg}{ds^2} \parallel^2 + \gamma, & \textit{Bone region} \\ \text{JumpCost}, & \textit{Jump region} \\ \alpha {D_1}^2 + \beta {D_2}^2, & \textit{Boneless region} \end{cases} \tag{5.8}$$

where α,β are the weighting parameters for the smoothness (the first derivative of Seg) and the curvature (the second derivative of Seg), and γ is a small negative scalar to tune the connectivity and is set as one-tenth of the threshold applied on the bone probability map. s is the index of the current pixel. A $JumpCost$ penalizes the big jump between the *bone region* and *boneless region.* The smoothness and curvature are set to a constant value D_1 and D_2 respectively in the *boneless region* because there is no bone detection in the *boneless region.* In the implementation, both D_1 and D_2 are equal to 1 to reduce the overall sensitivity of the algorithm to the parameters α and β as they are the tuning parameters for the smoothness and curvature of the segmentation. The parameters α and β are adjusted for different images based on the bone probability profile and its connectivity in the bone probability mapping.

An example of how these two parameters affect the segmentation is shown in Figure 5.12. When a higher α and lower β are applied, a more complete bone structure is detected but there may be extra erroneous detection and it may lose the bone morphology details like the curve shape (Figure 5.12a). Similarly, lower α and higher β return a segmentation with a better bone alignment, which however may be an incomplete detection (Figure 5.12b). This is a trade-off to tune the parameters α and β to get the best segmentation results. Empirically, a value of 3 and a value of 1 are chosen for α and β respectively to get the best result (Figure 5.12c).

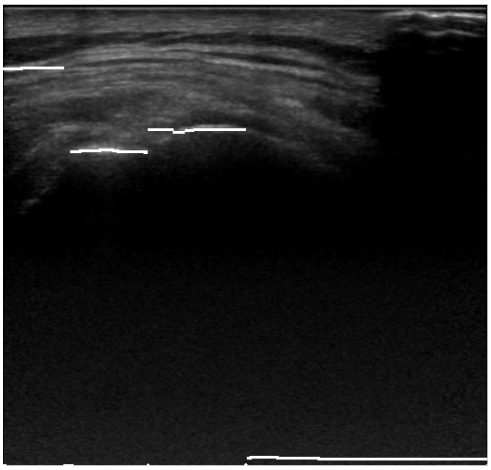

(a)

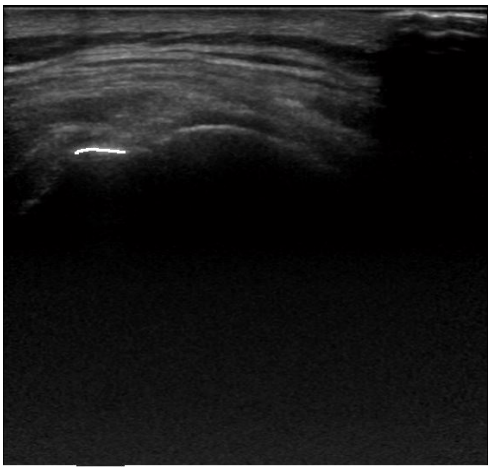

(b)

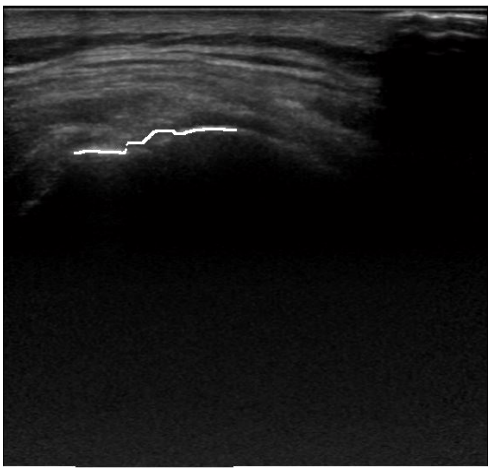

(c)

Figure 5.12: *Segmentation results after adjusting the parameters α and β, a) segmentation at $\alpha = 10$ and $\beta = 1$, b) segmentation at $\alpha = 1$ and $\beta = 10$, c) segmentation at $\alpha = 3$ and $\beta = 1$. Segmentation results have been thickened for better visualization.*

The cost of the segmentation is minimized by solving the recursive Equation 5.9, and the index of the pixel (k, j) with its minima stored as in Equation 5.10.

$$Segmin(i,j) = E_{ext}(i,j) + \min_{k}\{Segmin(k, j-1) + E_{int}(k,j)\} \tag{5.9}$$

$$Idxmin(i,j) = \underset{k}{\operatorname{argmin}}\{Segmin(k, j-1) + E_{int}(k,j)\} \tag{5.10}$$

where $Segmin(i,j)$ and $Idxmin(i,j)$ are the minimum cost and its index of the segmentation from the first column to the pixel in the ith row and j^{th} column. k is the row index.

Lastly, the optimal path is obtained by tracing back from the last column of the US image as in Equation 5.11:

$$Seg_{opt}(s) = \begin{cases} LR + 1, & s = LC \\ Idxmin[s+1, Seg_{opt}(s+1)], & s = 1, \cdots, (LC-1) \end{cases} \tag{5.11}$$

where Seg_{opt} is the optimal segmentation path with minimum energy cost. LR and LC indicate the number of rows and columns of the US image which also represent the last row and last column respectively.

The algorithm for the bone probability mapping was implemented in MATLAB (*MathWorks, R2014a, US*). The dynamic programming optimization was an open source implementation from [37] written as a MATLAB ".mex" function.

The data set contained 120 randomly selected US images of fifteen US videos (5013 frames) collected from the phantom test in Chapter 4 and 120 randomly selected US images of sixty US videos (16423 frames) collected from human volunteers in Chapter 6. A detailed description of data acquisition will be presented in Chapter 4 and 6. The size of all US images was 500×562 pixels (approximately 0.09mm per pixel side length). All the collected data were processed in MATLAB (*MathWorks, R2014a, US*) on a desktop computer (*8-core Intel Core i7-4770 3.40 GHz running a 64-bit Windows OS*).

The ground truth of the segmentation was constructed from the mean of the manual segmentation carried out by two experienced US imaging analysts (Christopher Bridge and Shanil Hansjee). The average intra-observer error over three separate segmentations on the same US image data set was 1.2 pixels, while the inter-observer error between them was 1.4 pixels. Results from this automatic segmentation were compared with the manually segmented ground truth and the results obtained using the method described in [37] with their best parameters set for the same data set.

5.3 Results

An example of a visual comparison between the probability maps of the method in [37] and this developed method is shown in Figure 5.13. In the bone probability mapping of this developed method (Figure 5.13b), the probability of detection of soft tissues above the bone as bone was significantly reduced by additionally employing local phase features and integrated backscattering energy information, which avoided the erroneous detection of the soft tissues as the bone structures.

Six representations of real US images, two of which were from the femur phantom (Figure 5.14a and Figure 5.14b) and the other four from the *in-vivo* test (Figure 5.14c to Figure 5.14f), with the manually segmented ground truth (red line) and automatic segmentation with both this developed method (white line) and the method in [37] (blue line) are shown in Figure 5.14.

On visual inspection, there appeared to be no difference in the segmentation results of the femur phantom using this developed method and the method in [37] with their suggested parameters as in Figure 5.14a and 5.14b. The femur phantom segmentation results were well aligned with the manually segmented ground truth as the femur phantom presented as a clear ridge-like pattern without any soft tissue noise above the bone structure in US images. However, besides the correctly segmented bone structure, extra incorrect detection of the soft tissues appeared in the *in-vivo* data set using Foroughi

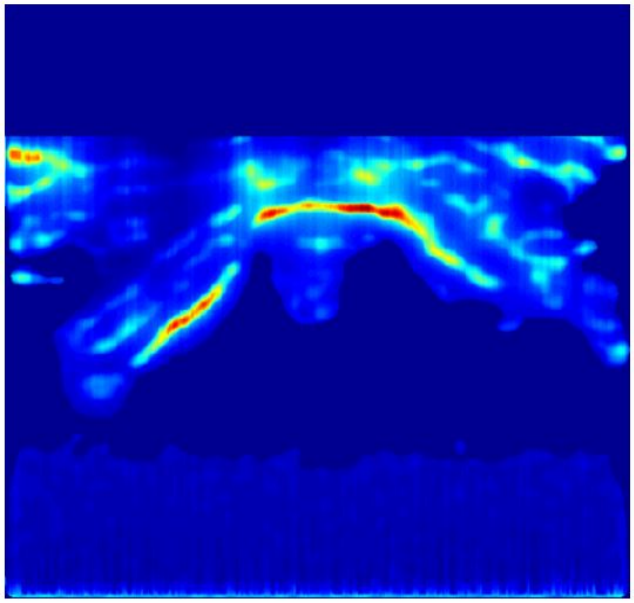

(a)

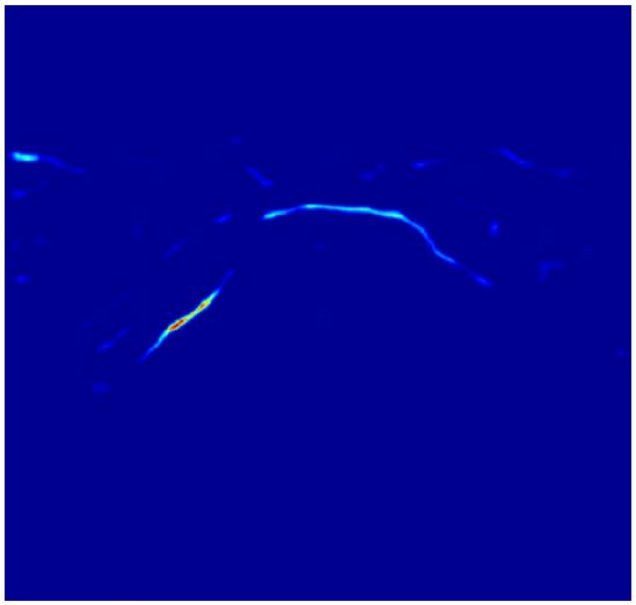

(b)

Figure 5.13: *Probability map comparison, a) probability mapping of the method in [37], b) probability mapping of the developed method.*

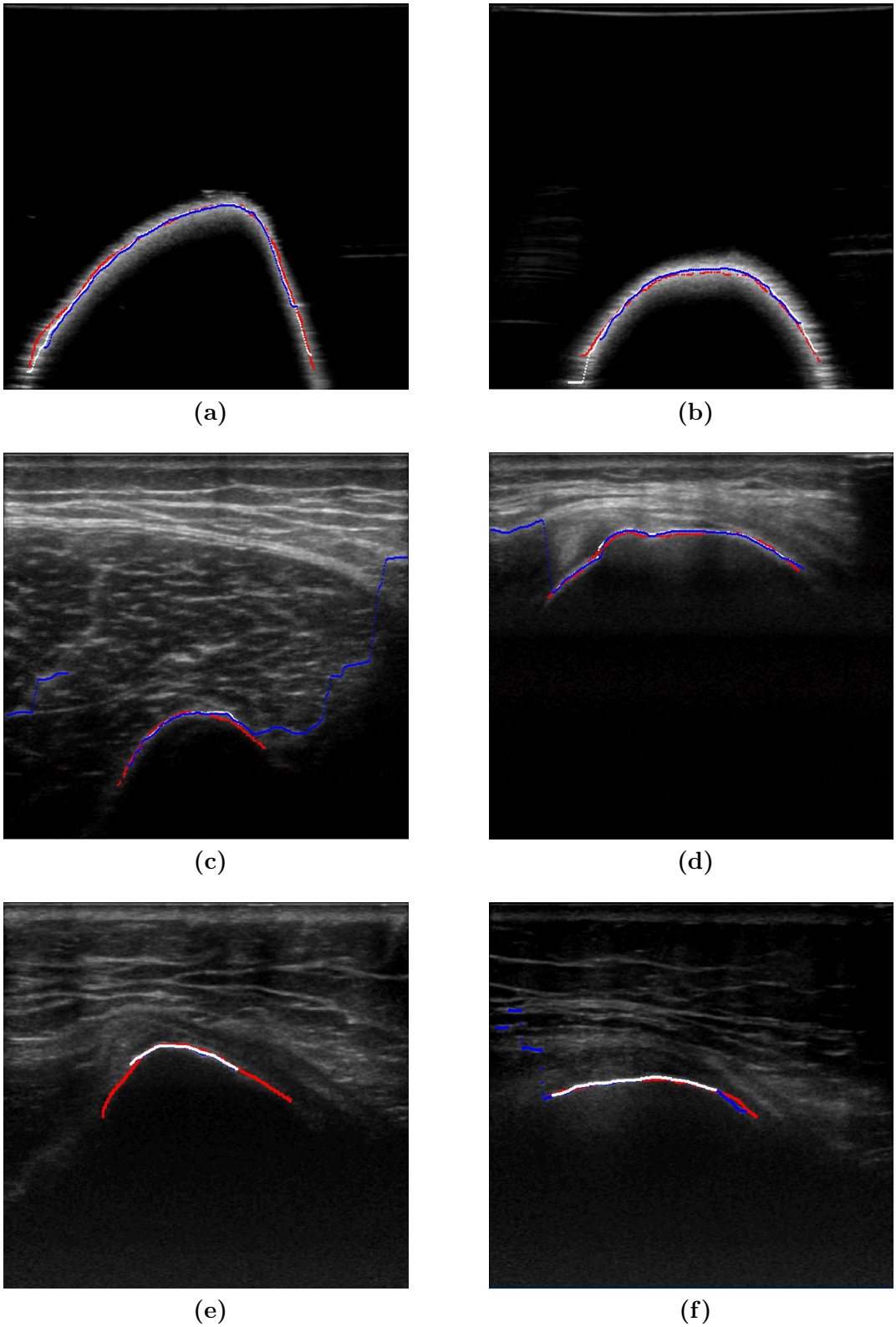

Figure 5.14: *The automatic segmentation results with this developed method (white line) and the method in [37] (blue line), and the manually segmented ground truth (red line), two different US representations of the phantom and four of the human greater trochanter. All the segmentation results are dilated for better visualization.*

et al.,'s method [37]. This is because those soft tissues with high intensity values also produce high values in the bone probability map which in other words have a low external energy cost in the optimization. Since multi-scaled bandpass filters were applied in this developed method to enhance the probability of bone structure detection and weaken detection of soft tissues, those unwanted soft tissue responses were eliminated efficiently. The segmentation results that were correctly localized within the clinical tolerance $\pm$ 1 mm (approximately 10 pixels) were counted as true positives. As explained in Section 5.2.1, a threshold was not directly applied to US images but on the bone probability map. When the probability map was thresholded with a high value, the erroneous detections of the soft tissue were reduced; however, the bone structure might not be completely detected, and *vice versa* for a low threshold. In many cases, the extent of the automatically segmented bone structure was less than that of the full manual segmentation, which leads to low overlapping percentages. This is because the indistinct appearance at the edges of the bone structure results in a lower bone probability. However, the detection of the full extent of the bone is not necessary for accurate registration later in the post-processing pipeline presented in Chapter 4. Moreover, in some cases, although the true positive detection rate from [37] is higher than this developed method, it meanwhile detects more false positive. The extra erroneous detections poorly affect the accuracy of later registration (Chapter 4).

A comparison between the ground truth (from manual segmentation) and each of the results using this developed method with different thresholds and the results on the same data set using the method in [37] with different thresholds are shown in Table 5.1a and Table 5.1b respectively. In the comparison, the number of erroneous detection frames, where there are false positive detections, is counted and listed in the second column. The number of missed detection frames, where there is no true positive detection, is listed in the third column. As the bone probability map gives a low response at the ends of the visible bone region, the automatic segmentation is never longer than the manual segmentation. Therefore, the maximum Euclidean distance (ED) error in pixels between

the true positive automatic segmentation and the manual segmentation of the same length is listed in the fourth column. The average percentage of pixels on the ground truth path that are correctly segmented within the clinical tolerance ± 1 mm (approximately 10 pixels) is calculated over the whole data set and listed in the last column of Table 5.1a and Table 5.1b. Since the range of the probability map after considering the IBS energy and local phase features is different from the method in [37], the segmentation results on the same US data set using each of this developed algorithm and the method in [37] with different threshold values are compared to the manual segmented ground truth in Table 5.1). When a lower threshold was applied on the probability map, there were more frames with erroneous detections and fewer frames with no detection, and *vice versa*. A threshold of 0.15 gave the best performance using this developed method while a threshold of 0.55 gave the best performance for the same data set using the method in [37], which are highlighted in Table 5.1a and Table 5.1b respectively. In Tables 5.1b, the best result from the method in [37] has more frames with erroneous detection and less average overlapping percentage than the developed method. It indicates that the erroneous detection of the soft tissues as the bone is effectively reduced by introducing local phase features and the acoustic characteristics into the bone probability mapping.

The average execution time for segmenting a single US image over those 120 randomly selected US images for the method presented in this chapter was compared with Foroughi's method [37]. An US image with pixel size 500×562 was segmented in approximately 4.1 seconds while the algorithm in [37] took around 5.3 seconds as more pixels satisfied the threshold criteria with Foroughi's method.

Threshold	Err. detection (frame)	Mis. detection (frame)	Max. ED error (pixel)	Avg. overlapping percentage (%)
0.05	27	0	0.84	63.81
0.10	19	0	1.07	62.46
0.12	10	0	1.24	59.39
0.15	2	0	1.33	57.26
0.18	1	5	1.37	52.33
0.20	1	13	1.38	50.36
0.25	1	18	1.38	46.68

(a)

Threshold	Err. detection (frame)	Mis. detection (frame)	Max. ED error (pixel)	Avg. overlapping percentage (%)
0.45	31	0	0.82	61.64
0.50	23	0	1.04	58.65
0.52	12	2	1.26	53.77
0.55	2	6	1.34	51.21
0.58	2	10	1.36	48.64
0.60	1	15	1.38	46.22
0.65	1	21	1.38	41.36

(b)

Table 5.1: *An comparison between the manually segmented ground truth and a) the results using this developed method with different thresholds, and b) the results on the same data set using the method in [37] with different thresholds. The thresholds highlighted in grey gave best results for each of these two methods.*

5.4 Conclusions

In this chapter, an automatic bone structure segmentation algorithm for US images has been presented. The bone structure was segmented based on a bone probability map composed of acoustic characteristics (shadow effect and IBS energy) and local phase features (local phase, local energy and feature symmetry features). By taking into account these acoustic characteristics, it significantly reduced the probability of soft tissues above the bone while the local phase features are proved to be sensitive to the ridge-like patterns. Those features enhanced the probability of the bone and reduced the probability of other image noise, which led to a more robust segmentation. Dynamic programming was employed to minimize the path energy cost that incorporated the bone probability, the smoothness and the continuity of the segmented path. The algorithm has been evaluated on 120 randomly selected US images obtained from a proximal femur phantom and another 120 randomly selected US images obtained from 10 healthy volunteers. It achieved an excellent accuracy with the average Euclidean distance error of the true positive detection at 1.33 pixels (approximately 0.13mm) and is superior to a previous method [37]. In the computer-aided post-processing pipeline, this developed automatic segmentation algorithm acts as a precursor to the 3D surface-to-surface registration (Chapter 4) which automates the CAT & MAUS system and improves system accuracy.

Chapter 6

Quantitative Study of *In-vivo* Hip Joint Kinematics During Gait

In this chapter, hip joint kinematics of healthy subjects during gait is quantified using the validated computer-aided tracking and motion analysis with ultrasound (CAT & MAUS) system introduced in previous chapters. A complete pipeline schematic of the CAT & MAUS system is shown in Figure 6.1. The system hardware setup was presented in Chapter 3 followed by the automatic bone segmentation in ultrasound (US) images in Chapter 5 and the globally optimal registration algorithm in Chapter 4. From the registration result, the bone of interest (i.e. greater trochanter in this research) can be located in preparation for estimating a description of joint kinematics. To quantify hip joint kinematics, firstly, the data acquisition procedure for the *in-vivo* experiments is described. A definition of hip joint kinematics adapted from recommendations of the International Society of Biomechanics (ISB) is then presented. The results monitored by CAT & MAUS are compared with the results from the motion analysis (MA) system alone. A version of this chapter has been published in the proceedings of the *BMVA:IET Human Motion Analysis for Healthcare Applications* conference [67]. A description of the full CAT & MAUS system and *in-vivo* tests has been published in the *International Journal of Computer-Assisted Radiology and Surgery* [64].

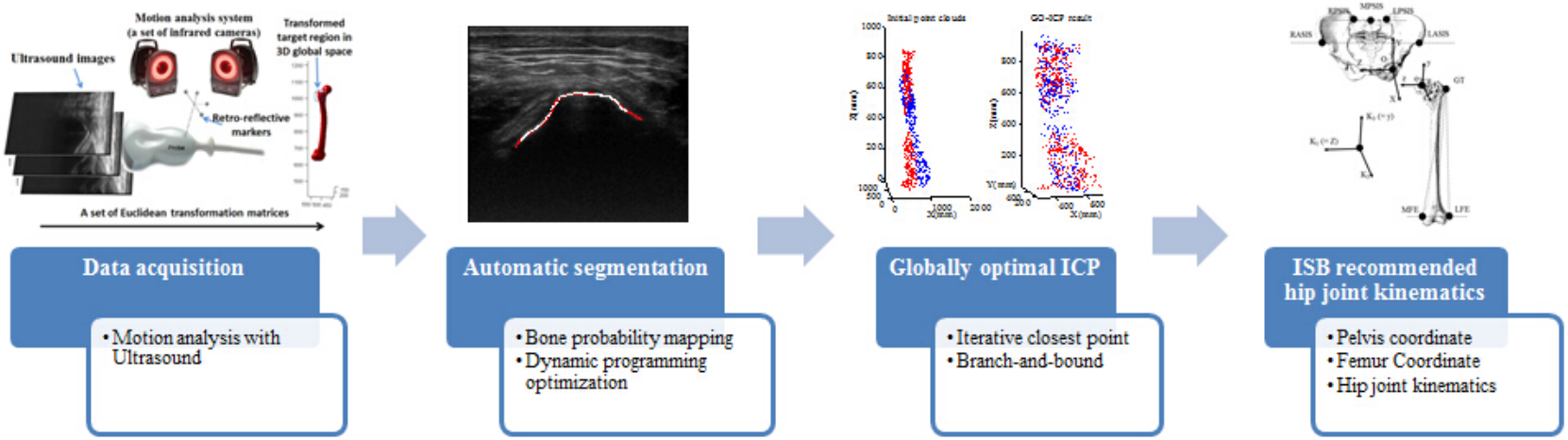

Figure 6.1: *A pipeline schematic of the CAT & MAUS system.*

6.1 *In-vivo* experiment

All the *in-vivo* tests were conducted in the Oxford Gait Laboratory, which is accredited by the Clinical Movement Analysis Society of UK and Ireland (CMAS) and is a member of the European Society of Movement Analysis in Adults and Children (ESMAC), with the same experiment settings for the phantom study as described in Chapter 3 and Chapter 4. The most commonly utilised optoelectronic motion analysis system suffers from soft tissue artefact (STA) which may cause an error up to 50 mm [1]. CAT & MAUS avoids the error caused by STA. To prove this, the results from CAT & MAUS and the results from MA alone are analysed and compared using Procrustes analysis in this section.

6.1.1 Data acquisition

Ten healthy volunteers (5 males and 5 females) with a mean age of 26 years (range 18-36 years) were recruited. Their anthropometric parameters were measured including the height, weight, left leg length and foot length, and these are listed in Table 6.1. All the volunteers were slim to average body-build weighted from 49.4 kg to 68.1 kg with heights from 160.1 cm to 185.2 cm. Calculated from their height and weight as in Equation 6.1, the average body mass index (BMI) is 20.15 ranging from 18.9 to 21.7.

$$BMI = \frac{Weight_{(Kg)}}{Height^2_{(m)}} \tag{6.1}$$

The World Health Organization regards a BMI within the range of 18.5 - 25 as healthy [97]. In this research, all experiments were conducted on the left leg of each subject. Thus, all results presented in this chapter are focused on the left leg. The average left leg length of the females was 91.2 cm and 99.3 cm for males. Their average left foot length was 23.3 cm for females and 25.7 cm for males. All ten volunteers had no known hip joint conditions and no joint replacements.

Volunteer No.	Gender	Height	Weight	BMI	Left leg length	Right leg length	Left foot length	Right foot length
1	Female	160.1 cm	49.4 kg	19.1	87.3 cm	86.0 cm	22.5 cm	22.5 cm
2	Female	160.2 cm	50.1 kg	19.5	92.0 cm	91.7 cm	23.0 cm	22.5 cm
3	Female	165.7 cm	54.0 kg	19.5	92.9 cm	94.1 cm	24.0 cm	23.0 cm
4	Female	166.2 cm	56.1 kg	20.3	93.2 cm	94.1 cm	23.0 cm	23.0 cm
5	Female	166.2 cm	56.2 kg	20.3	92.1 cm	91.4 cm	24.0 cm	24.0 cm
6	Male	168.9 cm	62.3 kg	21.7	96.8 cm	95.6 cm	26.0 cm	26.5 cm
7	Male	176.8 cm	67.3 kg	21.3	97.2 cm	98.5 cm	27.0 cm	27.5 cm
8	Male	178.0 cm	65.0 kg	20.5	97.0 cm	95.4 cm	24.0 cm	24.5 cm
9	Male	181.4 cm	68.1 kg	20.3	94.1 cm	94.0 cm	24.5 cm	24.5 cm
10	Male	185.2 cm	65.1 kg	18.9	106.9 cm	107.2 cm	27.5 cm	27.0 cm

Table 6.1: *Anthropometric parameters of the ten healthy volunteers.*

To model the lower limbs of the test subject, all bony landmarks on lower limbs were firstly represented by skin-based retro-reflective markers. The markers were attached on the skin by following a standard Helen Hayes configuration [23] with an extra 10 markers on the lower limbs including pelvis, femurs, tibias and feet as in Figure 6.2. All the bony landmarks are listed in Table 6.2 along with details of how they were tracked.

Body segments	bony landmarks	Description	Tracking method
Pelvis	**LASIS**	Left Anterior Superior Iliac Spine	MA
	RASIS	Right Anterior Superior Iliac Spine	MA
	LPSIS	Left Posterior Superior Iliac Spine	MA
	MPSIS	Mid Posterior Superior Iliac Spine	MA
	RPSIS	Right Posterior Superior Iliac Spine	MA
Left Femur	**LGT**	Left Greater Trochanter	MA/CAT & MAUS
	LMF	Left Mid Femur	MA
	LFW	Left Femur Wand	MA
	LLFE	Left Lateral Femoral Epicondyle	MA
	LMFE	Left Medial Femoral Epicondyle	MA
Right Femur	**RGT**	Right Greater Trochanter	MA
	RMF	Right Mid Femur	MA
	RFW	Right Femur Wand	MA
	RLFE	Right lateral Femoral Epicondyle	MA
	RMFE	Right Medial Femoral Epicondyle	MA
Left Tibia	**LTT**	Left Tibial Tuberosity	MA
	LMT	Left Mid Tibia	MA
	LTW	Left Tibia Wand	MA
Right Tibia	**RTT**	Right Tibial Tuberosity	MA
	RMT	Right Mid Tibia	MA
	RTW	Right Tibia Wand	MA
Left Foot	**LLM**	Left Lateral Malleous	MA
	LMM	Left Medial Malleous	MA
	LH	Left Heel	MA
	LT	Left Toe	MA
Right Foot	**RLM**	Right Lateral Malleous	MA
	RMM	Right Medial Malleous	MA
	RH	Right Heel	MA
	RT	Right Toe	MA

Table 6.2: *Bony landmarks of lower limbs and the methods used to track these landmarks.*

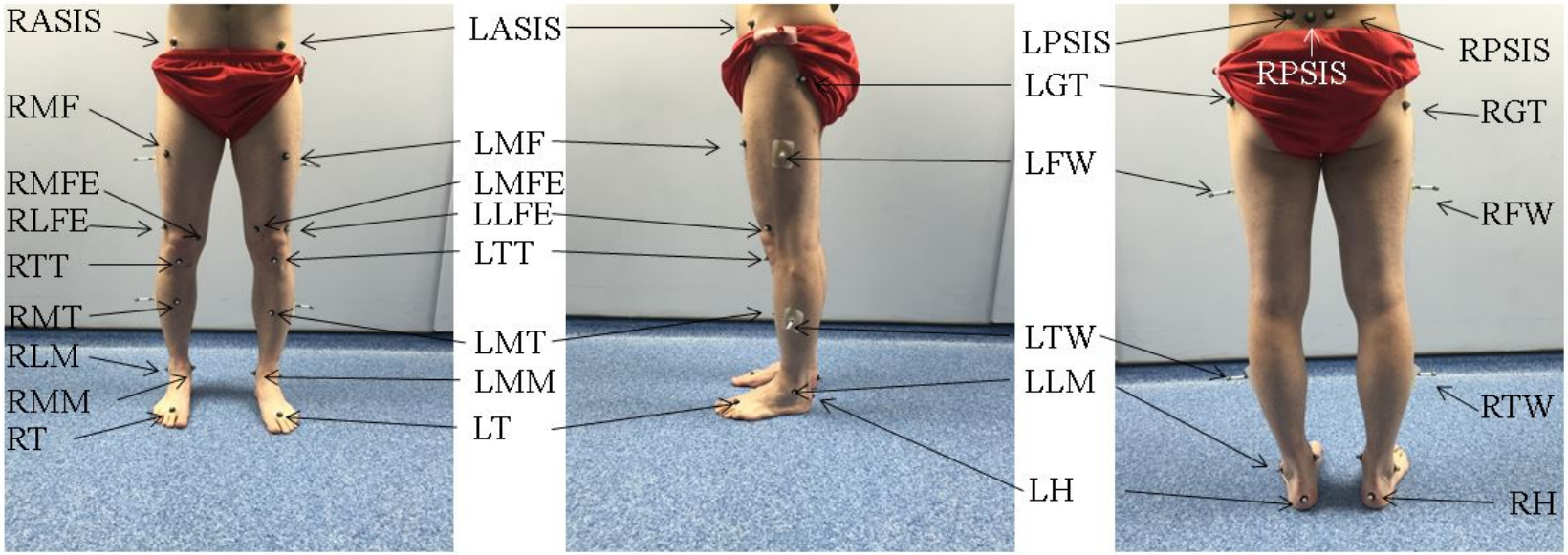

Figure 6.2: *Retro-reflective markers attached on one test subject in the front, sagittal and back views.*

A volunteer was then asked to perform the upright standing pose as in Figure 6.2 and four gait poses from one gait cycle, including heel strike, mid stance, toe off and mid swing of volunteer's left leg as shown in Figure 6.3. The heel strike pose of the left leg occurs when the left heel first makes contact with the ground during gait. The mid stance pose of the left leg is the mid point of the period during which the left leg supports the entire body weight. The toe off position of the left leg is the final period of foot contact during the left leg stance phase, where the toe of left foot is about to leave the ground. The mid swing pose of the left leg is the mid stance of the right leg where the left swing leg passes the right stance leg. As the single support stance phase and the swing phase together occupy about 80% of the gait cycle, the mid points of the stance phase and the swing phase are considered.

In order to compare the results from the CAT & MAUS system and the results from the motion analysis system alone (i.e. without US), all the markers attached on the skin, including the left greater trochanter (LGT), were firstly captured by the motion analysis system at each of those five positions as in Figure 6.4. The data captured by the motion analysis system alone is referred to as MA data for short. Similarly, the data captured by the CAT & MAUS system is abbreviated as CAT & MAUS data. The MA data were then processed in the VICON Nexus 2.2.2 package (*VICON, Oxford, UK*) in order to create a model of the volunteer's lower limbs in 3D space. Each part of the lower limbs was segmented and is presented with a different colour in subsequent diagrams. The left leg is coloured green, the right leg is coloured blue, and the pelvis is coloured yellow. From marker positions in the 3D space, the rotations of the hip joint between different positions were calculated as in Section 6.2.

Pose	Sagittal view	Front view	Back view
Heel strike			
Mid stance			
Toe off			
Mid swing			

Figure 6.3: *Four gait poses (heel strike, mid stance, toe off and mid swing) of the left leg in the sagittal, front and back views.*

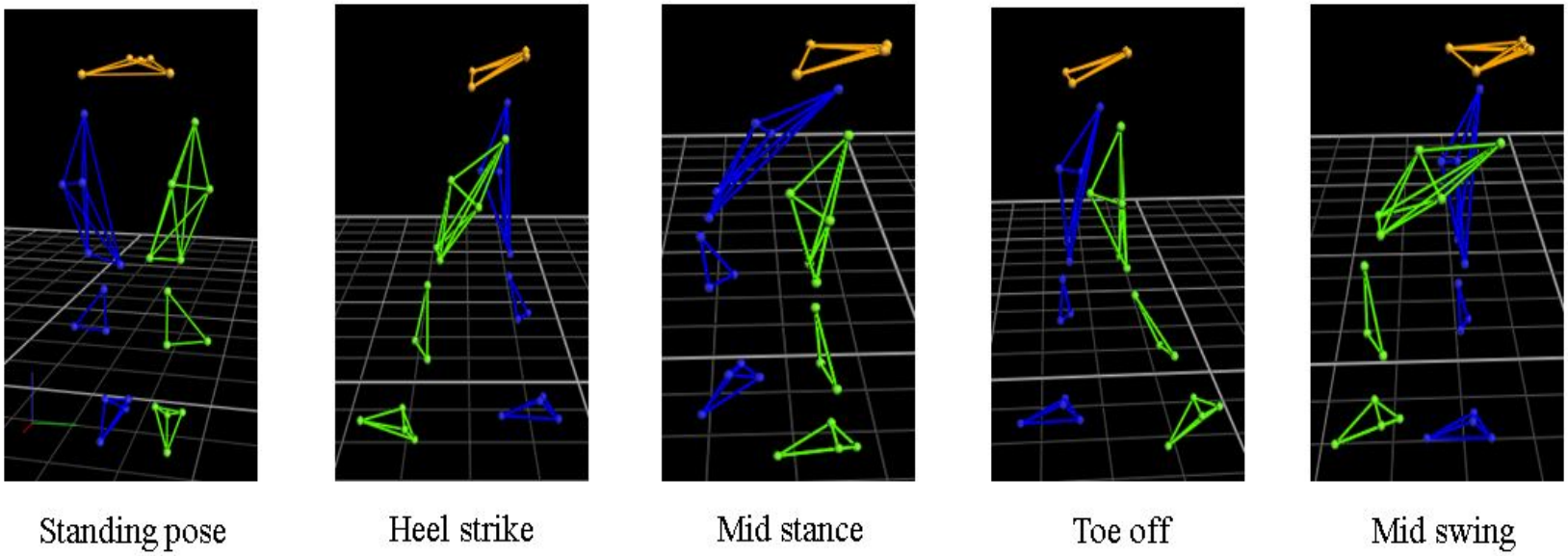

Figure 6.4: *Motion analysis data of the lower limb model at five different poses.*

To collect data using the CAT & MAUS system, the marker on the LGT was detached. Instead, the LGT was scanned using a 2D US probe in a parallel sweep as in Figure 6.5. During the US sweep, all the rest of markers on the lower limbs and the four markers attached on the probe were captured by the motion analysis system. The LGT surface

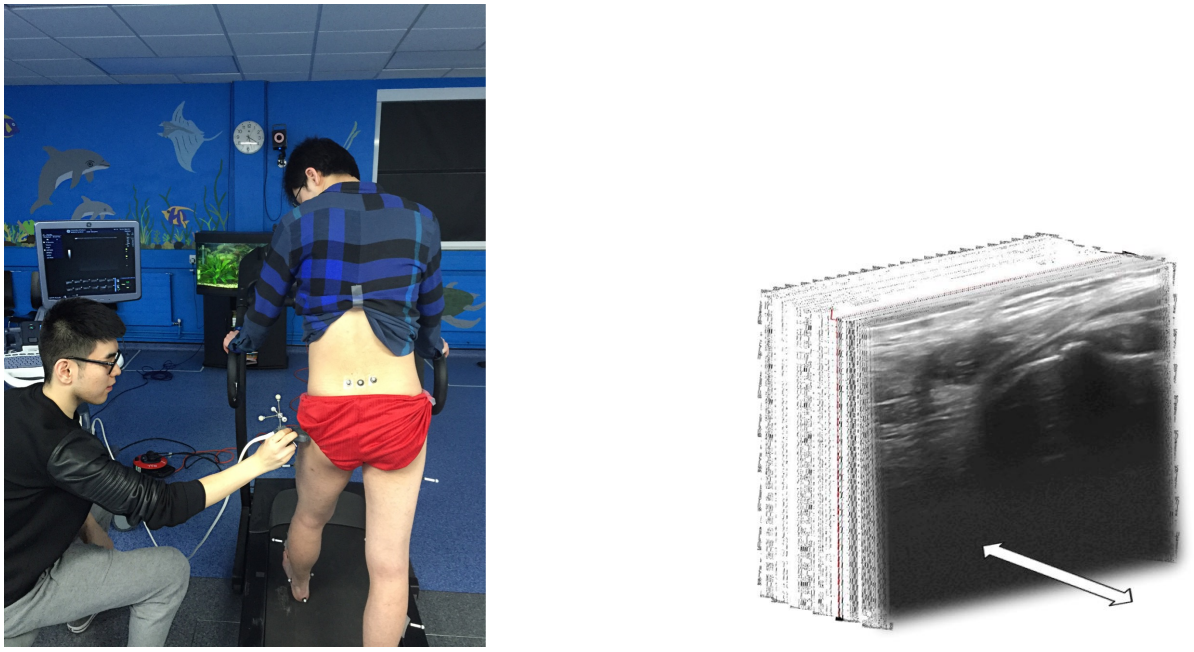

(a) **(b)**

Figure 6.5: *The LGT capture using CAT & MAUS, a) in-vivo data acquisition and b) US scanning in a parallel sweep.*

was then reconstructed by transforming the segmented bone structures in 2D US images into 3D space based on the position information of the probe markers as described in Chapter 3 and 5. Similar to the data acquisition protocol used for the motion analysis system alone, the volunteer was asked to perform the upright standing pose and the four gait poses (heel strike, mid stance, toe off and mid swing) again without the LGT marker. The LGT of the volunteer was scanned and reconstructed while all the rest of the markers on the subject's lower limbs and the US probe were captured by the motion analysis system at those five poses in turn as in Figure 6.6. Although the volunteer was asked to remain in a static pose, this was difficult to do in practice. Thus, to correct the error caused by the body movements, all the frames of motion analysis data of a given trial were registered to the first frame of that trial based on the pelvis position.

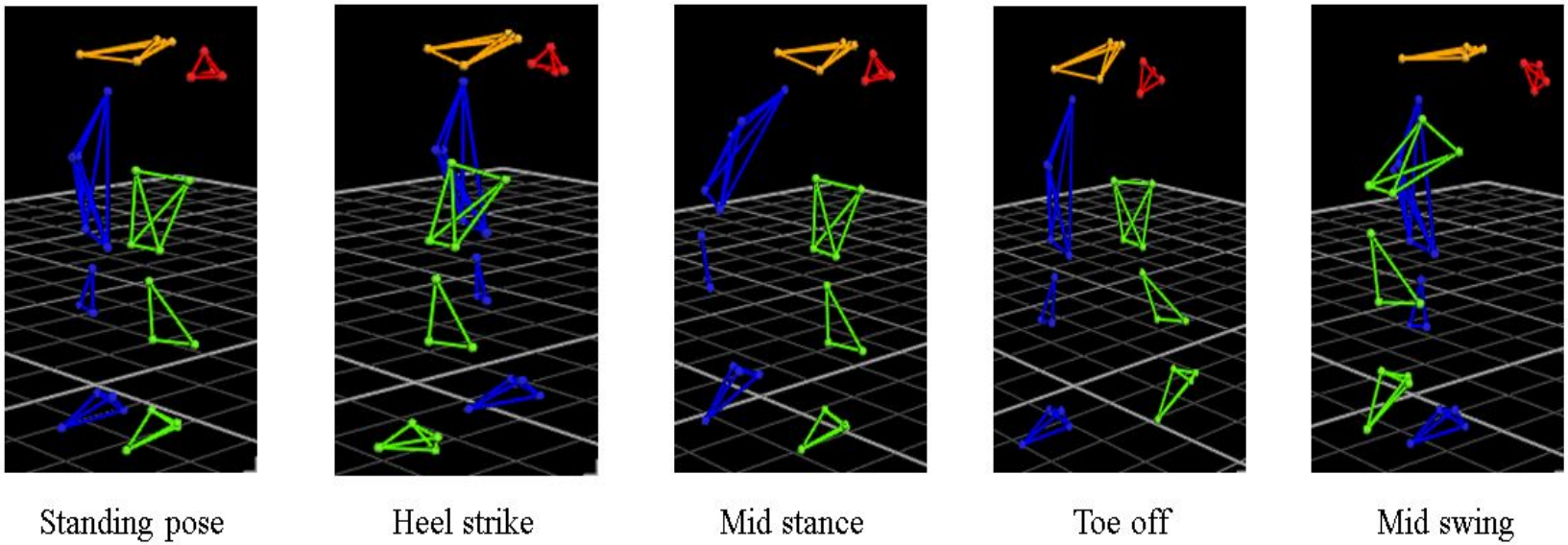

Figure 6.6: *CAT & MAUS data of the lower limb model at five different poses captured by the motion analysis system.*

In the previous MAUS system [88], by eye it was difficult to locate the same bony landmark at different poses. Therefore, the target LGT was selected as the outermost convexity of the reconstructed 3D LGT surface at the standing pose (the cyan cross in Figure 6.7) to automatically transform to the other position by the globally optimal registration result. The LGT surfaces at the four chosen gait poses were reconstructed

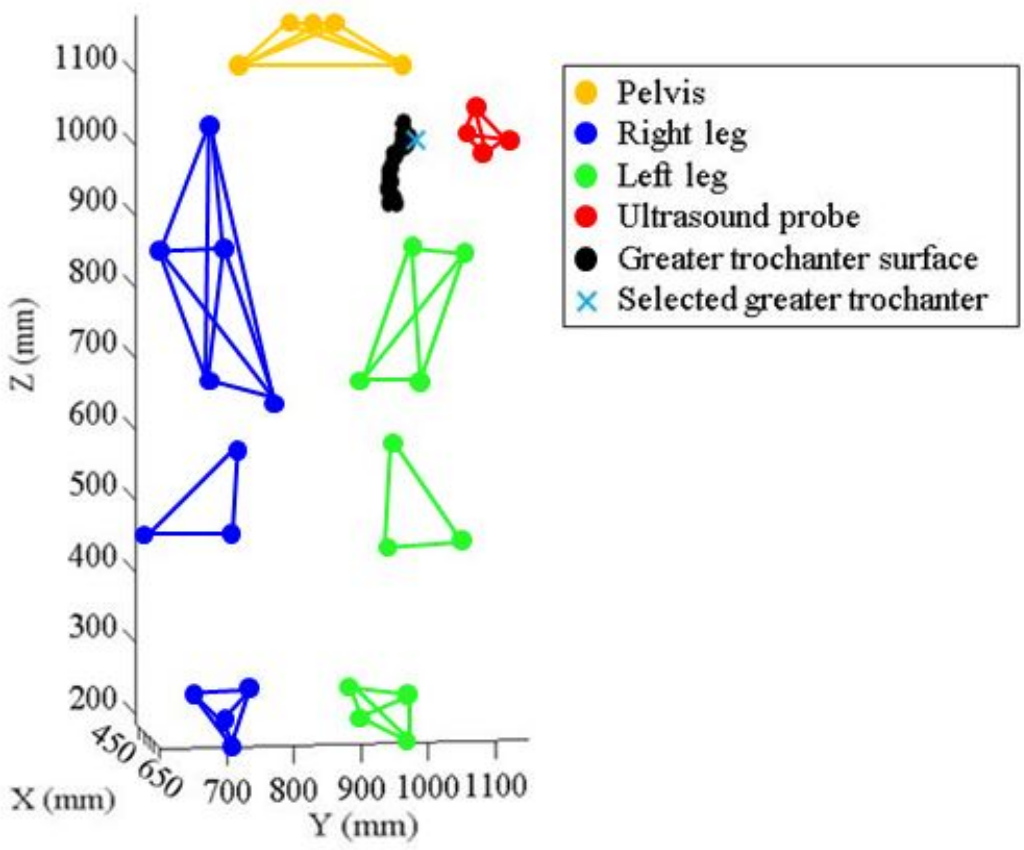

Figure 6.7: *The lower limbs MA model with the CAT & MAUS reference surface of greater trochanter reconstructed at the upright standing pose and the selected greater trochanter bony landmark superimposed.*

in the same way as for the standing pose. Each of these four surfaces were registered to the LGT surface at the standing pose using the globally optimal ICP registration algorithm presented in Chapter 4. One example of the registration between the surfaces at the standing pose and the toe off pose is shown in Figure 6.8. The transformation, i.e. translation and rotation, from the reference LGT surface at the standing pose to the LGT surface at the gait pose was calculated as the inverse transformation matrix

from the surface registration result. Then the position of the LGT at the gait pose was be calculated by transforming the selected LGT point at the standing pose using the transformation matrix. By replacing the marker-based LGT position measurement with the CAT & MAUS measurement, the error caused by the soft tissue artefact was reduced, as explained in Section 6.1.2.

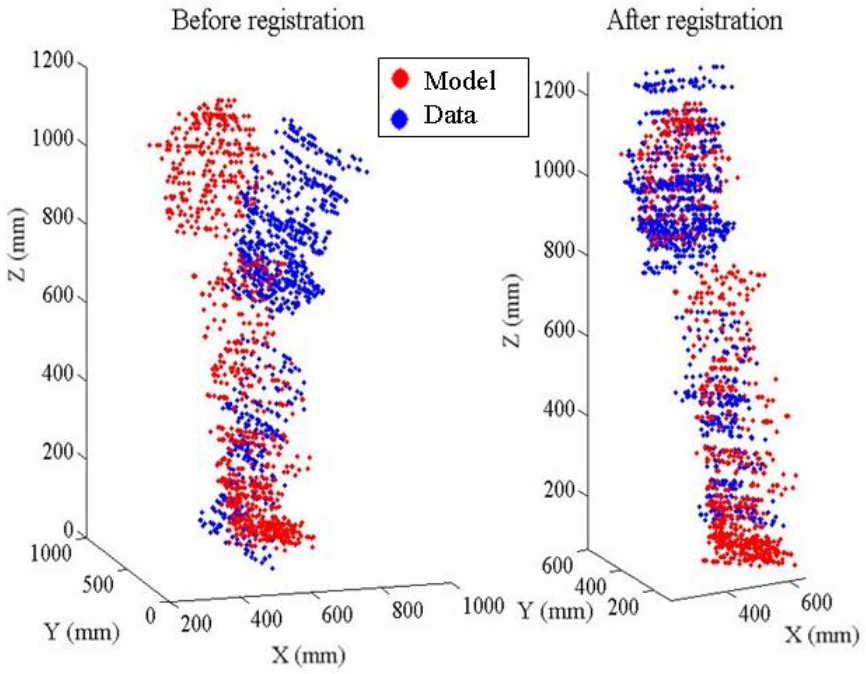

Figure 6.8: *An example of greater trochanter localization using globally optimal registration.*

6.1.2 Procrustes analysis

Each volunteer was examined three times using each of the motion analysis (MA) system alone and the CAT & MAUS system. The shape difference of the volunteer's gait pose over three examinations and the difference of the left femur shape modelled by MA and CAT & MAUS were quantified using Procrustes analysis. The first aim of using Procrustes analysis was to measure the repeatability of the measurements from each technique over three examinations at each pose. The second aim was to illustrate that CAT & MAUS reduces the deformation of the femur segment caused by soft tissue artefact during movements relative to MA alone.

Procrustes analysis has been used previously to assess STA [143]. It is a form of statistical shape analysis used to compare the shapes of a set of objects [118]. In this study, the comparison between two lower limb body segments made up from a finite number, k, of landmarks in three dimensions was considered. The MA data points were split into seven lower limb body segments: pelvis, left and right femurs, tibiae and feet as in Figure 6.9. The point set of the first body segment in 3D space is denoted as

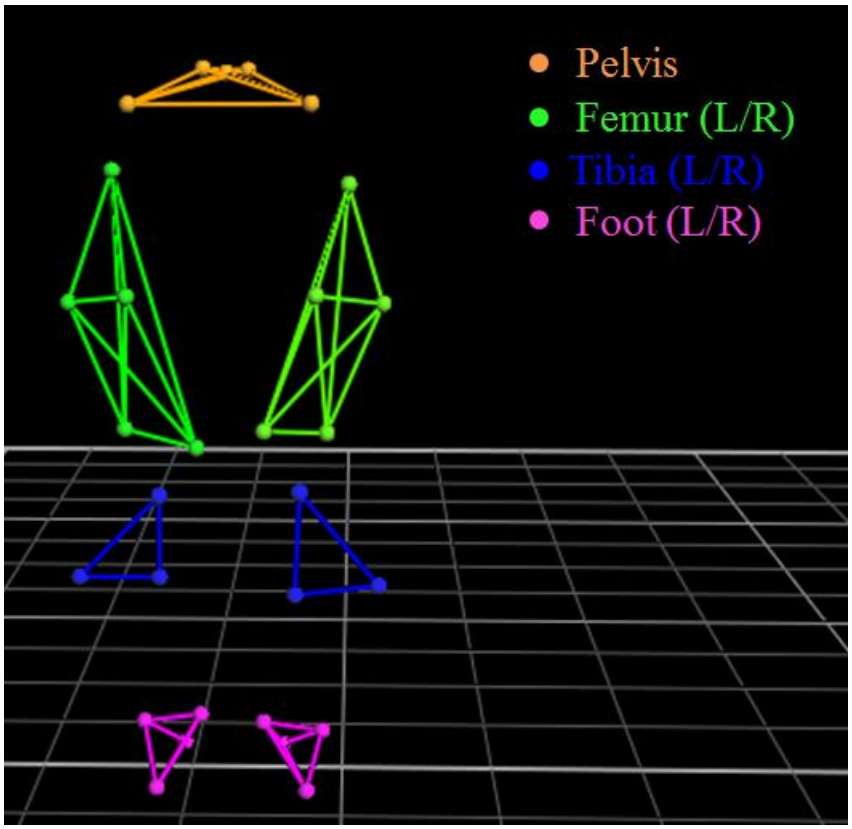

Figure 6.9: *Lower limb body segments split from motion analysis data points.*

$$((x_1, y_1, z_1), (x_2, y_2, z_2), ..., (x_i, y_i, z_i), ..., (x_k, y_k, z_k))$$

and the point set of the second body segment is denoted as

$$((u_1, v_1, w_1), (u_2, v_2, w_2), ..., (u_i, v_i, w_i), ..., (u_k, v_k, w_k))$$

. Before shape comparison, these two point sets are superimposed by translation, rotation and uniform scaling as follows.

All the point sets of the body segment are translated to the centroid of itself by subtracting the mean of all the landmarks, which means the ith point (bony landmark) (x_i, y_i, z_i) is translated to $(x_i - \overline{x}, y_i - \overline{y}, z_i - \overline{z})$, where $\overline{x} = \frac{x_1+x_2+...+x_i+...+x_k}{k}$, $\overline{y} = \frac{y_1+y_2+...+y_i+...+y_k}{k}$ and $\overline{z} = \frac{z_1+z_2+...+z_i+...+z_k}{k}$. Similarly, the scale of the point set is normalised by dividing by the root mean square $s = \sqrt{\frac{\sum_{i=1}^{k}(x_i-\overline{x})^2+(y_i-\overline{y})^2+(z_i-\overline{z})^2}{k}}$, which means the ith point (x_i, y_i, z_i) is scaled to $(\frac{x_i-\overline{x}}{s}, \frac{y_i-\overline{y}}{s}, \frac{z_i-\overline{z}}{s})$. The rotation normalisation is non-trivial as there is no standard reference orientation. Thus, the point set

$$((x_1, y_1, z_1), (x_2, y_2, z_2), ..., (x_i, y_i, z_i), ..., (x_k, y_k, z_k))$$

is set as the reference orientation. The point set

$$((u_1, v_1, w_1), (u_2, v_2, w_2), ..., (u_i, v_i, w_i), ..., (u_k, v_k, w_k))$$

is then rotated around the origin. The angles of rotation α, β and γ around x, y and z axes respectively are optimized by minimising the sum of the squared distances between the corresponding points. The two body segments are translated, scaled and rotated for shape comparison as in Figure 6.10.

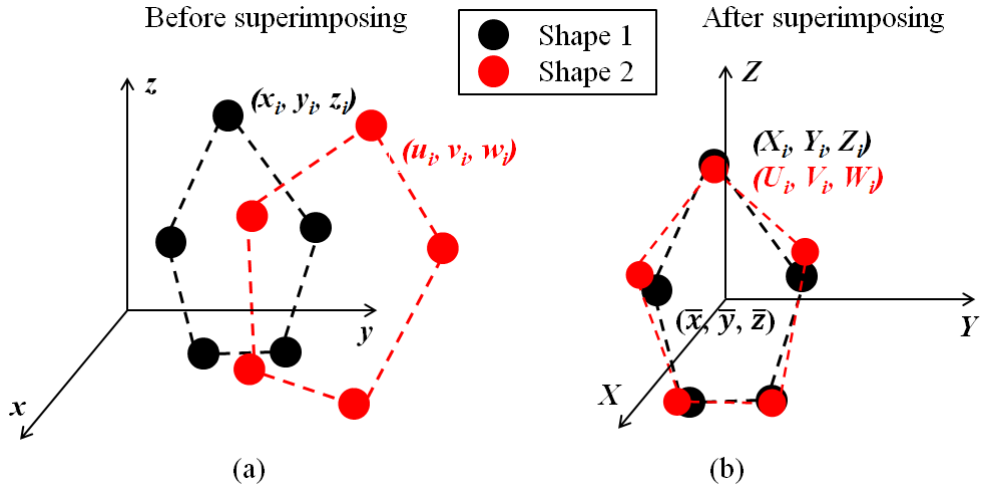

Figure 6.10: *Two shapes a) before and b) after superimposing.*

The two superimposed point sets are denoted by

$$((X_1, Y_1, Z_1), (X_2, Y_2, Z_2), ..., (X_i, Y_i, Z_i), ..., (X_k, Y_k, Z_k))$$

and

$$((U_1, V_1, W_1), (U_2, V_2, W_2), ..., (U_i, V_i, W_i), ..., (U_k, V_k, W_k))$$

respectively.

After superimposing the two point sets, the difference in their shapes is evaluated by calculating the Procrustes distance, which is defined as the square root of the sum of the squared distances between corresponding normalised landmark locations as in Equation 6.2.

$$P = \sqrt{\sum_{i=1}^{k} (U_i - X_i)^2 + (V_i - Y_i)^2 + (W_i - Z_i)^2} \tag{6.2}$$

A smaller Procrustes distance P indicates that the two body segments are more similar in shape. The Procrustes distance is invariant to the scale of the shapes due to the normalisation process.

6.1.2.1 Measurement of the repeatability of the examination

To quantify the repeatability of the examination, the shape difference between lower limb body segments over three repetitions of the examination was quantified with the Procrustes distance and the sum of Euclidean distance between corresponding bony landmarks at the standing pose and four different gait poses. These distances were calculated between each pairwise combination of these three examinations and a summary of the calculated distances is shown in Table 6.3. As only the left hip joint of the volunteer was examined, the right lower limb body segments are not listed in Table 6.3. However, the results of the shape similarity measurement on right leg were very similar to the results on the left leg.

In this research, two shapes with a Procrustes distance value higher than 0.5 were considered as significantly dissimilar. From Table 6.3, it is shown that the all the lower limb segments over three repetitions are similar, which indicates that the examination at different poses is repeatable. However, it can be seen that the largest dissimilarity of the lower limb segments over three examinations is at heel strike followed by toe off, mid

Body pose	Body segment	Procrustes distance	Sum of Euclidean distance (mm)
Standing pose	Pelvis	0.07 ± 0.03	10.21 ± 5.54
	Left femur	0.07 ± 0.02	16.78 ± 7.72
	Left tibia	0.02 ± 0.01	4.89 ± 1.57
	Left foot	0.01 ± 0.01	0.66 ± 0.21
Heel strike	Pelvis	0.08 ± 0.03	13.32 ± 7.34
	Left femur	0.07 ± 0.03	17.23 ± 7.92
	Left tibia	0.03 ± 0.01	4.99 ± 1.78
	Left foot	0.01 ± 0.01	0.68 ± 0.23
Mid stance	Pelvis	0.07 ± 0.03	9.81 ± 5.43
	Left femur	0.07 ± 0.03	16.48 ± 7.47
	Left tibia	0.02 ± 0.01	5.23 ± 1.83
	Left foot	0.01 ± 0.01	0.65 ± 0.18
Toe off	Pelvis	0.08 ± 0.04	12.71 ± 6.88
	Left femur	0.07 ± 0.03	17.16 ± 7.86
	Left tibia	0.03 ± 0.01	4.93 ± 1.64
	Left foot	0.01 ± 0.01	0.66 ± 0.22
Mid swing	Pelvis	0.08 ± 0.04	14.26 ± 4.93
	Left femur	0.07 ± 0.02	16.78 ± 7.72
	Left tibia	0.02 ± 0.01	4.94 ± 1.79
	Left foot	0.01 ± 0.01	0.67 ± 0.21

Table 6.3: *Shape comparison between lower limb segments between three examinations including Procrustes distance and the sum of Euclidean distance at each of standing pose and four gait poses.*

swing, mid stance and standing pose in descending order. Moreover, the femur deformed more than other lower limb segments at any pose over three examinations. This is because the femur contains more soft tissues, i.e. fat and muscle, under skin than other lower limb segments which leads to a bigger error caused by soft tissue artefact [67].

As the femur suffers from the most severe soft tissue artefact and it is used for hip joint kinematics description, the shapes of the femur modelled by the motion analysis (MA) system alone and the CAT & MAUS system are compared in Subsection 6.1.2.2.

6.1.2.2 Quantification of the femur segment deformation during movements

As the MA system suffers from soft tissue artefact, the shape of the body segment measured by MA deforms during movements. The shape deformation of femur segments measured by each of MA alone and CAT & MAUS at the standing pose and other gait poses was compared to prove CAT & MAUS reduces the error caused by soft tissue artefact. As described in Section 6.1.1, the left greater trochanter was captured by MA alone or CAT & MAUS while other bony landmarks were captured by just the MA system. Figure 6.11 illustrates the shape difference between the femur segment captured by MA alone and CAT & MAUS at the standing pose.

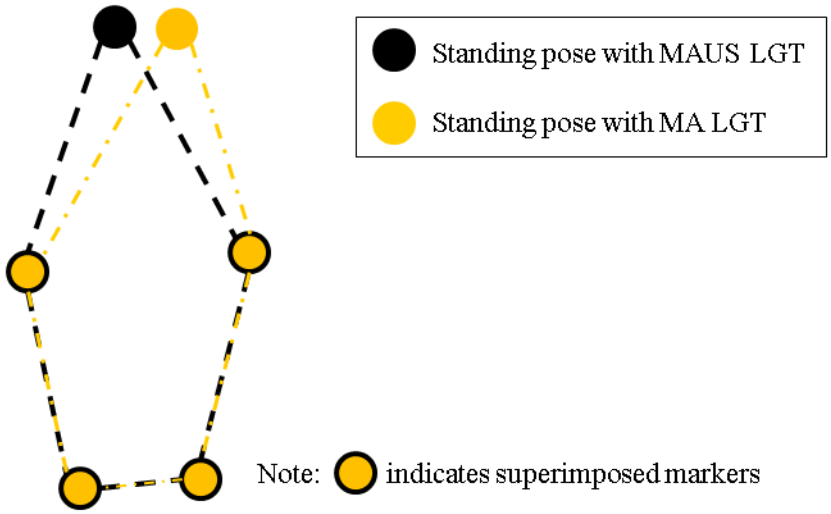

Figure 6.11: *An illustration of the difference between the femur segments modelled by MA alone and CAT & MAUS at the standing pose.*

The shape of the femur segment captured by MA alone and CAT & MAUS at one example gait pose of those four gait poses is compared in Figure 6.12. As the skin-based retro-reflective markers shifted away from their original position during movements, the marker on the LGT captured by MA alone did not present the actual underlying LGT while the ultrasound of CAT & MAUS captured the actual underlying LGT.

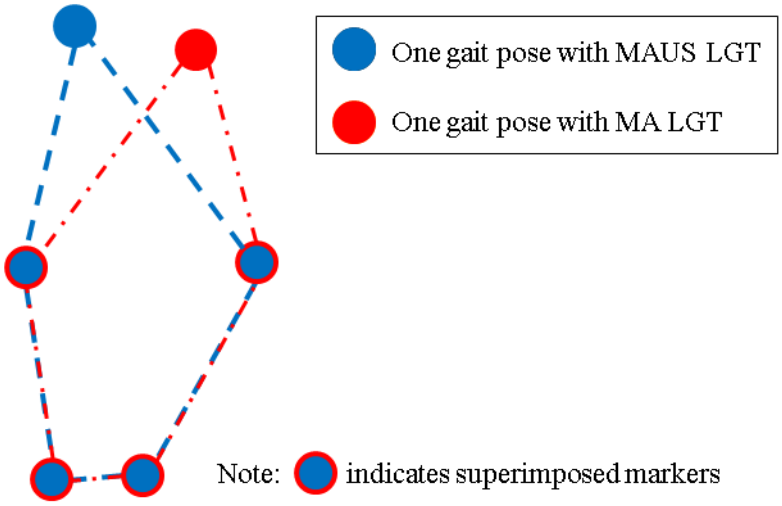

Figure 6.12: *An illustration of the comparison between the femur segments modelled by each of MA alone and CAT & MAUS at one example gait pose.*

To explain the soft tissue artefact, the femurs modelled by each of MA alone and CAT & MAUS at two different poses are compared in Figure 6.13. As ultrasound of the CAT & MAUS system captures the actual underlying LGT, the LGT detected at the standing pose and the other gait pose was expected to be the same which is the black and blue coincident point in Figure 6.13. As only the LGT was captured using both techniques (MA alone and CAT & MAUS), the other four markers attached on the femur should be the same during the examinations using each of motion analysis alone and CAT & MAUS at one pose because of the measurement repeatability, which are shown as the yellow and black coincident points at the standing pose and the red and blue coincident points at one gait pose. However, these four femur markers were shifted because of soft tissue artefact when the volunteer changed the pose from one pose to another.

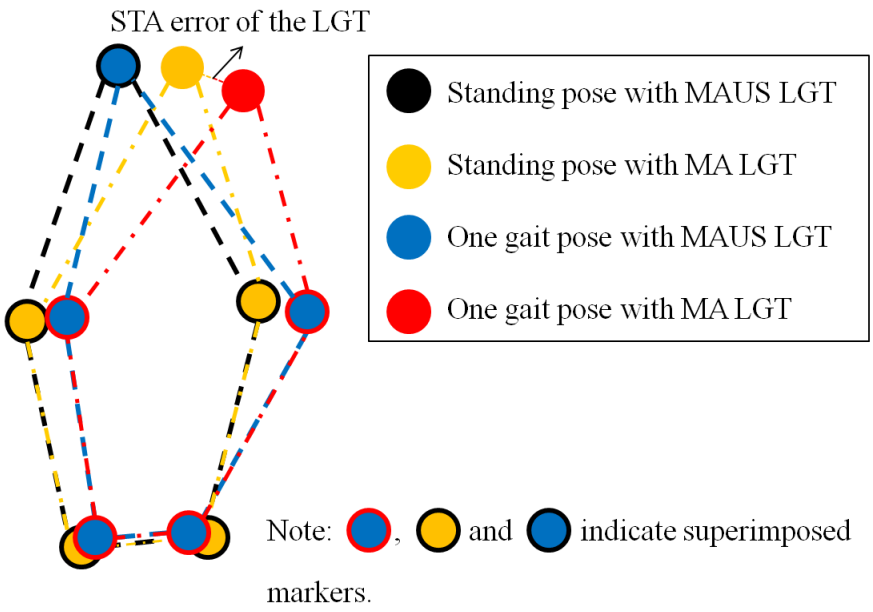

Figure 6.13: *An illustration of the comparison between the femur segments modelled by each of MA alone and CAT & MAUS at the standing pose and one example gait pose.*

The Procrustes distances between the femur shapes modelled by MA alone and CAT & MAUS at four gait poses compared to the femur shapes modelled by MA alone and CAT & MAUS at the standing pose were calculated respectively and they are listed in Table 6.4.

Body pose	CAT & MAUS	MA Alone
Heel strike	0.46 ± 0.09	0.74 ± 0.12
Mid stance	0.12 ± 0.08	0.35 ± 0.13
Toe off	0.41 ± 0.09	0.69 ± 0.13
Mid swing	0.38 ± 0.10	0.69 ± 0.14

Table 6.4: *Procrustes distance between the femurs modelled by MA alone and CAT & MAUS at four gait poses compared to the femurs modelled by MA alone and CAT & MAUS at the standing pose.*

As mentioned above, a greater Procrustes distance indicates a greater dissimilarity between two femur shapes, meaning the more the femur shape deformed. It can be seen that the Procrustes distance between the femur shapes modelled by CAT & MAUS at any gait pose and at the standing pose was smaller than the Procrustes distance between

the femur shapes modelled by MA alone at any gait pose and at the standing pose. In the other words, the femur shape modelled by CAT & MAUS was less deformed than the femur shape modelled by MA alone because the MA femur shape was affected by more soft tissue artefact. Moreover, the bigger movement the volunteer performed, the bigger deformation of the femur shape was associated with the soft tissue artefact. In the gait experiments, the heel strike was the biggest movement which led to the biggest femur shape deformation with Procrustes distances of 0.46 and 0.74 compared to the femur shape modelled by CAT & MAUS and MA alone respectively at standing position. Also, according to the Procrustes distance threshold of 0.5 (defined as a significant deformation happened), the femur shape from the MA system alone at the gait poses were considered significantly dissimilar from the shape captured at the standing pose. In the second column of Table 6.4, the CAT & MAUS system effectively reduced the dissimilarity between femur shapes modelled at different poses as real LGT was detected instead of a marker-based LGT, and thus the deformation associated with soft tissue artefact was avoided.

6.2 Adapted International Society of Biomechanics recommended hip joint kinematics description

The International Society of Biomechanics (ISB) has suggested a definition of a local joint coordinate system for hip joint kinematics calculation [141]. In this study, the ISB protocol has been followed with a minor adaptation of the femoral coordinate system to define hip joint kinematics. To quantify hip joint kinematics during movements, the local coordinate systems of lower limb bone structures have to been defined firstly. The bony landmarks used to define the local coordinate system of lower limb segments have been listed in Table 6.2 for reference.

6.2.1 Local lower limb bone structure coordinate systems definition

As the hip joint is a spheroidal (ball in socket) joint articulating the pelvis and femur, the local coordinate systems of pelvis and femur need to be defined and related to calculate hip joint kinematics. Refer to Figure 6.14 for a visual representation of the local coordinate systems of the pelvis and femur.

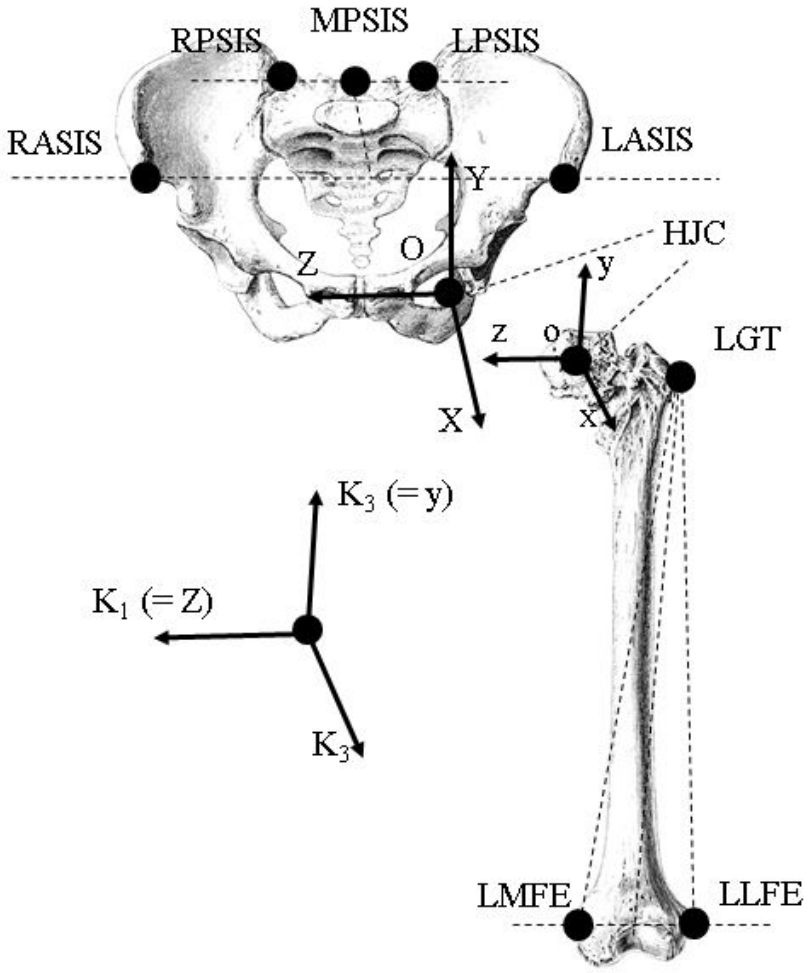

Figure 6.14: *Left hip joint coordinate systems, pelvic coordinate system (X,Y,Z) and adapted femoral coordinate system (x,y,z), and the kinematics description.*

- **Pelvic coordinate system (PCS) -** (X,Y,Z)

  In the local pelvic coordinate system, the left hip joint centre (HJC) is defined as the origin of the pelvic coordinate system (PCS). The HJC is estimated by the VICON Nexus 2.2.2 package (*VICON, Oxford, UK*) based on markers attached on the pelvis and the femur. The Z axis is parallel to the line pointing from the left anterior superior iliac spine (LASIS) to the right anterior superior iliac spine (RASIS) (Fig.6.14). The X axis of the PCS is parallel to the line lying in the plane defined by the LASIS, the RASIS and the mid posterior superior iliac spine (MPSIS), pointing anteriorly from MPSIS and orthogonal to the Z axis. The Y axis of the PCS is perpendicular to both the X axis and the Z axis, pointing superiorly.

- **Femoral coordinate system (FCS) -** (x,y,z)

  In the local femoral coordinate system, the origin of the femoral coordinate system (FCS) is coincident with the origin of the PCS, which is the HJC. The ISB recommends that the y axis of the FCS is defined as the line joining the midpoint between the left lateral femoral epicondyle (LLFE) and the left medial femoral epicondyle (LMFE), and the HJC, pointing superiorly [141]. As the HJC in this study is an estimated landmark based on the physical parameters of the subject, it varies between different individuals. The uncertainty of the estimated HJC introduces errors. Thus, we redefine the y axis as parallel to the line pointing from the midpoint between the LLFE and the LMFE to the LGT, pointing superiorly. The z axis of the FCS is orthogonal to the y axis and parallel to the line pointing from the LFE to the MFE. The x axis of the FCS is perpendicular to both the y axis and the z axis pointing anteriorly.

6.2.2 Hip joint kinematics (rotations) description

After locating the LGT from the registration result between two US surfaces at two different poses, hip joint kinematics can be quantified using the actual underlying LGT position in combination with other skin markers on the pelvis and femur. As the hip joint is a spheroidal joint, it rotates with three degrees of freedom during activities. Thus, hip joint kinematics can be described as hip joint rotations in the sagittal plane, the transverse plan and the coronal plane around the K_1, K_2, K_3 axes respectively. These joint rotations were described in the coordinate system (K_1, K_2, K_3) below.

- **Flexion/extension**

  The K_1 axis is parallel to the Z axis of the pelvic coordinate system. The rotation angle around the K_1 axis is termed the flexion/extension angle, which is the rotation in the sagittal plane.

- **Internal/external rotation**

  The K_2 axis is parallel to the y axis of the femoral coordinate system. The rotation angle around the K_2 axis is termed the internal/external rotation angle, which is the rotation in the transverse plane.

- **Adduction/abduction**

  The floating K_3 axis is perpendicular to the K_1 axis and the K_2 axis. The rotation angle around the K_3 axis is terned the adduction/abduction angle, which is the rotation in the coronal plane.

hip joint kinematics were then calculated using each of the MA data and CAT & MAUS data.

6.3 Results

6.3.1 CAT & MAUS GT and MA GT comparison

In the *in-vivo* experiments, the location of the LGT captured by CAT & MAUS and the MA system alone at different poses was compared in Table 6.5. It was shown that the average Euclidean distance with its variation between the CAT & MAUS GT and the MA GT over ten volunteers changed when the volunteer performed different poses. This is because skin-attached retro-reflective markers shifted away from the original location when the change of body pose takes place due to non-rigid structures in the musculoskeletal system such as skin, fat and muscles, sliding, stretching and compressing relative to the bone, which may cause an error of up to 50 mm [1]. The biggest average Euclidean distance difference compared to the average Euclidean distance at the standing pose happened at the heel strike pose, which was 22.84 mm.

Body pose	Euclidean distance (mm)
Standing pose	24.68 ± 4.87
Heel strike	47.52 ± 4.34
Mid stance	27.36 ± 3.82
Toe off	39.54 ± 4.20
Mid swing	41.84 ± 4.12

Table 6.5: *Euclidean distance between the CAT & MAUS GT and the MA GT at the standing pose and four different gait poses.*

A visual example of bony landmarks and probe markers in 3D space is shown in Figure 6.15 to present the difference between the MA GT and the CAT & MAUS GT at heel strike pose. It was obvious that the position of MA GT is different from the position of CAT & MAUS GT because the MA GT was based on a skin marker which could not measure the actual position of the underlying GT.

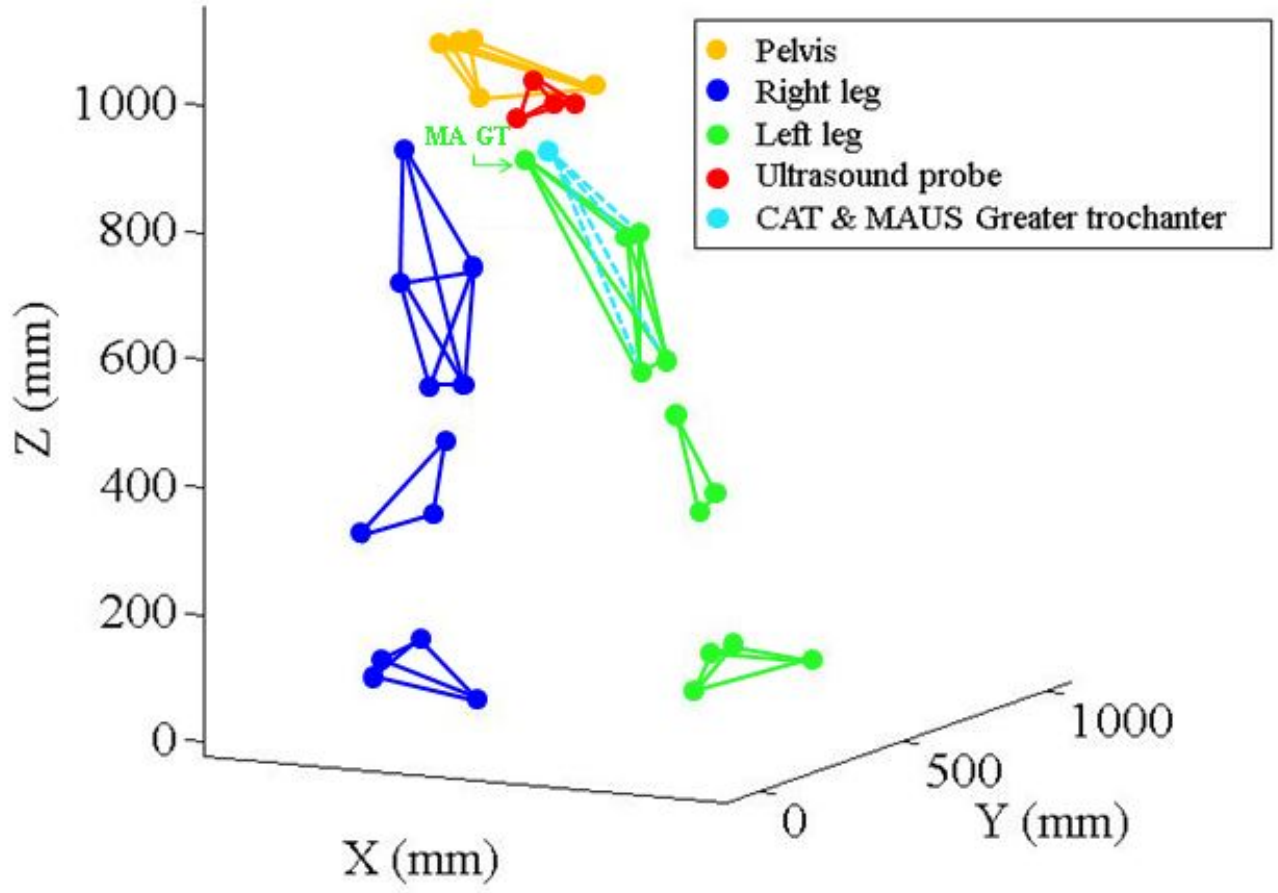

Figure 6.15: *Difference between the GT captured by MA alone and the GT captured by CAT & MAUS at heel strike pose.*

A three dimensional model of the hip joint at heel strike pose compared to standing pose is shown in Figure 6.16 to indicate the error caused by soft tissue artefact. The MA GT and the CAT & MAUS GT at the standing pose were aligned to get rid of the error introduced by soft tissues under the skin. After the same alignment was applied to the MA GT and the CAT & MAUS GT at any one gait pose, it was expected that the MA GT would align as well to the CAT & MAUS GT as at the standing pose. However, the two GTs were not aligned but located at different positions because the relative position of the MA GT compared to CAT & MAUS GT was changed due to the soft tissue artefact, which would introduce a significant error for later joint kinematics description if using only MA data.

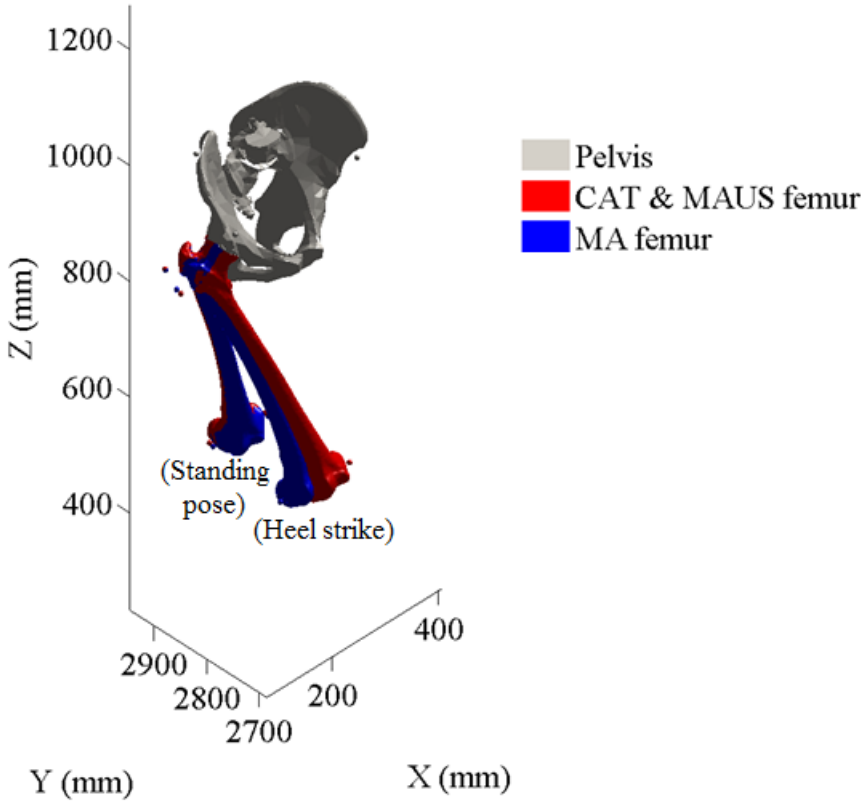

Figure 6.16: *Three dimensional visualization of hip joint at heel strike pose compared to standing pose to indicate the error caused by soft tissue artefact.*

6.3.2 Hip joint kinematics description

To quantify hip joint kinematics during gait using CAT & MAUS, the flexion/extension, adduction/abduction and internal/external rotation angles of the hip joint between standing pose and the other four gait poses were calculated with the CAT & MAUS LGT for the ten volunteers (Figure 6.17). Because of the different individual stride lengths, which varied between a minimum of 68 cm and a maximum of 83 cm, the mean flexion/extension angles of each of the four gait poses varied from $-14.98°$ (toe off) to $32.57°$ (heel strike) with an average standard deviation of $4.19°$, the mean adduction/abduction angles of each of the four gait poses varied from $-2.18°$ (toe off) to $2.92°$ (heel strike) with an average standard deviation of $0.93°$ and the mean internal/external rotation angles of each of the four gait poses varied from $-2.16°$ (heel strike) to $4.77°$ (toe off) with an average standard deviation of $1.33°$.

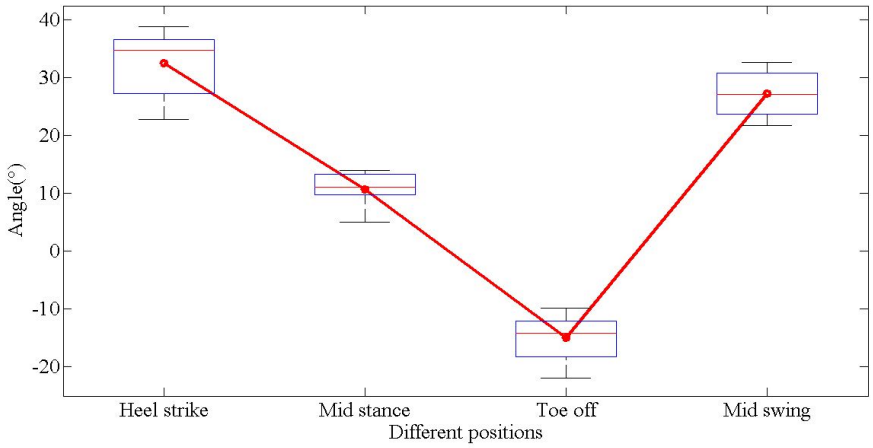

(a)

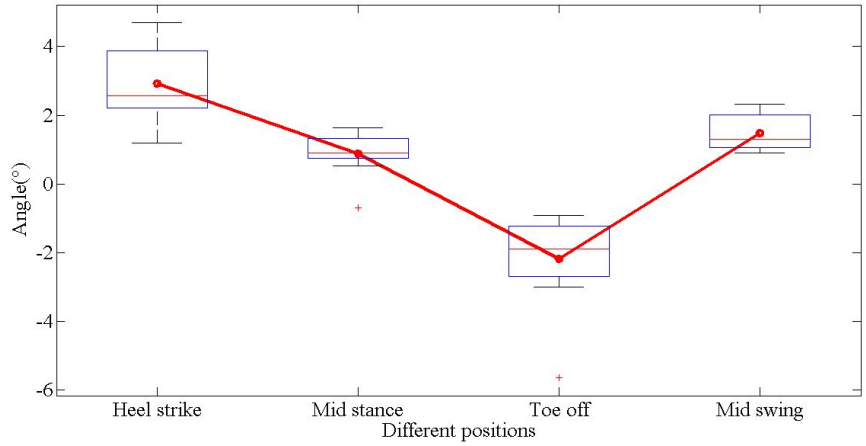

(b)

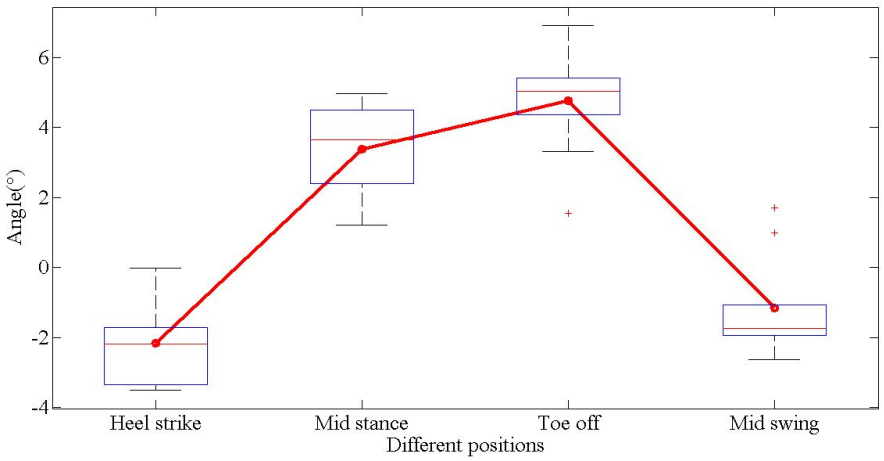

(c)

Figure 6.17: *Quantification of hip joint rotation angles using the CAT & MAUS system, a) flexion/extension, b) adduction/abduction and c) internal/external rotation.*

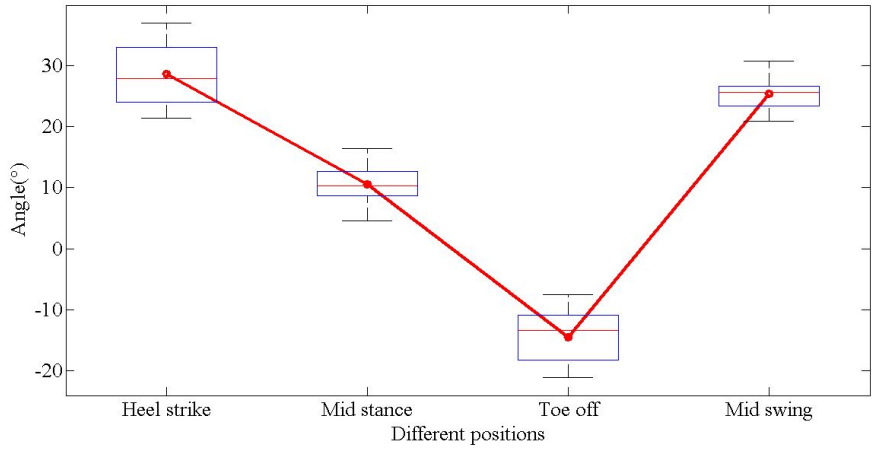

(a)

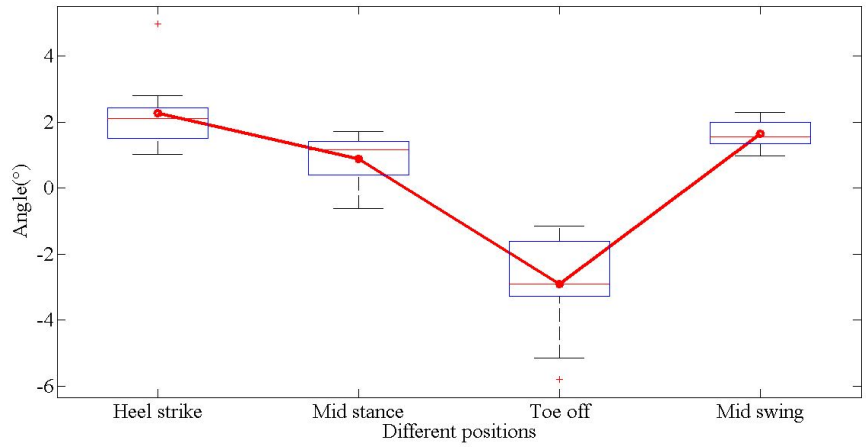

(b)

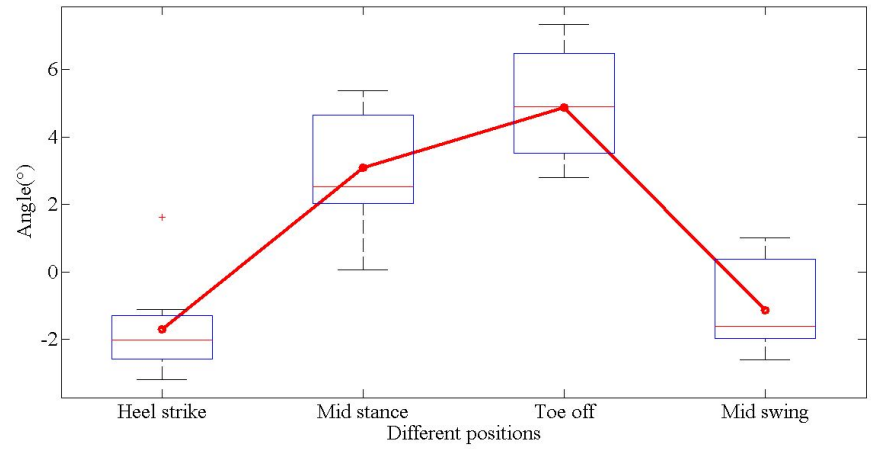

(c)

Figure 6.18: *Quantification of hip joint rotation angles using the motion analysis system alone (i.e. without US), a) flexion/extension, b) adduction/abduction and c) internal/external rotation.*

The quantification of hip joint rotation angles with the MA LGT (Figure 6.18) gives a similar trend to the CAT & MAUS measurement of hip joint rotations (Figure 6.17). Like hip joint kinematics quantification using CAT & MAUS, because of the different individual stride length, the mean flexion/extension angles of each of the four gait poses varied from $-14.44°$ (toe off) to $28.54°$ (heel strike) with an average standard deviation of $4.12°$, the mean adduction/abduction angles of each of the four gait poses varied from $-2.92°$ (toe off) to $2.27°$ (heel strike) with an average standard deviation of $0.96°$ and the mean internal/external rotation angles of each of the four gait poses varied from $-1.70°$ (heel strike) to $4.89°$ (toe off) with an average standard deviation of $1.50°$.

Since hip joint kinematics were decomposed into three clinically relevant rotation parameters (flexion/extension, adduction/abduction and internal/external rotation), rotations in each plane measured by CAT & MAUS and MA alone were compared. The adduction/abduction and the internal/external rotations are relatively small compared to the flexion/extension i.e. the rotation of the limb in the sagittal plane. Comparing the results from CAT & MAUS to the results from the MA alone, they are similar in the adduction/abduction and the internal/external rotation with maximum deviations of $0.74°$ and $0.36°$ respectively. However, the CAT & MAUS flexion/extension had a bigger rotation range than the MA flexion/extension by up to $6°$ because the skin-attached marker shifted away from the underlying bony landmark. This means that movement detected using the MA system alone was smaller than the actual movement of underlying bony landmark detected using CAT & MAUS. Therefore, the flexion/extension measured using MA alone was affected by STA and the CAT & MAUS system provided more accurate information about the position of the limb.

As all the volunteers were healthy and without any hip joint injury or operation, Figure 6.17 provides a motion trend of hip joint rotations of a healthy subject during gait. As expected, the motion trend in Figure 6.17 resembles the trend presented in [113]. Specifically, the hip joint rotations measured with the CAT & MAUS system are similar to the results modelled by an Euler model reported in [113] with a maximum error of $4°$

because of the different stride length.

Moreover, in practice, the CAT & MAUS system was shown to significantly reduce the data acquisition time relative to previous MAUS [89] on one subject from approximately 30 minutes to 3-5 minutes.

6.4 Conclusions

In this chapter, quantitative analysis of healthy hip joint kinematics during gait has been presented. The shape of a volunteer's body segments has been analysed using Procrustes analysis. It has been shown that there was no significant difference of the shape over different trials at the same pose, which showed the repeatability of the CAT & MAUS system. Moreover, it has been proven that the shape modelled by CAT & MAUS was less deformed than the shape modelled by the MA system alone during movements.

The results from the CAT & MAUS system have been compared to the results from the MA system alone. Although the general hip joint rotation trend of the CAT & MAUS results and the MA results was similar, the CAT & MAUS results had a larger range than the MA results especially for the hip joint flexion/extention. Since the insufficient representation of the underlying bony landmark using a skin-based marker would lead to an imprecise hip joint rotation calculation, an accurate rotation angle measured by CAT & MAUS leads a more reliable quantitative analysis of hip joint kinematics during gait.

As the CAT & MAUS system detects the actual underlying bony landmarks, which significantly reduces the error caused by soft tissue artefact, the results from CAT & MAUS can be used as the ground truth for other similar research of joint kinematics modelling. Moreover, from the CAT & MAUS results of the ten healthy volunteers in this research, a healthy hip joint kinematics model of gait could be built as a reference for future clinical condition comparison.

Chapter 7

Conclusions and Future Work

In this final chapter, the main contributions of this research are summarized, the current limitations are discussed, and potential opportunities for future work are suggested.

7.1 Contributions

The main contributions of this thesis are summarized as follows:

Framework for the hardware of the CAT & MAUS system with a novel calibration box design:

In Chapter 3, the hardware architecture, i.e. an augmented motion analysis with ultrasound (MAUS) system with the adapted three dimensional (3D) transformations, of the CAT & MAUS system was introduced. Because the US probe is tracked by the motion analysis (MA) system, the position of the image plane relative to the probe is known in 3D space. According to the tracked positional information of the US probe, the segmented bone structures are transformed into 3D space and reconstructed as a bone surface.

To efficiently synchronise the ultrasound (US) device and the motion analysis system, a multi-use calibration box has been designed. The spatial and temporal calibration of the CAT & MAUS system have been validated using a proximal femur phantom. A patch-based tracking algorithm has been developed to assist the validation of the CAT & MAUS system calibration. The average Euclidean distance error of the spatial calibration over five trials is 0.34 mm, which is within the clinical tolerance of computer-aided orthopaedics surgery ($\pm 1mm$) [21]. The maximum temporal error of the temporal calibration is $\frac{T_{MA}}{2}$ where T_{MA} is the time duration between two adjacent frames of the motion analysis system.

The augmented MAUS system is not only non-ionising but also detects the actual underlying bone landmarks more flexibly, which can describe a wider range of joint motion than conventional CT or MRI scanners. In particular, the developed system overcomes the drawback of the previous MAUS system [89] with which the target bony landmark at different poses had to be located by eye every time. Measurement using the previous

MAUS system was laborious, time consuming and less accurate. With the augmented MAUS system, the data acquisition time for one trial of one subject has been significantly reduced from around 30 minutes to approximately 3 minutes (Chapter 6).

The developed CAT & MAUS system has been used to collect gait data in the Oxford Gait Laboratory, Nuffield Hospital, Oxford.

Computer-aided post-processing pipeline to automate the MAUS system:

In order to automatically process the data obtained using a MAUS system, the computer-aided post-processing pipeline was introduced in Chapter 4 and 5.

A 3D globally optimal surface-to-surface registration was employed to accurately match the same bony landmark in data from two gait positions (Chapter 4). The globally optimal surface-to-surface registration integrated the branch-and-bound search algorithm with the iterative closest point (ICP) registration technique, which effectively solved the issue of getting trapped in local minima of the cost function – a key drawback of conventional ICP registration. The target bony landmark can be transformed from the reference position to any position accurately with an average rotation error of 0.38° and an average translation error of 0.33 mm, both of which are within the clinical tolerance of computer-aided orthopaedics surgery.

The 3D surfaces in the registration were previously reconstructed from the manual segmentation over thousands of ultrasound frames. However, manual segmentation is extremely laborious and time consuming. To tackle this problem, an automatic bone segmentation in US images has been developed as a precursor to the 3D registration step to make the system more time efficient (Chapter 5). The automatic segmentation achieved an accuracy of 0.13 mm and a sensitivity of 57.92%. Both registration and segmentation algorithms were validated using the proximal femur phantom before being used *in-vivo*.

***In-vivo* study: comparison between the results from each of the CAT & MAUS system and the MA system alone, an indication of the spatial measurement error of the MA system caused by soft tissue artefact:**

In Chapter 6, the *in-vivo* hip joint kinematics, i.e. the hip joint rotations, were quantified based on an adapted hip joint kinematics definition from the International Society of Biomechanics. The results from CAT & MAUS have been compared with the results from the motion analysis (MA) system alone. Since the trajectories of target bony landmark tracked by the CAT & MAUS system and the MA system alone were different, the average Euclidean distances at different poses varied from 24.68 mm to 47.52 mm. This indicated the spatial measurement error of the MA system caused by soft tissue artefact. This is because the target bony landmark detected by the CAT & MAUS system was identical while the MA marker measured bony landmark shifted away from the original position during pose change due to soft tissue sliding or compressing. It has also been reported that the CAT & MAUS results presented a greater motion range that the MA results. The maximum rotation angle difference can be up to 4.03° in the sagittal plane. Moreover, the deformation of the femur shape at different poses caused by soft tissue artefact has been investigated using Procrustes analysis. The Procrustes distances of the left femur segment with CAT & MAUS GT varied from 0.1232 to 0.4603 while the Procrustes distances of the left femur segment with MA GT varied from 0.3467 to 0.7380, which means that the CAT & MAUS measurement highly reduces the shape deformation than the marker-based measurement during movements.

All in all, a novel, non-ionising, automatic and accurate CAT & MAUS system has been developed in this thesis. As the CAT & MAUS system reveals the actual movement of the underlying bone landmarks compared to the MA system, the results from CAT & MAUS can be regarded as a reference to sensor based systems (for example, VICON motion capture system and GaitSmart system, etc.). Moreover, hip joint kinematics quantified using CAT & MAUS during gait over ten healthy volunteers can be potentially used as a healthy model for clinical comparison to patients with hip pathologies. However,

the number of volunteers involved in this research was limited, a larger number of healthy subjects with a wider variation of age, gender and body-build, etc., will contribute to a more accurate healthy hip joint kinematics model.

7.2 Future work

The potential directions of the future work in both technical and clinical perspectives are presented in this section for readers' interests.

7.2.1 Automatic segmentation on other bone structures

In Chapter 5, automatic segmentation was focused on segmenting the greater trochanter in US images as the aim of this thesis was to describe hip joint kinematics. The segmentation algorithm introduced in Chapter 5 was designed to segment a rigid-like bone structure in an ultrasound image where there are no other bone structures. However, the CAT & MAUS system is not just limited to measure hip joint movements. The system could be extended to monitor other joint movements. To reconstruct the 3D surface of the bone segments related to the joint of interest, the bone segmentation algorithms for different bone structures could be developed. For example, a blob segmentation algorithm could be used to segment the patella in US images. Refer to Figure 2.14 on Page 25 for an image example of the patella.

7.2.2 Dynamic measurement with more constrained movement protocol using the CAT & MAUS system

In the *in-vivo* test (Chapter 6), the complicated gait analysis was conducted using CAT & MAUS with the subject moving in a quasi-dynamic manner. Although all the poses that the volunteer performed strictly followed the gait phase definition [102] explained in Chapter 2, a quasi-dynamic gait lacks the reality and continuity of the actual dynamic gait. For example, the subject may move even though being asked to keep static, while

this problem is avoided during continuous walking. As the experiments using CAT & MAUS are not just restricted to gait, protocols of testing movements, i.e. poses, could be devised for future examination. For example, a hip joint rotation experiment has been conducted using CAT & MAUS as in Figure 7.1. This experiment showed the maximum

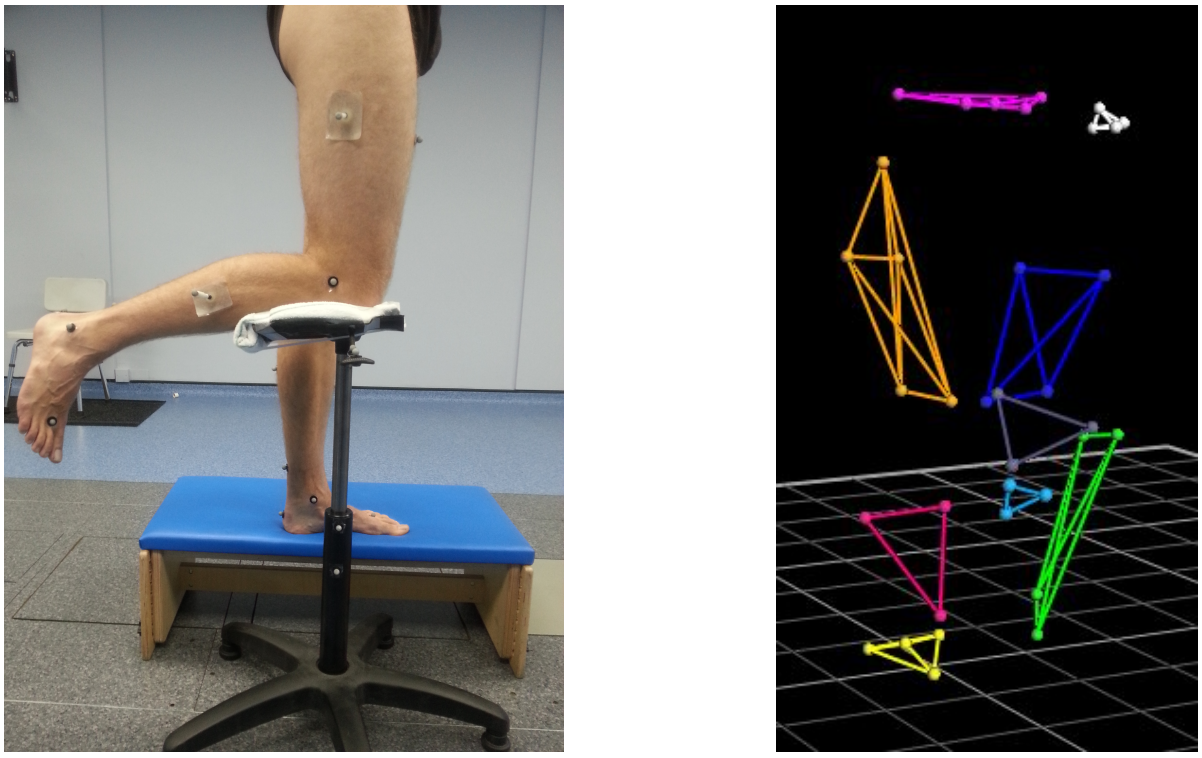

(a) **(b)**

Figure 7.1: *Hip joint rotation experiment, a) experiment pose, b) pose in motion analysis.*

rotation range of the hip joint adduction/abduction. Moreover, since this movement was constrained in one degree of freedom of a single joint (the hip joint), which is not as complicated as walking, the target bony structure could be tracked during the movement using the tracking algorithm introduced in Chapter 3. Thus, similar constrained motion experiments can be designed to dynamically measure joint movements and describe the joint functionality for other situations of interest.

7.2.3 Clinical analysis and decision making of musculoskeletal problems using CAT & MAUS

As the intention of this thesis is to develop a system for hip joint kinematics description during gait, the *in-vivo* tests were only conducted on healthy volunteers (Chapter 6). However, the CAT & MAUS system is not limited to measurement on healthy subjects. Hip joint kinematics of subjects with various hip joint pains could be monitored during movements as well. The results from subjects with hip joint pains could then be compared to the results from healthy volunteers to better understand hip joint pain from the kinematics perspective. Hip joint kinematics of subjects with a specific musculoskeletal problem could be regarded as one class. After hip join kinematics of subjects with hip joint pains are described, machine learning knowledge could be applied to build up a musculoskeletal condition classifier for clinical diagnosis. The CAT & MAUS results of a new subject could then be classified to support clinicians in diagnosing the hip joint disease.

Appendix A

List of Publications and Presentations

A.1 Publications

A.1.1 Journal papers

[1] R Jia, S Mellon, A P Monk, D W Murray, J A Noble. **A Computer-Aided Tracking and Motion Analysis with Ultrasound (CAT & MAUS) System for the Description of Hip Joint Kinematics**, *International Journal of Computer Assisted Radiology and Surgery*, 2016.

[2] R Jia, A P Monk, D W Murray, J A Noble, S Mellon. **CAT & MAUS: A Novel System for True Dynamic Motion Measurement of Underlying Bony Structures with Compensation for Soft Tissue Movement**, *Journal of Biomecanics*, 2016 (Invited paper).

A.1.2 Conference papers

[1] R Jia, A P Monk, D Murray, S Mellon, J A Noble. **Greater Trochanter Tracking In Ultrasound Imaging During Gait**, *International Symposium on Biomedical Imaging (ISBI)*, 2015.

[2] R Jia, S Mellon, A P Monk, D Murray, J A Noble. **Three Dimensional Freehand Ultrasound Reconstruction Using Hybrid Interpolation**, *Medical Image Understanding and Analysis (MIUA)*, 2015.

[3] R Jia, S Mellon, S Hansjee, A P Monk, D W Murray, J A Noble. **Automatic Bone Segmentation In Ultrasound Images Using Local Phase Features and Dynamic Programming**, *International Symposium on Biomedical Imaging (ISBI)*, 2016.

[4] R Jia, S Mellon, A P Monk, D W Murray, J A Noble. **Globally Optimal Registration for Describing Joint Kinematics**, *Medical Image Understanding and Analysis (MIUA)*, 2016.

[5] R Jia, S Mellon, S Hansjee, A P Monk, D W Murray, J A Noble. **CAT & MAUS: Elucidation of Hip Joint Kinematics in Gait and Comparison with Motion Analysis**, *BMVA: IET Human Motion Analysis for Healthcare Applications*, 2016.

A.2 Conference presentations

A.2.1 Oral presentations

[1] International Symposium on Biomedical Imaging (ISBI), NY, USA 2015.

[2] International Symposium on Biomedical Imaging (ISBI), Prague, CZ 2016.

[3] BMVA: IET Human Motion Analysis for Health-care Applications, London, UK 2016 (Filmed).

A.2.2 Poster presentations

[1] Medical Imaging Summer School (MISS), Sicily, Italy ,2014.

[2] Biomedical Imaging Festival, Oxford, UK, 2014.

[3] Medical Image Understanding and Analysis (MIUA), Lincoln, UK, 2015.

[4] Biomedical Imaging Festival, Oxford, UK, 2015.

[5] Invited Furlong Talk, ORUK, Royal Society of Medicine, London, UK, 2015.

[6] Medical Image Understanding and Analysis (MIUA), Loughborough, UK, 2016.

[7] Biomedical Imaging Festival, Oxford, UK, 2017.

Appendix B

Multi-use Calibration Box Design using SolidWorks

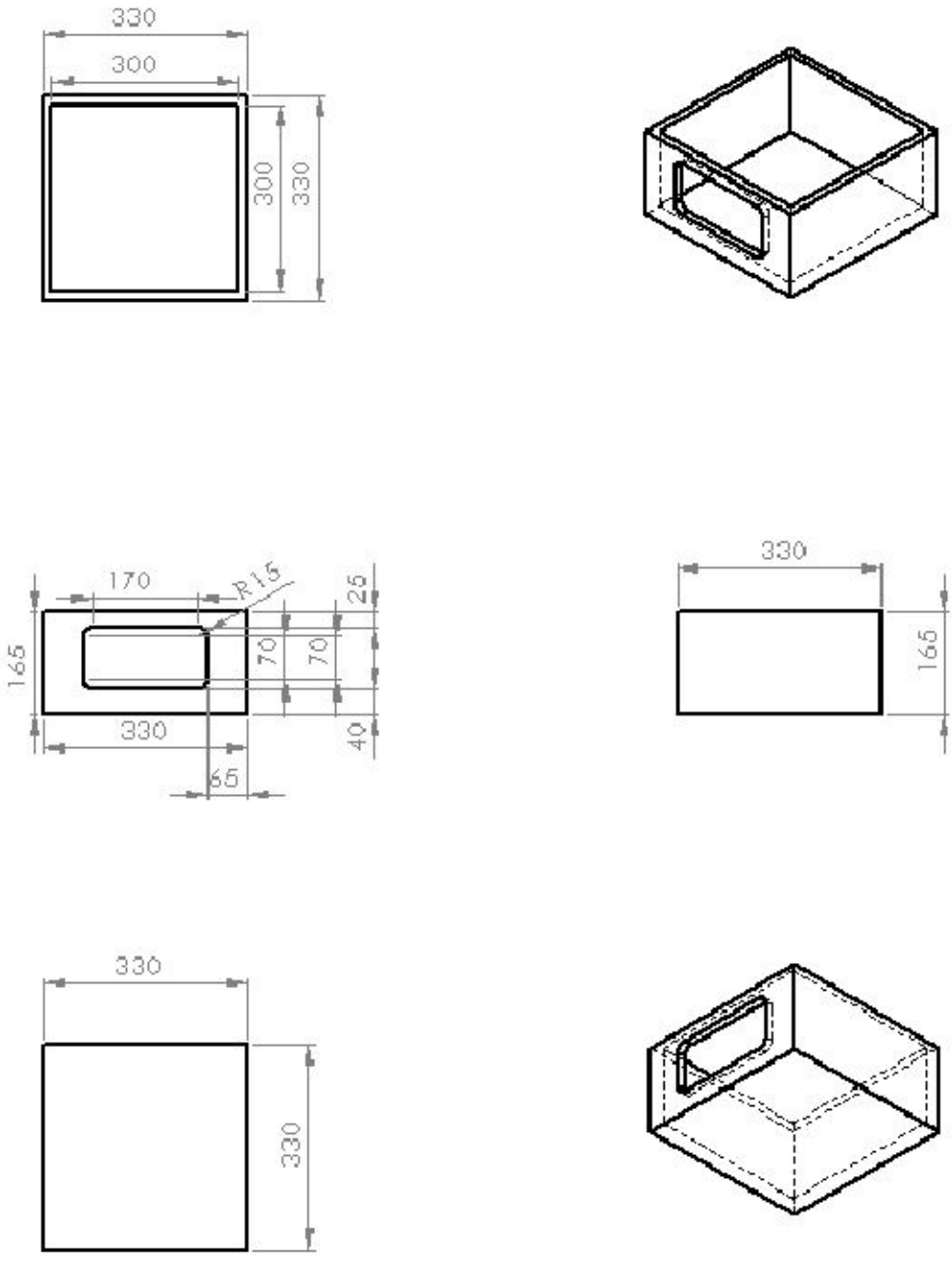

Figure B.1: *Solidworks design of calibration box with an open window in the front (Unit: mm).*

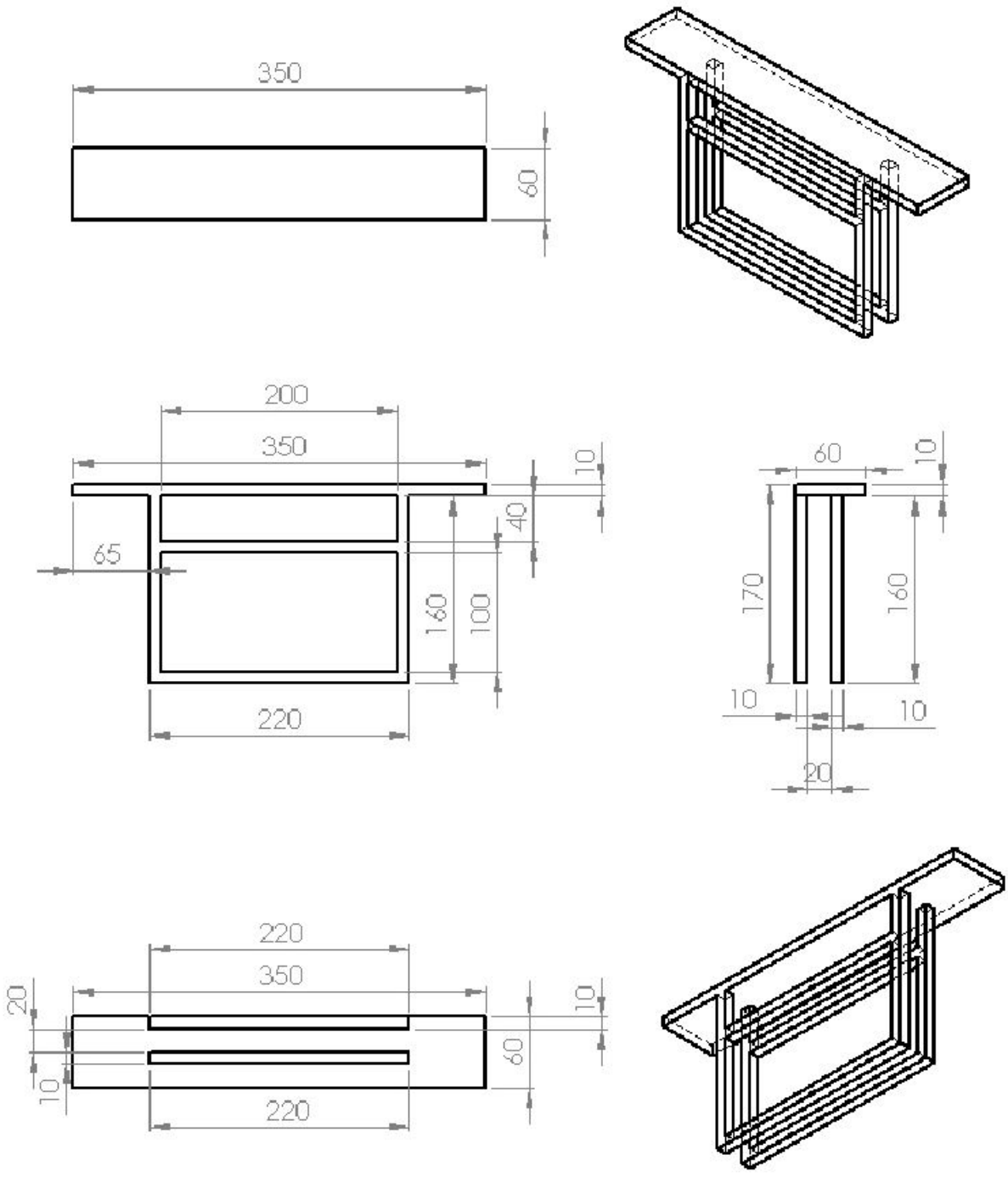

Figure B.2: *Solidworks design Dual frames of the calibration box (Unit: mm).*

Appendix C

Three Dimensional Freehand Ultrasound Reconstruction using Hybrid Interpolation

C.1 Introduction

In Chapter 3, an augmented motion analysis with ultrasound (MAUS) system was introduced. It shares common principle with three dimentional (3D) freehand ultrasound (US) imaging. The MAUS system tracks the position of a 2D US probe continuously in a 3D Euclidean coordinate frame. Based on the tracked position information of the US probe, the collected 2D US image slices can be transformed into 3D space. Since 3D surface-to-surface registration (Chapter 4) is employed to locate target bony landmarks, a reliable 3D reconstruction algorithm is essential to extract the object surface from the reconstructed 3D US volume for registration preparation. However, 2D US slices may not be transformed as a uniformly sampled set in 3D space and the resulting irregularity of the data points presents a major difficulty when reconstructing a smooth 3D volume. A good interpolation method should not only insert the most likely value in those gaps, but also avoid image and volume distortion.

The most commonly used methods for interpolation are pixel nearest neighbour (PNN), voxel nearest neighbour (VNN), distance weighted (DW) interpolation and radial basis function (RBF) interpolation [124]. PNN and VNN are more computationally efficient than DW and RBF to interpolate a given 3D volume, but they are susceptible to intensity discontinuities (Figure C.2b). Instead of considering the global volume, DW interpolation considers only a constrained local volume around each voxel. Thus some sparse data that are outside of the threshold region will be ignored [58]. RBF interpolation alone is only modelled within one pre-constraint region around the centre voxel, which ignores other relevant data points out of the constraint region [25].

This appendix introduces a more reliable interpolation method for 3D reconstruction as a precursor to future registration. The content of this appendix has been published in the Proceedings of *Medical Image Understanding and Analysis, 2015*.

C.2 Methods

C.2.1 Data acquisition

Six US sequences of a healthy male volunteer's greater trochanter were recorded using a LOGIQ S7 US device (*GE, USA*) while the volunteer was fixed at the left lateral decubitus to minimize body movement. The positions of the probe were captured by a VICON motion capture system (*Oxford, UK*) consisting of 16 infra-red cameras. For three trials, the probe was moved slowly to give approximately parallel slices (Figure C.1a). For the other three trials, the probe was moved in a "heel to toe" pivoting motion (Figure C.1b). An ML 6-15 transducer was triggered at 12MHz (90mm wave depth) for both scanning protocols. The frame rate of the US device was set by the user to 20 frames per second and the frame rate of the motion capture system was set to 100 frames per second.

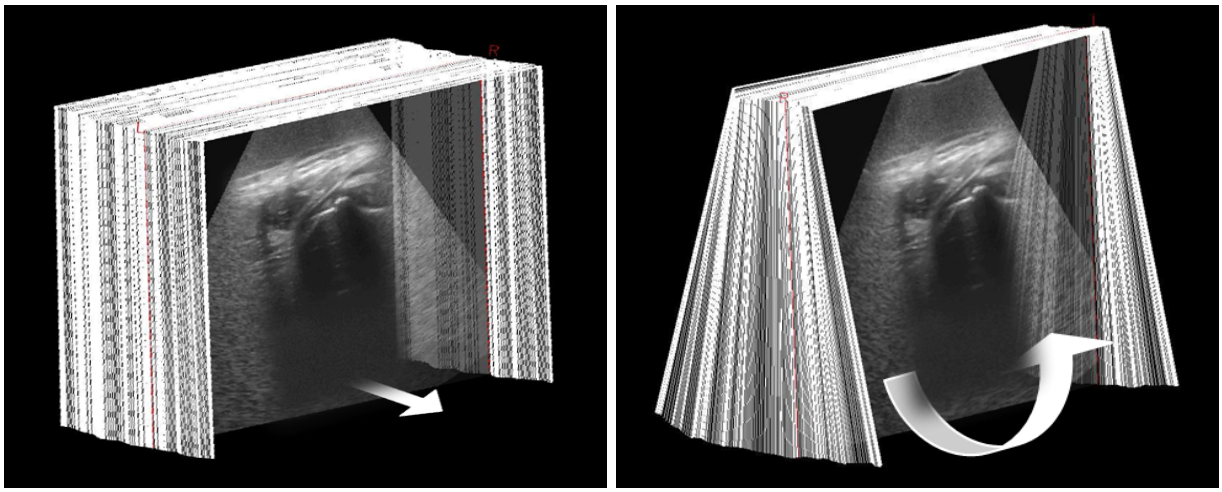

(a) **(b)**

Figure C.1: *US scanning, a) in parallel, and b) from heel to toe.*

C.2.2 Three dimensional volume reconstruction

Before transforming 2D US slices into 3D space, spatial and temporal calibration is required to determine the relationship between the US device and motion capture system.

Spatial calibration calculates the transformation parameters in the spatial domain, while temporal calibration synchronizes measurements from the two modalities. A detailed description of calibration procedures can be found in Chapter 3. After the calibration procedure, all slices of the US video can be transformed into the 3D global space. If one voxel has multiple non-zero values, the average value is assigned to this voxel.

After all the slices have been transformed into 3D global space, there are gaps within the reconstructed 3D volume (as shown in the cross-section in Figure C.2a). In order to fill these gaps, the relationship between one missing voxel with its K nearest neighbours (KNN) was found.

Firstly, the positions of all the non-zero voxels in the reconstructed volume are stored in a k dimensional (k-d) tree. A k-d tree is a binary tree in which the data are split into half iteratively by hyper-planes [66]. Each leaf node in the tree holds the position of one nonzero voxel.

The K nearest neighbours of every zero voxel in turn are found by querying the k-d tree. The Euclidean distances between the zero voxel and the K nearest neighbours are calculated as well. In this research, K was set to 10. As some zero voxels are not transformed from the pixels in the US image but the area outside the region of interest of the US image, a distance threshold was set to 10 voxels as either all the gaps or the thickness of similar tissue structures are smaller than 10 voxels. This means that distances from the zero voxel to the nearest neighbours that are greater than 10 voxels are unlikely to affect the interpolation of this missing voxel and are ignored.

After finding the K nearest neighbours, the zero voxel has to be assigned a representative value. The most efficient method would be to assign the value of the nearest neighbour or the average of these K searched voxels to the zero voxel, however, this may give rise to discontinuities (Figure C.2b). Radial basis function (RBF) interpolation can be applied to highly unstructured data [119]. Thus, a real-valued function $f(p)$, the intensity value in this research, is interpolated by $S(p)$ given the values $f(p_i) : i = 1 \dots n$, where $p_i : i = 1 \dots n$ is a set of distinct points in 3D space, i.e. the K nearest neighbours,

called interpolation nodes. The RBF interpolant for one missing voxel is calculated as Equation C.1:

$$S(p) = P_m(p) + \sum_{i=1}^{n} \lambda_i \phi(\|p - p_i\|) \tag{C.1}$$

where p_i is a set of the interpolation nodes whose positions and values are known. $\|\cdot\|$ denotes the Euclidean distance between p and p_i. $\phi(\cdot)$ is the basis function. λ_i is a set of weights, one for each interpolation node, which need to be determined. $P_m(\cdot)$ is the polynomial of degree m, the coefficients of which also need to be determined by solving a set of linear equations.

There are several choices for $\phi(\cdot)$ [119]. In our study, the commonly used Gaussian function was chosen as the basis function, as in Equation C.2.

$$\phi(\gamma) = e^{-\alpha\gamma^2} \tag{C.2}$$

where α is a constant parameter. It controls the tension of the interpolant. Thus, $\alpha = 1$ is used to avoid over-fitting the interpolant.

In order to reduce the computational time of interpolation in 3D space, the simplest first degree polynomial is used, which means $m = 1$. The interpolation conditions then become:

$$\begin{aligned}
\lambda_1\phi(\|p_1 - p_1\|) + \cdots + \lambda_n\phi(\|p_1 - p_n\|) + c_0 + c_1x_1 + c_2y_1 + c_3z_1 &= f(p_1) \\
\lambda_1\phi(\|p_2 - p_1\|) + \cdots + \lambda_n\phi(\|p_2 - p_n\|) + c_0 + c_1x_2 + c_2y_2 + c_3z_2 &= f(p_2) \\
&\vdots \\
\lambda_1\phi(\|p_n - p_1\|) + \cdots + \lambda_n\phi(\|p_n - p_n\|) + c_0 + c_1x_n + c_2y_n + c_3z_n &= f(p_n)
\end{aligned} \tag{C.3}$$

where c_t are the polynomial coefficients.

In order to give a unique set of coefficients, a side condition is also introduced as

$$\sum_{i=1}^{n} \lambda_i(c_0 + c_1x_i + c_2y_i + c_3z_i) = 0 \tag{C.4}$$

Then Equation C.3 and Equation C.4 can be combined together into a matrix of interpolation conditions:

$$\begin{bmatrix} \phi(\|p_1 - p_1\|) & \cdots & \phi(\|p_1 - p_n\|) & 1 & x_1 & y_1 & z_1 \\ \vdots & \vdots & \vdots & \vdots & \vdots & \vdots & \vdots \\ \phi(\|p_1 - p_1\|) & \cdots & \phi(\|p_1 - p_n\|) & 1 & x_1 & y_1 & z_1 \\ 1 & \cdots & 1 & 0 & 0 & 0 & \\ x_1 & \cdots & x_n & 0 & 0 & 0 & 0 \\ y_1 & \cdots & y_n & 0 & 0 & 0 & 0 \\ z_1 & \cdots & z_n & 0 & 0 & 0 & 0 \end{bmatrix} \begin{bmatrix} \lambda_1 \\ \vdots \\ \lambda_n \\ c_0 \\ c_1 \\ c_2 \\ c_3 \end{bmatrix} = \begin{bmatrix} f(p_1) \\ \vdots \\ f(p_n) \\ 0 \\ 0 \\ 0 \\ 0 \end{bmatrix} \tag{C.5}$$

By solving Equation C.5, the weights λ_i and polynomial coefficients can be calculated. The position of this zero voxel is then substituted into Equation C.1 and the result is assigned as the value of this voxel.

C.3 Results

Our hybrid method was compared with VNN and DW (Figure C.2). Here, one trial with the probe moved in parallel is taken as an example. As shown in Figure C.2, VNN interpolation causes discontinuity artefacts (circled in Figure C.2b), while the DW method blurs the original image, which may result in loss of image details. Also, when the distance threshold is set to a small number, the sparse data that are outside of the constrained region will not be interpolated.

It is a challenge in our in-vivo experiments to quantify the interpolation performance. Instead, our method was evaluated by visual inspection. The local intensity values of the region of interest (ROI) were also assessed (Figure C.3a white box). To achieve this, we compared the results of inter-pixel intensity variations were compared in Figure C.3b.

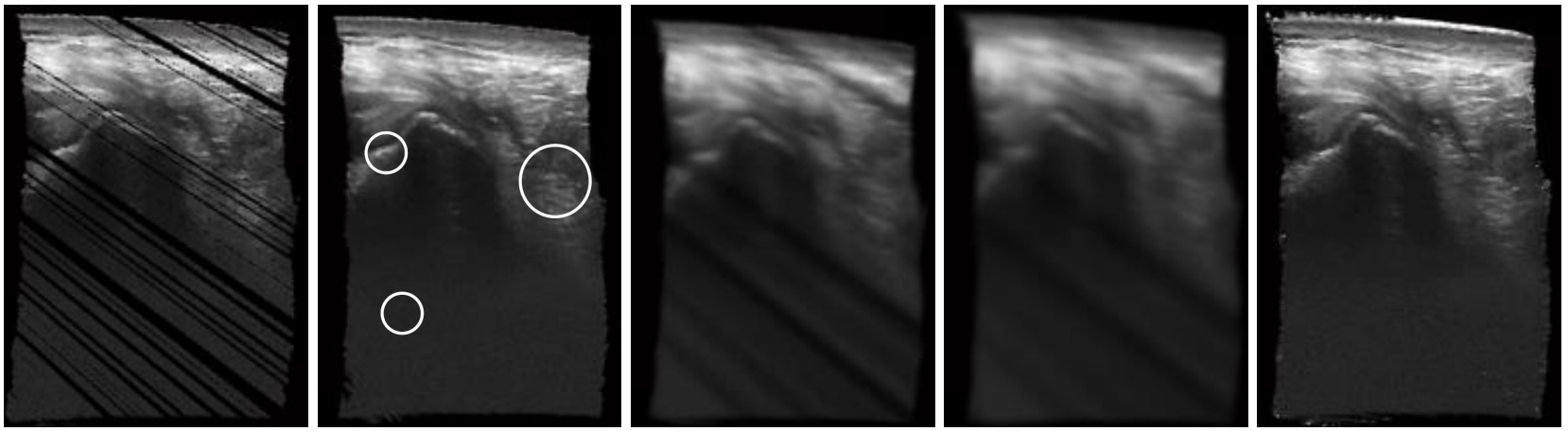

(a) **(b)** **(c)** **(d)** **(e)**

Figure C.2: *One cross section of the reconstructed US volume, a) without interpolation, b) VNN interpolation (discontinuity artefacts circled), c) and d) DW interpolation (with different distance threshold), and e) our method.*

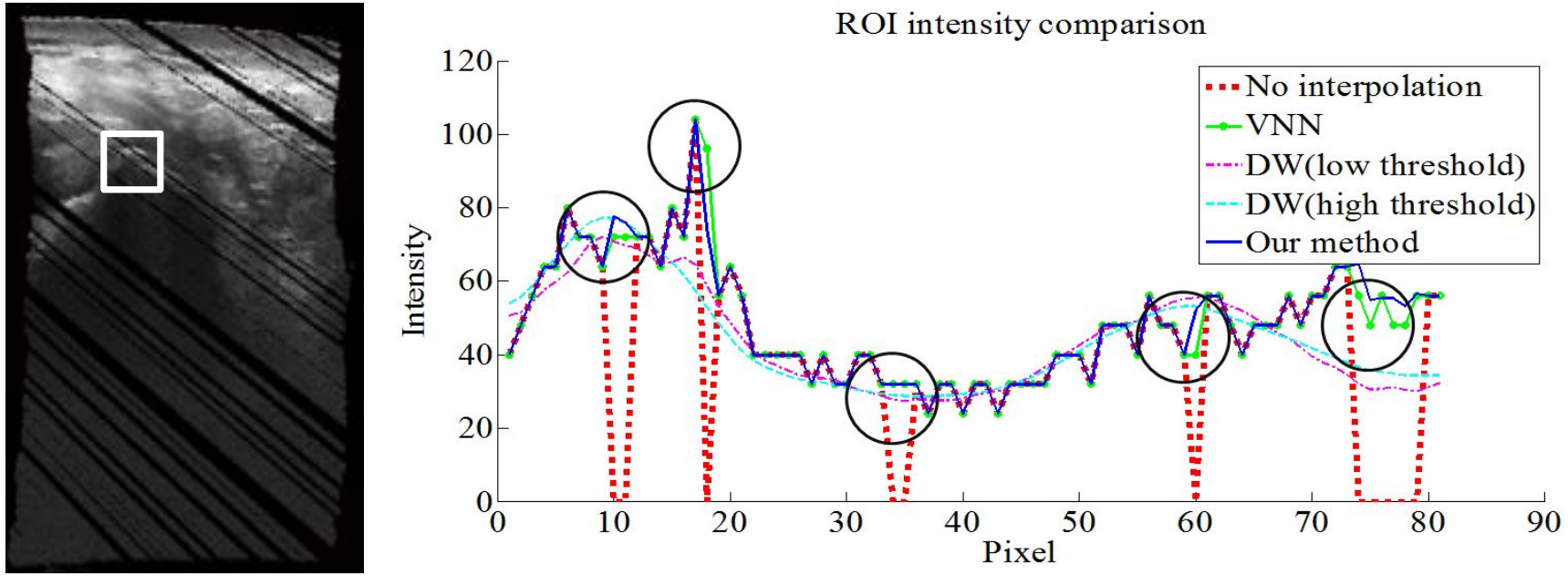

Figure C.3: *Intensity comparison between DW, VNN and our method, a) local region of interest (ROI), and b) comparison of inter-pixel intensity variations.*

As shown in Figure C.3b, the higher the distance threshold set for DW interpolation, the smoother the intensity profile (cyan dashed line), which means the image is more blurred. In the presence of image gaps (circled), VNN interpolation (green dotted solid line) gives more sudden jumps, which are shown as the discontinuities in the resulting image (Figure C.2b). For our method (blue solid line), more detailed intensity information has been presented without large discontinuities.

C.4 Conclusions

In this appendix, a hybrid interpolation method for 3D freehand ultrasound reconstruction using k-d tree searching combined with radial basis function interpolation was presented. By visual inspection, the interpolated 3D volume produced by the new hybrid method appears is more continuous and smoother than traditional VNN and DW methods. However, k-d tree construction and function-based interpolation need more computational time than VNN and DW. Non-optimized this took around 3 hours for a 3D volume with approximate 10 million non-zero voxels. Our method may be sped up by storing more nonzero voxels in one leaf node and searching fewer nearest neighbours. After this 3D US reconstruction, 3D surfaces of the-anatomy-of-interest can be segmented from the reconstructed volumes (Chapter 5). Then, the position of the target bony landmark can be determined by applying 3D surface-to-surface registration approach (Chapter 4).

Bibliography

[1] Akbarshahi, M., Schache, A. G., Fernandez, J. W., Baker, R., Banks, S., and Pandy, M. G. Non-invasive assessment of soft-tissue artifact and its effect on knee joint kinematics during functional activity. *Journal of Biomechanics 43*, 7 (May 2010), 1292–1301.

[2] Aldrich, J. E. Basic physics of ultrasound imaging. *Critical Care Medicine 35*, 5 (2007), S131–S137.

[3] Alton, F., Baldey, L., Caplan, S., and Morrissey, M. C. A kinematic comparison of overground and treadmill walking. *Clinical Biomechanics 13*, 6 (1998), 434–440.

[4] Andriacchi, T. P., Natarajan, R. N., and Hurwitz, D. E. Musculoskeletal dynamics, locomotion, and clinical applications. *Basic Orthopaedic Biomechanics 2* (1997), 37–68.

[5] Andriacchi, T. P., Ogle, J. A., and Galante, J. O. Walking speed as a basis for normal and abnormal gait measurements. *Journal of Biomechanics 10*, 4 (1977), 261–268.

[6] Arnold, A. S., Salinas, S., Asakawa, D. J., and Delp, S. L. Accuracy of muscle moment arms estimated from mri-based musculoskeletal models of the lower extremity. *Computer Aided Surgery 5*, 2 (2000), 108–119.

[7] Arun, K. S., Huang, T. S., and Blostein, S. D. Least-squares fitting of two 3d point sets. *IEEE Transactions on Pattern Analysis and Machine Intelligence*, 5 (1987), 698–700.

[8] Astephen, J. L., Deluzio, K. J., Caldwell, G. E., and Dunbar, M. J. Biomechanical changes at the hip, knee, and ankle joints during gait are associated with knee osteoarthritis severity. *Journal of Orthopaedic Research 26*, 3 (2008), 332–341.

[9] Babak, T., and Alex, M. Vision-based approach for long-term mobility monitoring: Single case study following total hip replacement. *Journal of Rehabilitation Research and Development 51*, 7 (2014), 1165.

[10] Bamberg, S. J., Benbasat, A. Y., Scarborough, D. M., Krebs, D. E., and Paradiso, J. A. Gait analysis using a shoe-integrated wireless sensor system. *IEEE Transactions on Information Technology in Biomedicine 12*, 4 (2008), 413–423.

[11] Barratt, D. C., Penney, G. P., Chan, C. S., Slomczykowski, M., Carter, T. J., Edwards, P. J., and Hawkes, D. J. Self-calibrating 3d-ultrasound-based bone registration for minimally invasive orthopedic surgery. *IEEE Transactions on Medical Imaging 25*, 3 (2006), 312–323.

[12] Besl, P. J., and McKay, N. D. Method for registration of 3d shapes. In *Robotics-DL Tentative* (1992), International Society for Optics and Photonics, pp. 586–606.

[13] Blanco, J. A tutorial on SE(3) transformation parameterizations and on-manifold optimization. Tech. Rep. 3, 2014.

[14] Bland, T., Tong, J., Ward, B., and Parker, N. Geometric distortion of area in medical ultrasound images. *ArXiv e-prints* (2015).

[15] Bridge, C. P., and Noble, J. A. Object localisation in fetal ultrasound images using invariant features. In *2015 IEEE 12th International Symposium on Biomedical Imaging (ISBI)* (2015), IEEE, pp. 156–159.

[16] Brounstein, A., Hacihaliloglu, I., Guy, P., Hodgson, A., and Abugharbieh, R. Towards real-time 3d us to ct bone image registration using phase and curvature feature based gmm matching. In *Medical Image Computing and Computer-Assisted Intervention–MICCAI 2011*. Springer, 2011, pp. 235–242.

[17] Buchanan, A., and Fitzgibbon, A. Interactive feature tracking using k-d trees and dynamic programming. In *IEEE Computer Society Conference on Computer Vision and Pattern Recognition* (2006), vol. 1, IEEE, pp. 626–633.

[18] Buchanan, A., and Fitzgibbon, A. Interactive feature tracking using kd trees and dynamic programming. In *2006 IEEE Computer Society Conference on Computer Vision and Pattern Recognition* (2006), vol. 1, IEEE, pp. 626–633.

[19] Buckland-Wright, C. Which radiographic techniques should we use for research and clinical practice? *Best Practice & Research Clinical Rheumatology 20*, 1 (2006), 39–55.

[20] Buxton, J. D. Fractures and joint injuries. *British Medical Journal 2*, 4941 (1955), 724.

[21] Chen, T. K., Abolmaesumi, P., Pichora, D. R., and Ellis, R. E. A system for ultrasound-guided computer-assisted orthopaedic surgery. *Computer Aided Surgery 10*, 5-6 (2005), 281–292.

[22] Chetverikov, D., Svirko, D., Stepanov, D., and Krsek, P. The trimmed iterative closest point algorithm. In 16th *International Conference on Pattern Recognition* (2002), vol. 3, IEEE, pp. 545–548.

[23] Collins, T. D., Ghoussayni, S. N., Ewins, D. J., and Kent, J. A. A six degrees-of-freedom marker set for gait analysis: repeatability and comparison with a modified helen hayes set. *Gait & Posture 30*, 2 (2009), 173–180.

[24] Comaniciu, D., and Meer, P. Mean shift: a robust approach toward feature space analysis. *IEEE Transactions on Pattern Analysis and Machine Intelligence 24*, 5 (2002), 603–619.

[25] Coupé, P., Hellier, P., Azzabou, N., and Barillot, C. 3d freehand ultrasound reconstruction based on probe trajectory. In *International Conference on Medical Image Computing and Computer-Assisted Intervention* (2005), Springer, pp. 597–604.

[26] David, W. J. Blob detection image matching. 2013.

[27] Davis, R. B., Ounpuu, S., Tyburski, D., and Gage, J. R. A gait analysis data collection and reduction technique. *Human Movement Science 10*, 5 (1991), 575–587.

[28] Dennison, J., and Beverland, D. E. An audit of trochanteric bursitis in total hip arthroplasty and recommendations for treatment. *Journal of Orthopaedic Nursing 6*, 1 (2002), 5–8.

[29] Detmer, P. R., Bashein, G., Hodges, T., Beach, K. W., Filer, E. P., Burns, D. H., and Strandness, D. E. Original contribution magnetic scan head tracking: in vitro calibration and validation. 923–936.

[30] Diamond, L. E., Wrigley, T. V., Bennell, K. L., Hinman, R. S., O'Donnell, J., and Hodges, P. W. Hip joint biomechanics during gait in people with and without symptomatic femoroacetabular impingement. *Gait & Posture 43* (2016), 198–203.

[31] Dicharry, J. Kinematics and kinetics of gait: from lab to clinic. *Clinics in Sports Medicine 29*, 3 (2010), 347–364.

[32] dictionary, M. Gait cycle. In *http://medical-dictionary.thefreedictionary.com/gait+cycle* (2016).

[33] Egmond, N., Stolwijk, N., Heerwaarden, R., Kampen, A., and Keijsers, N. L. Gait analysis before and after corrective osteotomy in patients with knee osteoarthritis and a valgus deformity. *Knee surgery, sports traumatology, arthroscopy* (2016), 1–10.

[34] Eitzen, I., Fernandes, L., Nordsletten, L., and Risberg, M. A. Erratum: sagittal plane gait characteristics in hip osteoarthritis patients with mild to moderate symptoms compared to healthy controls: a cross-sectional study. *BMC Musculoskeletal Disorders 16*, 1 (2015), 1.

[35] Felsberg, M., and Sommer, G. The monogenic signal. *IEEE Transactions on Signal Processing 49*, 12 (2001), 3136–3144.

[36] Fitzgibbon, A. W. Robust registration of 2D and 3D point sets. *Image and Vision Computing 21*, 13-14 (Dec. 2003), 1145–1153.

[37] Foroughi, P., Boctor, E., Swartz, M. J., Taylor, R. H., and Fichtinger, G. P6d-2 ultrasound bone segmentation using dynamic programming. In *Ultrasonics Symposium, IEEE* (2007), IEEE, pp. 2523–2526.

[38] Fulkerson, J. P. Diagnosis and treatment of patients with patellofemoral pain. *The American Journal of Sports Medicine 30*, 3 (2002), 447–456.

[39] Gabel, M., Gilad-Bachrach, R., Renshaw, E., and Schuster, A. Full body gait analysis with kinect. In *2012 Annual International Conference of the IEEE Engineering in Medicine and Biology Society* (2012), IEEE, pp. 1964–1967.

[40] Gage, J. R., Deluca, P. A., and Renshaw, T. S. Gait analysis: principles and applications. *American Journal of Bone Joint Surgery 77*, 10 (1995), 1607–1623.

[41] Geiger, D., Gupta, A., and Costa, L. A. Dynamic programming for detecting, tracking, and matching deformable contours. *IEEE Transactions on Pattern Analysis and Machine Intelligence 17*, 3 (1995), 294–302.

[42] Gilles, B., Christophe, F. K., Magnenat-Thalmann, Nand Becker, C. D., Duc, S. R., Menetrey, J., and Hoffmeyer, P. Mri-based assessment of hip joint translations. *Journal of Biomechanics 42*, 9 (2009), 1201–1205.

[43] Gilles, B., and Pai, D. K. Fast musculoskeletal registration based on shape matching. In *Medical Image Computing and Computer-Assisted Intervention–MICCAI 2008*. Springer, 2008, pp. 822–829.

[44] Gofman, J. *Radiation and human health. [Lead abstract]*. Sierra Club Books,San Francisco, CA, Jan 1981.

[45] Gooding, M. J., Kennedy, S. H., and Noble, J. A. Temporal calibration of freehand three-dimensional ultrasound using image alignment. *Ultrasound in Medicine & Biology 31*, 7 (2005), 919–927.

[46] Griffin, F. M., Math, K., Scuderi, G. R., Insall, J. N., and Poilvache, P. L. Anatomy of the epicondyles of the distal femur: Mri analysis of normal knees. *Journal of Arthroplasty 15*, 3 (2000), 354–359.

[47] Haacke, E. M., Brown, R. W., Thompson, M. R., Venkatesan, R., et al. *Magnetic resonance imaging: physical principles and sequence design*, vol. 82. Wiley-Liss New York:, 1999.

[48] Hacihaliloglu, I., Abugharbieh, R., Hodgson, A. J., Rohling, R. N., and Guy, P. Automatic bone localization and fracture detection from volumetric

ultrasound images using 3d local phase features. *Ultrasound in Medicine & Biology 38*, 1 (2012), 128–144.

[49] Hara, D., Nakashima, Y., Hamai, S., Higaki, H., Ikebe, S., Shimoto, T., Yoshimoto, K., and Iwamoto, Y. Dynamic hip kinematics in patients with hip osteoarthritis during weight-bearing activities. *Clinical Biomechanics 32* (2016), 150–156.

[50] Hara, D., Nakashima, Y., Hamai, S., Higaki, H., Shimoto, T., Ikebe, S., Hirata, M., Kanazawa, M., Kohno, Y., and Iwamoto, Y. In vivo hip kinematics in healthy subjects and patients with osteoarthritis during weight0bearing activities. *Bone Joint Journal 98*, SUPP 2 (2016), 29–29.

[51] Härdle, W. K., and Hlávka, Z. Principal component analysis. In *Multivariate Statistics*. Springer, 2015, pp. 183–203.

[52] Hartley, Rand Zisserman, A. *Multiple view geometry in computer vision*. Cambridge University Press, 2003.

[53] Heberer, K., Fowler, E., Staudt, L., Sienko, S., Buckon, C. E., Bagley, A., Sison-Williamson, M., McDonald, C. M., and Sussman, M. D. Hip kinetics during gait are clinically meaningful outcomes in young boys with duchenne muscular dystrophy. *Gait & Posture 48* (2016), 159–164.

[54] Herrington, L., McEwan, I., and Thom, J. Quantification of patella position by ultrasound scanning and its criterion validity. *Ultrasound in Medicine & Biology 32*, 12 (2006), 1833–1836.

[55] Higuchi, T., Arai, Y., Takamiya, H., Miyamoto, T., Tokunaga, D., and Kubo, T. An analysis of the medial patellofemoral ligament length change pattern using open-mri. *Knee surgery, sports traumatology, arthroscopy 18*, 11 (2010), 1470–1475.

[56] Horowitz, A. L. *MRI physics for radiologists.* Springer, 1995.

[57] Hsu, P. W., Prager, R. W., Gee, A. H., and Treece, G. M. Real-time freehand 3D ultrasound calibration. *Ultrasound in Medicine & Biology 34*, 2 (Feb. 2008), 239–251.

[58] Huang, Q., and Zheng, Y. An adaptive squared-distance-weighted interpolation for volume reconstruction in 3d freehand ultrasound. *Ultrasonics 44* (2006), e73–e77.

[59] Hutin, E., Pradon, D., Barbier, F., Bussel, B., Gracies, J., and Roche, N. Walking velocity and lower limb coordination in hemiparesis. *Gait & Posture 36*, 2 (2012), 205–211.

[60] Ionescu, G. Automated registration of ultrasound with CT images : application to computer assisted prostate radiotherapy and orthopedics. 768–778.

[61] Jia, R. Computer-aided tracking with motion analysis with ultrasound system (CAT-MAUS) for dynamic joint movement tracking. *PRS Transfer Report* (2014).

[62] Jia, R., Mellon, S., Hansjee, S., Monk, A. P., Murray, D., and Noble, J. A. Automatic bone segmentation in ultrasound images using local phase features and dynamic programming. *International Symposium on Biomedical Imaging (ISBI)* (2016), In proceeding.

[63] Jia, R., Mellon, S., Monk, A. P., Murray, D., and Noble, J. A. Three dimensional freehand ultrasound reconstruction using hybrid interpolation. *Medical Image Understanding and Analysis* (2015), 169–174.

[64] Jia, R., Mellon, S., Monk, A. P., Murray, D., and Noble, J. A. A computer-aided tracking and motion analysis with ultrasound (CAT & MAUS) system for the description of hip joint kinematics. *International Journal of Computer Assisted Radiology and Surgery* (2016).

[65] Jia, R., Mellon, S., Monk, A. P., Murray, D., and Noble, J. A. Globally optimal registration for describing joint kinematics. *Procedia of Computer Science, International Conference of Medical Image Understanding and Analysis* (2016).

[66] Jia, R., Monk, A. P., Murray, D. W., Mellon, S. J., and Noble, J. A. Greater trochanter tracking in ultrasound imaging during gait. In *IEEE* 12th *International Symposium on Biomedical Imaging (ISBI)* (2015), IEEE, pp. 260–263.

[67] Jia, R., Shanil, H., Monk, A. P., Murray, D., Noble, J. A., and Mellon, S. Cat & maus: Elucidation of hip joint kinematics in gait and comparison with motion analysis. IET.

[68] Jian, B., and Vemuri, B. C. A robust algorithm for point set registration using mixture of gaussians. In 10th *IEEE International Conference on Computer Vision* (2005), vol. 2, IEEE, pp. 1246–1251.

[69] Kadaba, M. P., Ramakrishnan, H. K., and Wootten, M. E. Measurement of lower extremity kinematics during level walking. *Journal of Orthopaedic Research 8*, 3 (1990), 383–392.

[70] Kitahata, S., Rickers, K., Orias, A. E., Ringgaard, S., Andersson, G., Bunger, C., Peterson, J., Robie, B., and Inoue, N. In vivo kinematic analysis of the spine using 3d mri bone-marrow model. *Bone Joint Journal 98*, SUPP 2 (2016), 109–109.

[71] Kong, H., Akakin, H. C., and Sarma, S. E. A generalized laplacian of gaussian filter for blob detection and its applications. *IEEE Transactions on Cybernetics 43*, 6 (2013), 1719–1733.

[72] Kovesi, P. Symmetry and asymmetry from local phase. In *Tenth Australian Joint Conference on Artificial Intelligence.* (1999), pp. 190–196.

[73] Krebs, D. E., Robbins, C. E., Lavine, L., and Mann, R. W. Hip biomechanics during gait. *Journal of Orthopaedic & Sports Physical Therapy 28*, 1 (1998), 51–59.

[74] Laurin, C. A., Dussault, R., and Levesque, H. P. The tangential x-ray investigation of the patellofemoral joint: x-ray technique, diagnostic criteria and their interpretation. *Clinical Orthopaedics and Related Research 144* (1979), 16–26.

[75] Lawler, E. L., and Wood, D. E. Branch-and-bound methods: A survey. *Operations Research 14*, 4 (1966), 699–719.

[76] Leardini, A., Chiari, L., Della, U., and Cappozzo, A. Human movement analysis using stereophotogrammetry: part 3. soft tissue artifact assessment and compensation. *Gait & Posture 21*, 2 (2005), 212–225.

[77] Leigh, R. J., Osis, S. T., and Ferber, R. Kinematic gait patterns and their relationship to pain in mild-to-moderate hip osteoarthritis. *Clinical Biomechanics 34* (2016), 12–17.

[78] Liu, T., Inoue, Y., and Shibata, K. Development of a wearable sensor system for quantitative gait analysis. *Measurement 42*, 7 (2009), 978–988.

[79] Lucas, B., and Kanade, T. An iterative image registration technique with an application to stereo vision. pp. 674–679.

[80] MacCormick, J. How does the kinect work? *Presentert Ved Dickinson College 6* (2011).

[81] MacWilliams, B. A., Cowley, M., and Nicholson, D. E. Foot kinematics and kinetics during adolescent gait. *Gait & Posture 17*, 3 (2003), 214–224.

[82] Maraci, M. A. Towards engineering ultrasound image analysis solutions for resource constrained environments. *PhD Thesis, University of Oxford* (2016).

[83] Matharu, G. S., Janardhan, S., Brash, L., Pynsent, P. B., Dunlop, D. J., and James, S. L. The utility of repeat ultrasound imaging in the follow-up of metal-on-metal hip arthroplasty patients. *The Annals of The Royal College of Surgeons of England 98*, 2 (2016), 143–149.

[84] Mercier, L., Langø, T., Lindseth, F., and Collins, L. D. A review of calibration techniques for freehand 3d ultrasound systems. *Ultrasound in Medicine & Biology 31*, 2 (2005), 143–165.

[85] Milovanovic, M., Minovic, M., and Starcevic, D. Walking in colors: human gait recognition using kinect and cbir. *IEEE Multi-Media 20*, 4 (2013), 28–36.

[86] Mitchell, H. H., Hamilton, T. S., Steggerda, F. R., Bean, H. W., et al. The chemical composition of the adult human body and its bearing on the biochemistry of growth. *Journal of Biological Chemistry 168* (1945), 625–637.

[87] Monda, M., Goldberg, A., Smitham, P., Thornton, M., and McCarthy, I. Use of inertial measurement units to assess age-related changes in gait kinematics in an active population. *Journal of Aging & Physical Activity 23*, 1 (2015).

[88] Monk, A. P. The patellofemoral joint : form and function. *Thesis University of Oxford* (2011).

[89] Monk, A. P., Chen, M., Mellon, S., Gibbons, M., Beard, D. J., Murray, D. W., and Gill, H. S. Comparison of in-vivo coronal plane patella tracking following knee arthroplasty using the maus technique. *Bone & Joint Journal Orthopaedic Proceedings Supplement 95*, SUPP 26 (2013), 10–10.

[90] Moore, K. L., Dalley, A. F., and Agur, A. M. *Clinically oriented anatomy.* Lippincott Williams & Wilkins, 2013.

[91] Morlock, M., Schneider, E., Bluhm, A., Vollmer, M., Bergmann, G., Müller, V., and Honl, M. Duration and frequency of every day activities in total hip patients. *Journal of Biomechanics 34*, 7 (2001), 873–881.

[92] Mulford, K. Trochanteric bursitis.

[93] Nagpal, S., Abolmaesumi, P., Rasoulian, A., Hacihaliloglu, I., Ungi, T., Osborn, J., Lessoway, V. A., Rudan, J., Jaeger, M., Rohling, R. N., et al. A multi-vertebrae ct to us registration of the lumbar spine in clinical data. *International Journal of Computer Assisted Radiology and Surgery 10*, 9 (2015), 1371–1381.

[94] Nagpal, S., Hacihaliloglu, I., Ungi, T., Rasoulian, A., Osborn, J., Lessoway, V. A., Rohling, R. N., Borschneck, D. P., Abolmaesumi, P., and Mousavi, P. A global CT to US registration of the lumbar spine, 2014.

[95] of Health, D. A joint responsibility : doing it differently musculoskeletal services framework.

[96] Oliveira, F. P., and Tavares, J. Medical image registration: a review. *Computer Methods in Biomechanics and Biomedical Engineering 17*, 2 (2014), 73–93.

[97] Organization, W. H. Bmi classification. In *Global Database on Body Mass Index* (2012).

[98] Palastanga, N., Field, D., and Soames, R. *Anatomy and human movement: structure and function*, vol. 56. Elsevier Health Sciences, 2006.

[99] Pappas, I. P., Popovic, M. R., Keller, T., Dietz, V., and Morari, M. A reliable gait phase detection system. *IEEE Transactions on Neural Systems and Rehabilitation Engineering 9*, 2 (2001), 113–125.

[100] Parker, N., and Neasham, J. Correcting distortions in medical ultrasound images. *SAGE Doctoral Training Notes* (2016).

[101] Peat, G., McCarney, R., and Croft, P. Knee pain and osteoarthritis in older adults: a review of community burden and current use of primary health care. *Annals of Rheumatic Diseases 60*, 2 (2001), 91–97.

[102] Perry, J., and Burnfield, J. M. Gait analysis: normal and pathological function.

[103] Perry, S. *Physical principles of medical imaging.* Radiology, 1985.

[104] Peterson, L. E. K-nearest neighbor. *Scholarpedia 4*, 2 (2009), 1883.

[105] Picerno, P., Cereatti, A., and Cappozzo, A. Joint kinematics estimate using wearable inertial and magnetic sensing modules. *Gait & Posture 28*, 4 (2008), 588–595.

[106] Powers, C. M. The influence of altered lower-extremity kinematics on patellofemoral joint dysfunction: a theoretical perspective. *The Journal of Orthopaedic and Sports Physical Therapy 33*, 11 (2003), 639–646.

[107] Prager, R. W., Gee, A. H., and Berman, L. Stradx: real-time acquisition and visualization of freehand three-dimensional ultrasound. *Medical Image Analysis 3*, 2 (1999), 129–140.

[108] Prager, R. W., Ohling, R. N., Gee, A. H., and Erman, L. B. Rapid calibration for 3D freehand Ultrasound. 855–869.

[109] Preis, J., Kessel, M., Werner, M., and Linnhoff-Popien, C. Gait recognition with kinect. In *1st International Workshop on Kinect in Pervasive Computing* (2012), New Castle, UK, pp. P1–P4.

[110] Qvistgaard, E., Kristoffersen, H., Terslev, L., Danneskiold-Samsøe, B., Torp-Pedersen, S., and Bliddal, H. Guidance by ultrasound of intraarticular injections in the knee and hip joints. *Osteoarthritis and Cartilage 9*, 6 (2001), 512–517.

[111] Rahman, J., Tang, Q., Monda, M., Miles, J., and McCarthy, I. Gait assessment as a functional outcome measure in total knee arthroplasty: a cross-sectional study. *BMC Musculoskeletal Disorders 16*, 1 (2015), 1.

[112] Rajpoot, K., Grau, V., and Noble, J. A. Local-phase based 3d boundary detection using monogenic signal and its application to real-time 3d echocardiography images. In *International Symposium on Biomedical Imaging ISBI* (2009), IEEE, pp. 783–786.

[113] Ramakrishnan, H. K., and Kadaba, M. P. On the estimation of joint kinematics during gait. *Journal of Biomechanics 24*, 10 (1991), 969–977.

[114] Ramasubramanian, V., and Paliwal, K. K. Fast k-dimensional tree algorithms for nearest neighbor search with application to vector quantization encoding. *IEEE Transactions on Signal Processing 40*, 3 (1992), 518–531.

[115] Razek, A., and El-Basyouni, S. Ultrasound of knee osteoarthritis: interobserver agreement and correlation with western ontario and mcmaster universities osteoarthritis. *Clinical Rheumatology 35*, 4 (2016), 997–1001.

[116] René, R. Gaussian rounding. In *http://www.xbeat.net/vbspeed/i_BankersRounding.htm*. 2002.

[117] Rohling, R. N. 3D freehand ultrasound: reconstruction and spatial compounding. *PhD Thesis, the Univeristy of Cambridge* (1998).

[118] Ross, A. Procrustes analysis. *Course Report, Department of Computer Science and Engineering, University of South Carolina* (2004).

[119] Sarra, S. A. Adaptive radial basis function methods for time dependent partial differential equations. *Applied Numerical Mathematics 54*, 1 (2005), 79–94.

[120] Sato, Y., Nakamoto, M., Tamaki, Y., Sasama, T., Sakita, I., Nakajima, Y., Monden, M., and Tamura, S. Image guidance of breast cancer surgery using

3d ultrasound images and augmented reality visualization. *IEEE Transactions on Medical Imaging 17*, 5 (1998), 681–693.

[121] Sawbones. Catalogue biomechanical testmaterials.

[122] Segal, N. A., Felson, D. T., Torner, J. C., Zhu, Y., Curtis, J. R., Niu, J., and Nevitt, M. C. Greater trochanteric pain syndrome: epidemiology and associated factors. *Archives of Physical Medicine and Rehabilitation 88*, 8 (2007), 988–992.

[123] Shbeeb, M. I., and Matteson, E. L. Trochanteric bursitis (greater trochanter pain syndrome). *Mayo Clinic Proceedings. Mayo Clinic 71*, 6 (1996), 565–569.

[124] Solberg, O., Lindseth, F., Torp, H., Blake, R. E., and Hernes, T. A. Freehand 3d ultrasound reconstruction algorithms: a review. *Ultrasound in Medicine & Biology 33*, 7 (2007), 991–1009.

[125] Souza, R. B., Draper, C. E., Fredericson, M., and Powers, C. M. Femur rotation and patellofemoral joint kinematics: a weight-bearing magnetic resonance imaging analysis. *Journal of Orthopaedic & Sports Physical therapy 40*, 5 (2010), 277–285.

[126] Sproull, R. F. Refinements to nearest-neighbor searching in k-dimensional trees. *Algorithmica 6*, 1-6 (1991), 579–589.

[127] Standring, S. *Gray's anatomy: the anatomical basis of clinical practice*. Elsevier Health Sciences, 2015.

[128] State, A., Chen, D. T., Tector, C., Brandt, A., Chen, H., Ohbuchi, R., Bajura, M., and Fuchs, H. Case study: observing a volume rendered fetus within a pregnant patient. 364–368.

[129] Tao, W., Liu, T., Zheng, R., and Feng, H. Gait analysis using wearable sensors. *Sensors 12*, 2 (2012), 2255–2283.

[130] Tipping, M. E., and Bishop, C. M. Probabilistic principal component analysis. *Journal of the Royal Statistical Society: Series B (Statistical Methodology) 61*, 3 (1999), 611–622.

[131] Tomasi, C., and Kanade, T. *Detection and tracking of point features*. School of Computer Science, Carnegie Mellon Univ. Pittsburgh, 1991.

[132] Treece, G. M., Gee, A. H., Prager, R. W., Cash, C. J. C., and Berman, L. H. High-definition freehand 3D ultrasound. *Ultrasound in Medicine & Biology 29*, 4 (2003), 529–546.

[133] Treece, G. M., Prager, R. W., Gee, A. H., and Berman, L. Correction of probe pressure artifacts in freehand 3D ultrasound. *Medical Image Analysis 6*, 3 (2002), 199–214.

[134] Tsai, T., Dimitriou, D., Li, J., Nam, K. W., Li, G., and Kwon, Y. Asymmetric hip kinematics during gait in patients with unilateral total hip arthroplasty: In vivo 3-dimensional motion analysis. *Journal of Biomechanics 48*, 4 (2015), 555–559.

[135] University, K. A. Normal gait. In *www.kau.edu.sa/Files/0052891/Subjects/1-NORMAL 1.PPT* (2016).

[136] Wagstaff, K., Cardie, C., Rogers, S., Schrödl, S., et al. Constrained k-means clustering with background knowledge. In *ICML* (2001), vol. 1, pp. 577–584.

[137] Wein, W., Brunke, S., Khamene, A., Callstrom, M. R., and Navab, N. Automatic ct-ultrasound registration for diagnostic imaging and image-guided intervention. *Medical Image Analysis 12*, 5 (2008), 577–585.

[138] Wein, W., Karamalis, A., Baumgartner, A., and Navab, N. Automatic bone detection and soft tissue aware ultrasound–ct registration for computer-aided

orthopedic surgery. *International Journal of Computer Assisted Radiology and Surgery 10*, 6 (2015), 971–979.

[139] Whittle, M. W. Clinical gait analysis: a review. *Human Movement Science 15*, 3 (1996), 369–387.

[140] Whittle, M. W. *Gait analysis: an introduction*. Butterworth-Heinemann, 2014.

[141] Wu, G., Siegler, S., Allard, P., Kirtley, C., Leardini, A., Rosenbaum, D., Whittle, M., D'Lima, D. D., Cristofolini, L., Witte, H., Schmid, O., and Stokes, I. ISB recommendation on definitions of joint coordinate system of various joints for the reporting of human joint motion–part I: ankle, hip, and spine. International Society of Biomechanics., 2002.

[142] Xiao, G., Brady, J. M., Noble, J. A., Burcher, M., and English, R. Nonrigid registration of 3d free-hand ultrasound images of the breast. *IEEE Transactions on Medical Imaging 21*, 4 (2002), 405–412.

[143] Xiong, Y., Zhao, Y., Yang, H., Sun, Y., and Wang, Y. Comparison between interactive closest point and procrustes analysis for determining the median sagittal plane of three-dimensional facial data. *The Journal of Craniofacial Surgery 27*, 2 (2016), 441.

[144] Yang, J., Li, H., and Jia, Y. Go-icp: solving 3d registration efficiently and globally optimally. In *Proceedings of the IEEE International Conference on Computer Vision* (2013), pp. 1457–1464.

[145] Yang, W., Hsu, W., Wu, R., Lu, T., and Lin, K. Motion analysis of axial rotation and gait stability during turning in people with parkinson's disease. *Gait & Posture 44* (2016), 83–88.

[146] Yao, Z., and Li, H. Tracking a detected face with dynamic programming. *Image and Vision Computing 24*, 6 (2006), 573–580.

[147] Zhang, Y., Rohling, R., and Pai, D. K. *Direct surface extraction from 3D freehand ultrasound images.* IEEE, 2002.